



AGH

AGH UNIVERSITY OF SCIENCE AND TECHNOLOGY

Faculty of Physics and Applied Computer Science

Doctoral thesis

Karolina Drogowska

Effect of hydrogen charging in Ti-V-Ni thin films and their oxides

Supervisor: dr hab. inż. Zbigniew Tarnawski, prof. AGH

Co-Supervisor: Dr. hab. Adam Georg Balogh,

Technische Universität Darmstadt

Cracow, 2013

Declaration of the author of this dissertation:

Aware of legal responsibility for making untrue statements I hereby declare that I have written this dissertation myself and all the contents of the dissertation have been obtained by legal means.

date, author signature

Declaration of the thesis Supervisor:

This dissertation is ready to be reviewed.

date, supervisor signature

Acknowledgements

I would like to thank my supervisor, Prof. Zbigniew Tarnawski, for giving me opportunity to work on such an interesting topic, for trusting in me and his great help. Moreover, I thank him for encouraging me to apply for the MPD Programme, which allowed me to improve my knowledge and develop my skills during my stay in Darmstadt. I would like to thank my co-supervisor, Dr. hab. Adam Georg Balogh, for creating such incredible work conditions and access to such wide variety of experimental techniques. I am grateful to him for his patience, fruitful discussions and explanations, as well as personal support and motivation.

I would like to express my gratitude to my colleagues from different groups, where I had a great pleasure to work and learn: Institute of Materials Science, Technische Universität Darmstadt, the Faculty of Computer Science, Electronics and Telecommunications, AGH Krakow and the Faculty of Mathematics and Physics, Charles University in Prague, Czech Republic. In particular, I thank Dr. Stefan Flege for introducing me the SIMS technique and his great help during the experiments, Dr. Joachim Brötz and Dr. Edward Kusior for XRR measurements and analysis, Dr. Andrzej Brudnik for sample preparation, M.Sc. Halina Czternastek for optical measurements, RNDr. Ladislav Havela for hydrogenation experiments under high pressures and Prof. Radomír Kužel for XRD and XRR measurements for these films.

The collaboration with Dr. Hans-Werner Becker from Dynamitron Tandem Labor, Ruhr-Universität Bochum, Germany in performing the N-15 experiments is highly acknowledged.

I deeply appreciate scientific and personal help, many fruitful discussions, excellent pieces of advice and support of Prof. Katarzyna Zakrzewska from Faculty of Computer Science, Electronics and Telecommunications, AGH Krakow.

I would like to thank Prof. Nhu-Tarnawska Hoa Kim Ngan from Institute of Physics, Pedagogical University in Kraków for her great help and guidance, especially with RBS measurements and data analysis.

I would like to thank my best friends, Maciej Kluczny and Paweł Mercik for their friendship, fantastic common moments and experiences, and belief in me. I owe Barbara Łysoń-Sypień a debt of gratitude for her wisdom and support. I would like to thank people who made the time of my stay in Darmstadt such an unique experience: Przemysław Chrzastowski, Andreas Jurkowski and Marek Walasek for establishing our Polish Team there and fantastic adventures during exploration of south Hessen. I am exceptionally lucky to meet such incredible friends during the time of my Ph.D. studies, especially Xavier Marti,

Wojciech Tabiś, Dominik Przyborowski, Kamil Koźlak, Małgorzata Tokarz and Joanna Kowalska, whom I wanted to thank as well.

I would like to thank Foundation for Polish Science for the financial support provided under MPD "Krakow Interdisciplinary PhD-Project in Nanoscience and Advanced Nanostructures" financed by the EU European Regional Development Fund. I also express my gratefulness to Prof. Bartłomiej Szafran for his great work as the coordinator of the MPD Programme and great help in many occasions.

I acknowledge financial support from the Grant for young scientists from The Faculty of Physics and Applied Computer Science, AGH.

I would like to thank the Faculty of Mathematics and Physics, Charles University in Prague, especially Prof. Vladimír Sechovský, for the financial support for my stay in Prague during performing the high-pressure hydrogenation experiments. I acknowledge also the financial support from the DAAD project D/08/07729 (coordinators: Dr. hab. A.G. Balogh, Prof. N.-T. Hoa Kim Ngan).

But most of all, I would like to thank my marvelous family, especially my amazing parents and my inspiring sister. Your strong support, trust and belief in me, raising my spirit and unlimited love have always motivated me. Thank you for inspiring me by your achievements, for your wisdom, for your understanding and giving me such a feeling of safety.

I do want to express my hearted gratitude to my Vojtěch for all the miracles which he has brought into my life. *“Láska je touha po ztracené půli nás samých!”*

*To the most inspiring persons of my life:
my parents Małgorzata and Edmund,
my sister Ola
and my Vojtěch.*

Content

Streszczenie	v
Zusammenfassung	vii
Motivation, aim and scope	1
1. Hydrogen, titanium, vanadium and nickel	3
1.1 Hydrogen in metals and metal oxides.....	3
1.1.1 Hydrogen absorption and desorption.....	3
1.1.2 Applications of hydrogen and metal hydrides	8
1.2 Titanium and titanium oxides	11
1.2.1 Physical and chemical properties of titanium.....	11
1.2.2 Applications of titanium	12
1.2.3 Physical and chemical properties of titanium oxides	13
1.2.4 Application of titanium oxides	14
1.2.5 Influence of hydrogen on titanium and titanium oxide	18
1.2.6 Application of titanium hydrides.....	20
1.3 Vanadium and vanadium oxides	20
1.3.1 Physical and chemical properties of vanadium	20
1.3.2 Physical and chemical properties of vanadium oxides.....	21
1.3.3 Application of vanadium oxides.....	27
1.4 Ti-TiO _x and V-VO _x thin films	28
1.4.1 Ti-TiO _x thin films	28
1.4.2 V-VO _x thin films	31
1.4.3 TiO ₂ – VO _x thin films.....	35
1.5 Nickel as a dopand.....	37
2. Samples preparation and experimental techniques	39
2.1 Samples preparation	39
2.2 Hydrogenation	41
2.3 High – resolution SEM.....	42
2.3.1 Scanning process and image formation.....	42
2.3.2 SEM resolution.....	43
2.4 X-ray Diffraction	44
2.4.1 Physical background.....	44
2.4.2 XRD measurements.....	45

2.5 X-ray Reflectivity	46
2.5.1 The theoretical background	46
2.5.2 XRR measurements	47
2.6 Rutherford Backscattering	47
2.6.1 History	48
2.6.2 Physical background.....	48
2.6.3 Instrumentation and Experimental Techniques	53
2.6.4 Data evaluation and computer simulations.....	57
2.7 Secondary Ion Mass Spectrometry	60
2.8 Nuclear Reaction Analysis – N-15 method	63
2.8.1 Physical background.....	63
2.8.2 Data evaluation and computer simulations.....	64
2.9 Optical measurements	65
3. Investigations of layer geometry and properties of as-deposited Ti-TiO₂ thin films ...	67
3.1 The thin Ti-TiO ₂ films deposited on Si(111) substrates	68
3.2 The thicker Ti-TiO ₂ films on Si(111) substrates	81
3.3 The Ti-TiO ₂ films deposited on C-foils.....	82
4. Effect of hydrogenation on the Ti-TiO₂ thin films	87
4.1 Hydrogen charging of Ti-TiO ₂ films covered partially by Pd.....	87
4.1.1 Film structure and composition	87
4.1.2 Resistivity of hydrogenated Ti thin films	90
4.1.3 Hydrogen profiling in Ti-TiO ₂ films	92
4.2 Hydrogenation of Ti-TiO ₂ films at high pressure.....	98
4.2.1 Results and discussion.....	98
4.2.2 Influence of hydrogenation to film crystallinity.....	102
5. Hydrogen charging of VO_x- TiO₂ thin films	103
5.1 The as-deposited VO _x -TiO ₂ films	103
5.2 Effect of hydrogen charging on the VO _x - TiO ₂ films.....	107
5.3 Hydrogen profile of TiO ₂ /V ₂ O ₅ /SiO ₂ film	114
6. Hydrogen absorption in Ti-V-Ni films	117
6.1 Chemical composition of the Ti-V-Ni films	117
6.2 Hydrogen profile of Ti-V-Ni films	122
Conclusions and final remarks.....	125
References	127
List of publications	

Streszczenie

Przedmiotem pracy są badania właściwości układów cienkich warstw tytanowych, wanadowych oraz ich tlenków, a także warstw metalicznych zawierających tytan (Ti), wanad (V) i nikiel (Ni), oraz zbadanie wpływu wodorowania na ich wybrane właściwości fizyczne. Celem badań przedstawionych w pracy było uzyskanie dwu i trójwarstwowych układów metaliczno-tlenkowych na różnych podłożach (krzem, szkło, węgiel) metodą rozpylania katodowego, zbadanie ich właściwości fizycznych, nawodorowanie w różnych warunkach oraz określenie zmian zachodzących w warstwach po procesie wodorownia.

Praca zawiera trzy grupy materiałów cienkowarstwowych, które poddane zostały procesowi wodorownia i których właściwości fizyczne zostały zbadane:

1. systemy warstw Ti-TiO₂ na Si(111), SiO₂ i foliach węglowych,
2. systemy warstw VO_x-TiO₂ na SiO₂,
3. warstwy Ti-V-Ni na Si(111) oraz SiO₂.

Pojedyncze warstwy metaliczne Ti, dwuwarstwy Ti-TiO₂ oraz trójwarstwy Ti-TiO₂-Ti zostały scharakteryzowane za pomocą metod X-ray Reflectivity (XRR), X-ray Diffraction (XRD), Rutherford Back-Scattering (RBS) i pomiarów optycznych. Oporność elektryczna została zmierzona za pomocą metody czteropunktowej. Powierzchnia próbek została przebadana za pomocą Auger Electron Spectroscopy (AES) oraz High Resolution Scanning Electron Microscopy (HRSEM).

Badania strukturalne wykazały gładkie i jednorodne warstwy, brak dyfuzji atomów wchodzących w skład poszczególnych warstw. Wyznaczone za pomocą trzech komplementarnych metod grubości warstw nie wykazują większych odstępstw od założonych wartości. Obraz SEM dla przekroju systemu warstw Ti/TiO₂/Ti wskazuje na kolumnowy wzrost warstwy dwutlenku tytanu.

Warstwy zostały wodorowane wielokrotnie w różnych warunkach, tj. w temperaturze pokojowej pod wysokim ciśnieniem, jak i w podwyższonej temperaturze (300 °C) i ciśnieniu wodoru 1 bar. Wpływ wodorownia na warstwy został opisany po porównaniu badań przeprowadzonych przed i po wodorowaniu. Metody Secondary Ion Mass Spectrometry (SIMS) i Nuclear Reaction Analysis (NRA - N-15) pozwoliły uzyskać profile wodoru w próbkach, jak również jego ilość w poszczególnych warstwach. Zauważono, że przykrycie próbki warstwą palladu zwiększa zarówno ilość magazynowanego wodoru, jak i efektywność jego dyfuzji w głąb multiwarstwy. Otrzymane profile wskazują na brak zmian w koncentracji wodoru w warstwie TiO₂, co jest związane z jej kolumnową budową. Metodą RBS wykazano

wzrost grubości warstw, natomiast pomiary rentgenowskie wskazują na zanik preferowanej orientacji tytanu po wodorowaniu w wysokich ciśnieniach ($p_{H_2} = 102$ bar).

Badania RBS pozwoliły na uzyskanie informacji o stechiometrii tlenków wanadu w systemach warstw VO_x - TiO_2/SiO_2 . Powtórzenie tych badań po wodorowaniu wykazało redukcję stopnia utlenienia tlenku po każdym procesie wodorownia. Przykrycie warstwy V_2O_5 warstwą TiO_2 nie zmniejszyło absorpcji i dyfuzji wodoru, i w konsekwencji redukcji tlenku wanadu. Dodatkowo, grubości warstw zwiększyły się, co wskazuje na gromadzenie się wodoru w warstwach.

Wpływ domieszkowania niklem na zdolność absorpcji wodoru przez warstwy tytanowo-wanadowej został zbadany metodami RBS i N-15. Badania te wykazały utlenianie się powierzchni podczas procesu wodorownia, głównie do TiO_2 . Podobnie jak we wcześniej badanych warstwach, wodór dyfundował przez tę warstwę i gromadził się w głębszych podwarstwach metalicznych, co zostało zaobserwowane na profilach wodoru. Profile te wskazują na dobrą absorpcję wodoru przez warstwę Ti-V-Ni oraz jego gromadzenie się w warstwie (ok. 40 at.%). Podobne ilości wodoru były uzyskane dla czystych warstw tytanowych.

Zusammenfassung

Metall-Wasserstoff-Systeme, besonders die Dünnschichtsysteme, sind seit einigen Jahrzehnten sowohl Gegenstand der Grundlagenforschung als auch von hohem technologischen Interesse. Der auf Zwischengitterplätzen atomar gelöste Wasserstoff verändert die physikalischen Eigenschaften der Metalle, wie z. B. elektrischer Widerstand, Kristallstruktur oder optische Eigenschaften. Metalle sind auch Materialien, die Wasserstoff speichern können. Um die für Anwendungen optimale Materialeigenschaften zu erhalten ist es notwendig systematische Untersuchungen an solchen Proben durchzuführen.

Andere Beispiele für die aktuelle technologische Bedeutung dieser Systeme sind die Metall-Wasserstoff-Akkumulatoren oder die Brennstoffzellen für die Nutzung von Wasserstoff als sekundären Energieträger, sowie die Materialversprödung von metallischen Werkstoffen durch Wasserstoff.

Diese Arbeit fasst drei Gruppen von Dünnschichtsystemen zusammen, welche durch verschiedene Wasserstoffprozesse behandelt und deren physikalischen Eigenschaften untersucht wurden:

1. Ti-TiO₂-Schichten auf Si(111)- und SiO₂-Substrat, sowie auf Kohlenstofffolien;
2. VO_x-TiO₂-Schichten auf SiO₂;
3. Ti-V-Ni-Schichten auf Si(111)- und SiO₂

Einzelne Metallschichten von Titan, Ti-TiO₂ Doppelschichten und Ti-TiO₂-Ti Mehrschichtproben wurden mit Hilfe der Röntgenreflektometrie (XRR), der Röntgenbeugung (XRD), der Rutherford Backscattering Spectrometry (RBS) und unter Anwendung von optischen Messungen charakterisiert. Der elektrische Widerstand wurde mit Hilfe der Vier-Punkt-Methode gemessen. Die Oberfläche der Proben wurde mit Augerelektronenspektroskopie (AES) und hochauflösender Rasterelektronenmikroskopie (HRSEM) untersucht.

Die Schichten wurden mehrmals temperatur- und druckabhängig mit Wasserstoff beladen. Der Einfluss der Wasserstoffbeladung auf die Schichten wurde durch den Vergleich der durchgeführten Versuche vor und nach der Wasserstoffbehandlung untersucht. Wasserstoff-Tiefenprofile und Wasserstoffkonzentration in den Proben wurden mit Sekundärionen-Massenspektrometrie (SIMS) und Kernreaktionsanalyse (N-15) ermittelt. Es ist wichtig zu erwähnen, dass durch die Beschichtung der Proben mit Palladium sowohl die Konzentration des eingelagerten Wasserstoffes als auch die Effektivität der Diffusion in die Tiefe der Proben erhöht wurde. Mit der RBS Methode wurde die Zunahme der Schichtdicke nachgewiesen, jedoch haben die Röntgenmessungen darauf hingewiesen, dass die bevorzugte Diffusionsrichtung des Titans zunehmend verloren geht, nachdem die Probe unter hohem Druck ($p_{\text{H}_2} = 102 \text{ bar}$) mit Wasserstoff beladen wurde.

Die Auswertung der RBS Spektren erlaubten es uns Erkenntnisse über die genaue Zusammensetzung der Vanadiumoxide zu gewinnen. Die Wiederholung dieser Untersuchungen hat gezeigt, dass der Oxidationsgrad nach jedem Wasserstoffprozess abnimmt. Die Beschichtung des V_2O_5 durch TiO_2 hat die Absorption des Wasserstoffs nicht verringert und folglich auch nicht die Reduktion des Vanadiumoxids.

Der Einfluss der Anreicherung der Titan-Vanadiumschicht durch Nickel wurde ebenfalls mit der RBS Methode untersucht. Wasserstoff-Tiefenprofile, die mit der N-15 Methode gewonnen wurden, deuten auf eine gute Absorption des Wasserstoffes in der Ti-V-Ni-Schicht und einer Anreicherung von Wasserstoff in der Schicht hin (etwa 40 at.%). Ähnliche Wasserstoffmengen wurden nur bei reinen Titanschichten erzielt.

Motivation, aim and scope

Hydrogen has been generally accepted as a fuel in the future. Both expiration of fossil fuels and the greenhouse effect threatening the development of human civilization make us consider other, efficient and renewable, energy sources, lacking the negative impact on environment. There is currently a lot of hope in hydrogen-based energy. The construction of hydrogen-based energy systems brings up the issue of interaction of hydrogen and matter. One of special topics is then searching for optimum hydrogen storage materials, which would improve the space efficiency (better than in pressurized or liquid hydrogen) and provide the safety of operation. Metal hydrides for hydrogen storage applications are a key enabling technology for the extensive use of hydrogen as an energy carrier. Nickel–metal hydride (Ni-MH) rechargeable batteries can have two to three times the capacity of equivalent size nickel–cadmium (NiCd) batteries. LaNi_5 hydrides (LaNi_5H_6) are used as a hydrogen storage material reaching already now higher volume densities than liquid hydrogen, which has to be maintained at low temperature $T = 20$ K.

Introduction hydrogen into the crystal lattice in general leads to an expansion and modification of both crystal and electronic structure. Although it brings a relatively small perturbation to the system (e.g. the lattice expansion and the hydrogen bonding with other atoms in the lattice), the new-formed hydrides often exhibiting new and very interesting physical properties. Thin films and multilayers often play an important role in improving the rate of hydrogen absorption. The atom mixing, diffusion across the interfaces and precipitation of nanoparticles may also affect the hydrogen uptake-release cycling.

This work presents results of investigations of the hydrogenation effect on the structure and physical properties of Ti-V-Ni thin films and their oxides. Series of Ti-TiO₂, TiO₂-VO_x and Ti-V-Ni thin films with different layer-structures, different compositions and geometries and layer-thickness have been prepared by sputtering technique on different (Si(111), SiO₂, C) substrates. The films have been characterized by standard techniques, such as X-ray diffraction and reflectometry (XRD and XRR), electron microscopy (SEM), optical spectroscopy. The layer composition and thickness have been determined by Rutherford backscattering spectroscopy (RBS). The hydrogen profiles in the films upon hydrogen charging at 1 bar have been obtained by secondary ion mass spectroscopy (SIMS) as well as by nuclear reaction analysis (NRA) using the nitrogen-15 beam (N-15 method). The influence of hydrogenation under high pressure up to 100 bar on crystal lattice changes have been also investigated.

The thesis consists of 6 chapters. The general information about hydrogen in metals and oxides and application of hydrogen and metal hydrides is given in Chapter 1. The overview of structure and properties of titanium, vanadium and their oxides, their applications and the role of nickel as a dopant are also described in this chapter. Chapter 2 includes

descriptions of the sample preparation by sputter technique, hydrogenation process and the experimental techniques used in this work, such as XRD, XRR, SEM, RBS, SIMS and NRA N-15. The experimental results and data analysis for different thin films are presented in the next chapters. In Chapter 3 we concentrate on investigations of the structure and properties of single-, bi- and trilayered thin films of the Ti-TiO₂ system deposited on Si(111), SiO₂ and C substrates. Effect of hydrogen charging at 1 bar and hydrogenation at 100 bar on selected Ti-TiO₂ thin films systems is described in Chapter 4. We emphasize the role of palladium acting as catalysis for hydrogen absorption in the trilayer Ti-TiO₂-Ti films. In Chapter 5, effect of hydrogen charging on the layer composition and structure of VO_x-TiO₂ thin films is presented. We focus on analysing the oxygen reduction of vanadium oxide especially under influence of hydrogen. Investigations of Ti-V-Ni films deposited on Si(111) and SiO₂ are presented in Chapter 6. In particular, the hydrogen absorption capacity in these films is underlined. Conclusions and final remarks are included at the end of the thesis.

Chapter 1

Hydrogen, Titanium, Vanadium and Nickel

In this chapter, the basic physical and chemical properties of hydrogen, hydrides as well as general properties of Vanadium, Titanium and their oxides are described. The special emphasis is put on their physical properties and their changes under hydrogen absorption, such as an increase of the crystal lattice, changes in mechanical and electrical properties. The general information of thin films and multilayers of Ti-, V-based and their oxide-based system as well as the role of Nickel as a dopand are also included.

1.1 Hydrogen in metal and metal oxides

Hydrogen, the lightest, and the most abundant element in the universe, has many fascinating properties and thus can be applied in many fields. It has three naturally occurring isotopes: protium (denoted as ^1H or H), deuterium (^2H , D), and extremely rare on the earth tritium (^3H , T). Hydrogen exists in several different states. Throughout the universe, it is found to be a monoatomic gas (at low densities in interstellar medium), a metallic conductor (under extremely high pressures and low temperatures) and an ionized plasma (at very high temperatures). On the earth it exists, depending on temperature and pressure, in molecular form - diatomic particle H_2 , as a gas, liquid or solid. Hydrogen is able to react chemically with most of the other elements to form both inorganic (water, acids, hydroxides) and organic (hydrocarbons and their derivatives) compounds. Hydrogen can be also found in many different solids, and as an impurity it has an influence on the properties of materials, both desirable and undesirable, and therefore intensive studies of its behaviour in materials are of utmost importance.

1.1.1 Hydrogen absorption and desorption

Some types of metallic systems can absorb a large amount of hydrogen and release it again upon heating. Such systems are called metallic hydrides (or metal hydrides). Introduction of hydrogen into the crystal lattice leads to an expansion and modification of both crystal and electronic structure. Although it brings a relatively small perturbation to the system (e.g. the lattice expansion and the hydrogen bonding with other atoms in the lattice), the new-formed hydrides often exhibiting new and fascinating physical properties. Very often studying the properties of hydrides can provide additional information on the nature and specific features of interatomic interactions in the initial compounds. Many interesting data concerning metal-hydrogen interaction and mobility of hydrogen in solids are summarized in refs. [1,2]. In the following section, the main and most important mechanisms of hydrogen

mobility are described. Despite of the fact, that the intermolecular bond between the hydrogen atoms building hydrogen molecule is strong (length of 0.74 Å with dissociation energy of 4.75 eV), hydrogen atoms readily dissolve on most transitions metal and oxides surfaces. In case of gas phase charging, several reaction stages of hydrogen with the metal, in order to form the hydride, need to be considered, because molecular hydrogen does not directly diffuse into metallic solids. The stages of hydrogen-metal interaction are shown in Fig. 1.1.

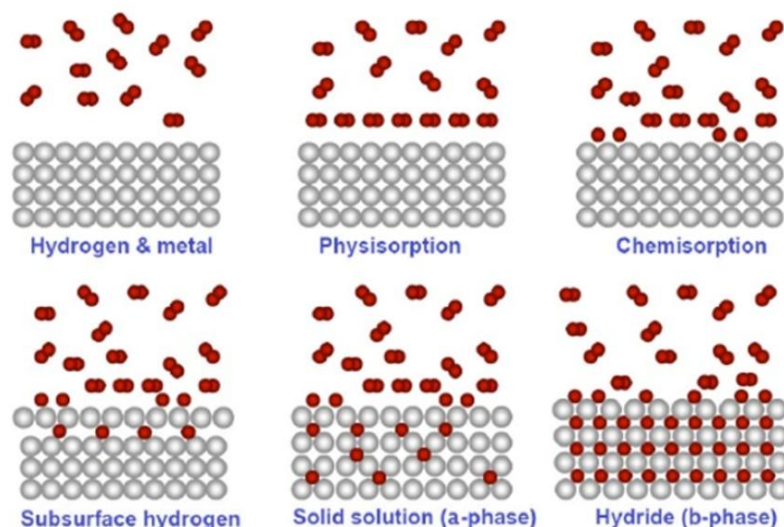


Figure 1.1. Stages of hydrogen-metal interaction. (1) Hydrogen molecules near metal surface, (2) physisorption, (3) chemisorption, (4) creation of hydrogen subsurfaces. Figure taken from [3].

Fig. 1.2 presents the hydrogen diffusion inside a metal and creation of α - and β -phases. The first attractive interaction of the hydrogen molecule approaching the metal surface (1) is the Van der Waals force, leading to a physisorption state (2). Physisorption is a reversible process, strongly dependent on both pressure and temperature. In the next step, dissociation and chemisorption of hydrogen molecule takes place (3). After overcoming activation barrier for the formation of the hydrogen metal bond, hydrogen atoms start diffusing into a bulk (4), occupying the sites randomly inside whole metal lattice. This is very fast process, especially for *bcc* metals with small lattice parameters [4], i.e. the diffusion coefficient for hydrogen in vanadium is of the order $10^4 \text{ cm}^2/\text{s}$ [5]. Until the concentration of hydrogen atoms inside metal is low, hydrogen stays in a host metal as a solid solution (5), the so-called α -phase. Further hydrogen charging increases the amount of hydrogen inside a metal. Some part of hydrogen atoms diffuses through α -phase into deeper parts of metal, but some of them stay with earlier placed atoms, and order in some regular way, because of local interaction between H atoms. It is called the $\alpha+\beta$ phase. Fulfilling all sites leads to the ordered hydride state – the β -phase. Further hydrogen charging leads to movement of the β phase front deep into the bulk.

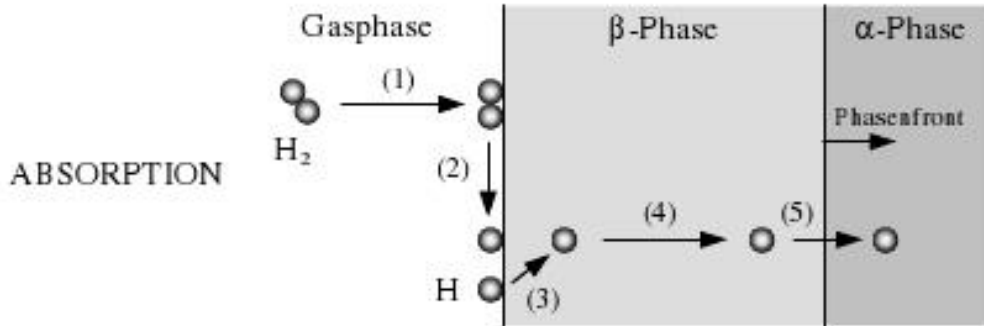


Figure 1.2. Steps of the hydrogenation process accompanied with the movement of phase-front . (1) hydrogen molecule approaching, (2) dissolving, (3) diffusion, (4) bounding inside the lattice, (5) further diffusion and formation of α -phase. Figure taken from [6].

Many metals and alloys react reversibly with hydrogen to form metal hydrides according to the reaction (1.1):



where Me is a metal, a solid solution, or an intermetallic compound, MeH_x is the respective hydride and x the ratio of hydrogen to metal, $x=cH [H/Me]$, Q is the heat of reaction. The reaction is reversible. Usually, during the charging processes (hydride forming, absorption) the heat is released, while the desorption requires the supplied heat.

Amount of hydrogen, which can be absorbed, depends on the heat of reaction. In certain materials, like the metals of group III-V transition elements and alkali metals, this is an exothermic reaction which means that absorption of hydrogen takes place also at low temperatures. All the other metals, with exception of Pd, Ni and Mn, belong to endothermic system, so the heat has to be supplied for hydride formation.

Depending on external conditions, such as temperature and pressure, different phases can exist in binary hydrogen/metal systems. As it was reported by Fukai [2], in room temperature and under normal pressure, during the process of hydride forming, an ionized hydrogen atom occupies interstitial sites – tetrahedral or octahedral – in the metal host lattice, as presented in Fig. 1.3. The electron is given to the conducting electron gas cloud, which shields the proton. The dissolution of hydrogen atoms leads to an expansion of the host metal lattice, increasing atomic volume of 2 to 3 \AA^3 per hydrogen atom, as it was reported by

Schober and Wenzl, for the behaviour of hydrogen inside niobium [7]. Dependence on atomic volume of niobium in the function of hydrogen concentration is presented in Fig. 1.4.

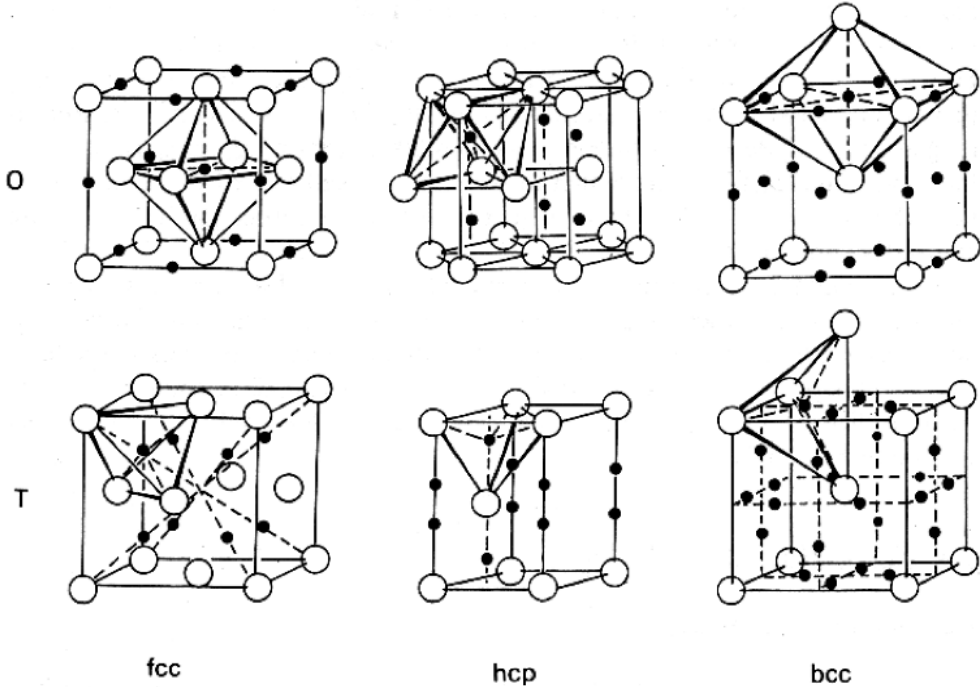


Figure 1.3. Octahedral (top, O) and tetrahedral (bottom, T) interstitial sites occupied by hydrogen atoms for different metal crystal lattices. Picture taken from [2].

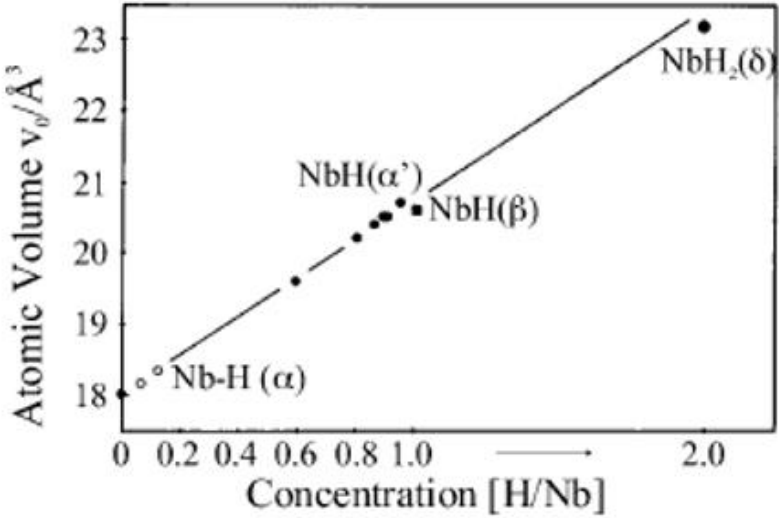


Figure 1.4. Volume expansion of the Nb host metal with increasing H concentration [7].

The mechanisms of hydrogen absorption are in principle similar both for surfaces, as well as for bulks. The difference can be caused by intrinsic properties of host, like phonon spectrum, electronic charge density, quantum mechanical tunneling due to small hydrogen mass and the process of surface to subsurface hydrogen migration.

Desorption of hydrogen is the process as shown in Fig. 1.5. During this process, due to decrease of hydrogen amount within the bulk, the phase transition takes place (I). The hydrogen atoms from a material diffuse into the direction of surface (II). There, on the surface, the atomic hydrogen is released into atmosphere (III) and after the recombination with another hydrogen atom (IV), the hydrogen molecule appears in the gas phase (V).

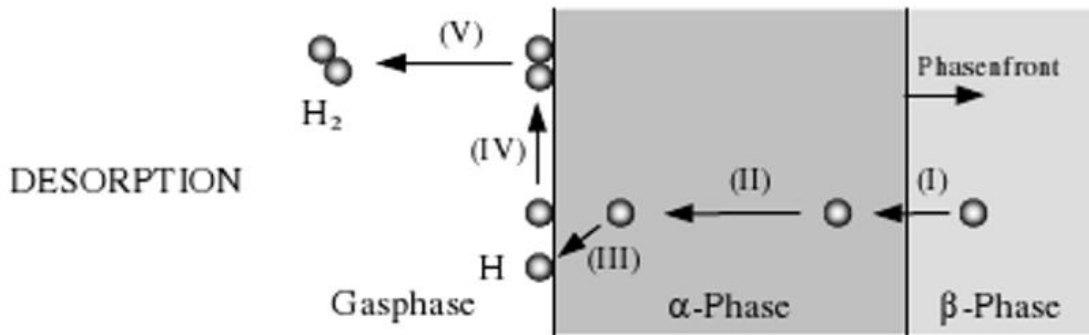


Figure 1.5. Stages of hydrogen desorption process. Decreasing hydrogen concentration leads to disappearance of β -phase (I), movement of H atoms towards surface (II), achieving surface (III) and recombination with other H atoms (IV) to create an H_2 molecule (V). Figure taken from [6].

In the bulk oxides hydrogen can exist as a neutral hydrogen atom (H^0), as a charged ion (H^+ or H^-) or as a molecule (H_2). As a molecule, hydrogen exists within grain boundaries of the oxide [8] which results in formation of cracks and voids. The case of neutral atoms is very special one, since H atoms can fill the interstitial sites of the lattice, with no interaction with other elements of the sample, especially with oxygen anions was observed e.g. in silica (SiO_2) [9] or inside a platinum dispersed $BaMnO_3$ perovskite. These H atoms can diffuse freely through the structure without changing the electrical properties of the oxides. On the other hand, H atom can be ionized and then the H^+ ions can react with oxygen anions and form very stable OH^- groups residing on O^{2-} ion position [10]. The hydrogen transport is very effective due to hopping mechanism and H^+ ion jump between adjacent oxygen. Hydrogen H^+ ions formed in oxides are the most interesting case because of possible application of hydrogen charged oxides in electrical and electrochemical devices [8]. Due to low concentration of oxygen vacancies in native oxides as well as the fact, that the mobility of hydrogen in oxides is much lower compared to metals (the highest reported diffusion coefficients are only of the order 10^{-8} cm^2/s and rapidly decrease with decreasing

temperature), these materials are often doped with other effectively-negative charge impurities to improve the H^+ ion transport. H^- ion formation was reported for first time in 1984, when Malaman and Brice [11] identified oxyhydride (hydride and oxygen ion together in the same structure) for calcite type phase of LaHO. The other examples of such oxides are usually the perovskite related structure – i.e. $LaSrCoO_3H_{0.7}$ or $Ba_3(AlO_4)H$.

1.1.2 Applications of hydrogen and metal hydrides

Hydrogen is generally considered to be the fuel of future. Both expiration of fossil fuels and the greenhouse effect threatening the development of human civilization make us consider other efficient and renewable energy sources especially with lacking the negative impact on environment. There is currently a lot of hope in hydrogen-based energy, which is reflected by massive research programs both in USA and Europe. The construction of hydrogen-based energy systems brings up the important issue for fundamental research, e.g. obtaining the knowledge of the interaction of hydrogen and matter in the solid-state form. One of special topics is then searching for optimum hydrogen storage materials, which would improve the space efficiency (better than in pressurized or liquid hydrogen) and provide the safety of operation. Although advent of mobile applications (cars) expected on a broad scale will still take some years, smaller scale stationary or special mobile applications (boats) are currently operational and gradually gaining a market.

Metal hydrides for hydrogen storage applications are a key enabling technology for the extensive use of hydrogen as an energy carrier. $LaNi_5$ hydrides ($LaNi_5H_6$) are used as hydrogen storage materials reaching higher volume densities than liquid hydrogen. Besides, unlike the liquid hydrogen, which has to be maintained at low temperature $T = 20$ K, such metal hydrides are stable and thus can be maintained at room temperature.

The first idea for using hydrogen as a fuel was proposed by Jules Verne in “The mysterious island”, and was included in the words of Cyrus Smith: “I believe that water will be employed as fuel, that hydrogen and oxygen, used singly or together, will furnish an inexhaustible source of heat and light, of an intensity of which coal is not capable”. Since 1839, when Sir William Grove [12] demonstrated the device converting chemical energy directly into electrical one, fuel cells have started to be considered as devices with wide range of potential applications. The example of the scheme of fuel cell is shown in Fig. 1.6. A fuel cell contains three segments: the anode, the electrolyte and the cathode. The chemical reactions occur at the interfaces:

- At the anode, hydrogen splits to electrons and protons. The so called Proton Exchange Membrane (PEM) separates the free electrons, which move through an external circuit producing electrical current, and lets the protons travel through the electrolyte to the cathode.

- Protons reunite with the electrons at the cathode, and react with oxygen, creating water. A very important aspect of hydrogen fuel cells is that only environmentally friendly combustion products are emitted.

Currently, fuel cells are applied in more and more devices. Due to their high efficiency, silent operation and lack of polluting gases they can be found in hybrid cars, boats and planes.



Figure 1.6. Scheme of proton-conducting hydrogen fuel cell and principle of its operation. Picture taken from [13].

The role of palladium in improving hydrogen dissociation reaction in the metal surface has been widely investigated [14]. Also other metals were applied as additives because of high costs of palladium. Interesting results have been obtained for nickel, cobalt, iron, niobium, titanium and vanadium [15], and the best catalytic effect has been observed especially for Ti and V implantations. Leon et al. [16] compared hydrogen kinetics in magnesium thin films doped with palladium and vanadium ions and showed, that hydrogen absorption was faster in case of vanadium-implanted films than in pure magnesium- and palladium-implanted films. Schulz et al. [17] reported that V and Ti were better catalysts than Ni for hydrogen absorption and desorption in transition metal-doped MgH_2 . Pozzo and Alfe [18] investigated a wide range of transition metal dopants including Ti, Zr, V, Fe, Ru, Co, Rh, Ni, Pd, Cu and Ag. Their results showed that Ti, V and Zr, together with Ru, could eliminate the Mg–H dissociation barrier. Such oxides as CeO_2 , Nb_2O_5 , Fe_2O_3 and V_2O_5 [19,20] are the best candidates for improvement of hydrogen desorption parameters. Additionally, it has been

reported that only rutile form of titanium dioxide additive changes the absorption-desorption hydrogen processes in MgH_2 .

Currently, strong emphasis is put on replacing toxic materials, included in electrodes of batteries. One example is to use a hydrogen-absorbing alloy instead of cadmium, such as LaNi_5 , MgNi_5 hydride, in e.g. Nickel Metal-Hydride (NiMH) batteries. Besides, these batteries have 30-50% higher capacity, higher energy density (140–300 $\text{W}\cdot\text{h/L}$) and the absence of a memory effect [21]. These batteries can be also found in small electronic devices (due to lack of necessity for special safety equipment preventing overcharging of the battery), as well in hybrid electric vehicles.

As already mentioned, the reaction of hydrogen absorption is exothermic, and the heat supplied to the metal hydride releases hydrogen, thus the metal hydrides could be used as heat pumps. Heat pumps are kind of refrigerators, which can be designed for cooling or heating functions, depending on the heat migration associated with hydrogen absorption/desorption. When heat is supplied from an external source (e.g. air, water, exhaust gas) to lower-temperature metal hydride, it releases hydrogen which is absorbed by higher-temperature hydride and the heat will be produced in a heating processes [22].

Investigation on metals altering their reflectivity dramatically after hydrogenation exposition have been studied intensively since 1996 after the discovery, that the rare earth metals (yttrium and lanthanides) can switch their optical behaviour when they are charged with hydrogen [23], e.g. the transparence of Y film increases significantly upon hydrogen charging process as shown in Fig.1.7. These materials were the first step for application such systems as switchable mirrors.

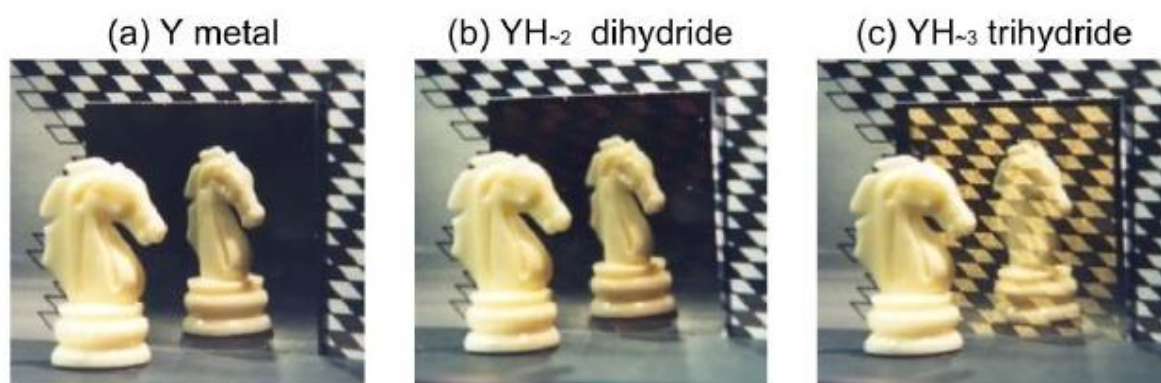


Figure 1.7. The hydrogen induced optical transition of YH_x films: (a) The reflecting metallic Y film prior to hydrogenation, (b) the dihydride state, transparence increases (c) the transparent trihydride state. Pictures from [23].

Richardson et al. [24] found that the process of switching the optical properties takes place also in Mg-transition metal alloys (where Co, Fe, Mn and V are the additives). Niessen and Notten [25] used Mg, Ti, V and Cr for preparing thin films absorbing significant amount of hydrogen, that can be applied as hydrogen sensors or smart solar collectors.

Metal hydrides have been one of the main research topics of the Department of Solid State Physics, Faculty of Physics and Applied Computer science, AGH Krakow. The general information about the work done by the AGH group and be found in refs. [26,27]. However, the investigations have been performed on the bulk samples. In this work we concentrate on the hydrogen effect on especially thin film systems, such as titanium, vanadium-based thin films.

1.2 Titanium and titanium oxides

1.2.1 Physical and chemical properties of titanium

Titanium (Ti) has an element with atomic number 22, mass of 47.867 g/mol and density of 4.506 g/cm³. The name "Titanium" was derived from the Titans of Greek mythology, which symbolizes the strength. Titanium has 5 stable isotopes with atomic number ranging from 46 to 50. ⁴⁸Ti is the most abundant, making almost 74% of natural titanium abundance. The oxidation states of titanium are +1, +2, +3 and +4.

Titanium has a high corrosion resistance, good mechanical properties (Mohs' hardness of 6.0 and Young's modulus of 116 GPa). Both melting (1669 °C) and boiling (3287 °C) points are relatively high. Titanium is paramagnetic and has a low electrical ($2.38 \cdot 10^6$ S/m at temperature of 293 K) and thermal conductivity ($21.9 \text{ W} \cdot \text{m}^{-1} \cdot \text{K}^{-1}$). At room temperatures, pure titanium has a hexagonal close-packed (*hcp*) crystal structure (α phase), with the lattice parameters $a = 0.295$ nm and $c = 0.468$ nm, and thus the c/a ratio of 1.587 is smaller than the value of 1.633 for the ideal *hcp* crystal structure [28]. The unit cell of this phase is shown in Fig. 1.8 (a), where additionally the three most densely packed types of planes have been indicated: the basal (0002) plane, one of three prismatic $\{10\bar{1}0\}$ planes and one of six pyramidal $\{10\bar{1}1\}$ planes. An allotropic phase transformation, changing the crystal structure to a body-centered cubic (*bcc*) crystal structure (β phase) takes place at temperature of 882 °C, but is strongly depended on the purity of the metal. Fig 1.8 (b) illustrates the titanium crystal lattice at 900 °C with lattice parameter $a = 0.332$ nm.

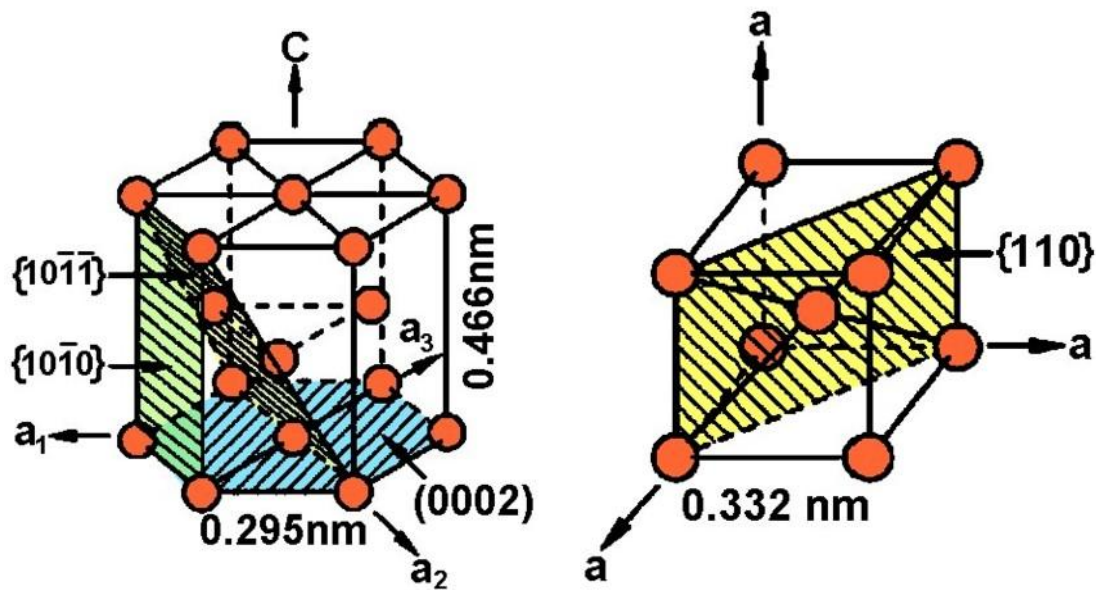


Figure 1.8. Unit cells of Ti crystal lattice: (left) α phase (*hcp* structure) of titanium at room temperature, (right) β phase (*bcc* structure) for titanium at temperatures at 900 °C. Taken from [28].

1.2.2 Applications of titanium

Titanium itself as well as its alloys play an important role in many industrial applications thanks to their excellent corrosion resistance and high specific strength. Besides, titanium is also known as a biocompatible element used successfully in body implants due to its small atomic mass, good mechanical properties and harmless native oxide formed easily upon oxidation. The applications of titanium is listed below:

- Aerospace: exhaust ducts, hydraulic systems, aircraft engines and frames, naval ships,
- Modern army: light weapons, ocean-deployed devices,
- Automotive: automobile or motorcycle racing,
- Medicine: biocompatible element used in body implants, surgery instruments,
- Industry: petrochemical and chemical, pulp and paper, metallurgy, steel production,
- Architecture: parts for building or bridges constructions,
- Sport: bicycle frames, tennis rackets, hockey and cricket sticks,
- Jewelry: rings, body piercing, watches and clocks components,
- Nuclear waste storage.

The most serious disadvantage of titanium is its high price, what restrains its application.

1.2.3 Physical and chemical properties of titanium dioxide

Titanium oxides can be generally classified as Magnéli phases Ti_nO_{2n-1} (for $n = 4-10$). Their phase diagram is shown in Fig. 1.9.

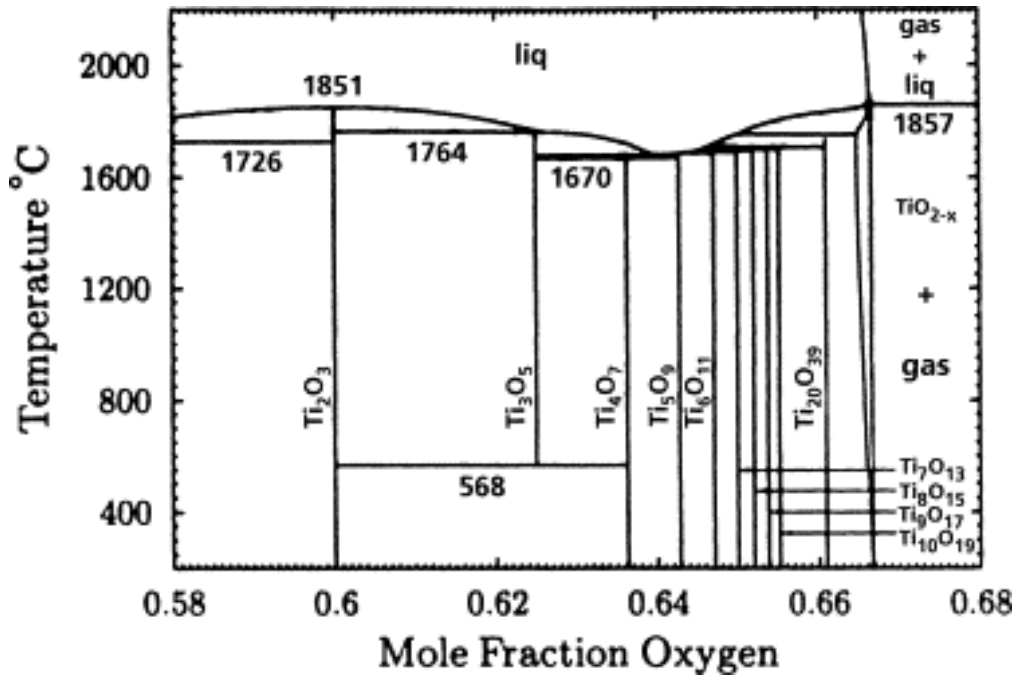


Figure 1.9. Phase diagram of titanium oxides, according to Waldner and Eriksson [29].

The highest relative ratio of oxygen to titanium can be found in titanium dioxide TiO_2 , which is formed as result of the reaction with oxygen at 1200 °C in air, and at 610 °C in pure oxygen. TiO_2 is also the most abundant and most resistant form of titanium oxides. TiO_2 occurs as white powder with molar mass 79.86 g/mol, density of 4.23 g/cm³, melting point of 1857 °C and boiling point of 2972 °C, not soluble in water. It has amphoteric properties, reacts with concentrated sulfur acid and when melted with hydroxides, carbonates or oxides of other metals, it forms the titanates.

Three polymorphic forms of TiO_2 are known to exist: tetragonal rutile (stable at high temperatures), orthorhombic brookite and tetragonal anatase (which can be converted to rutile upon heating [30]). The structure of different TiO_2 phases are shown in Fig. 1.10.

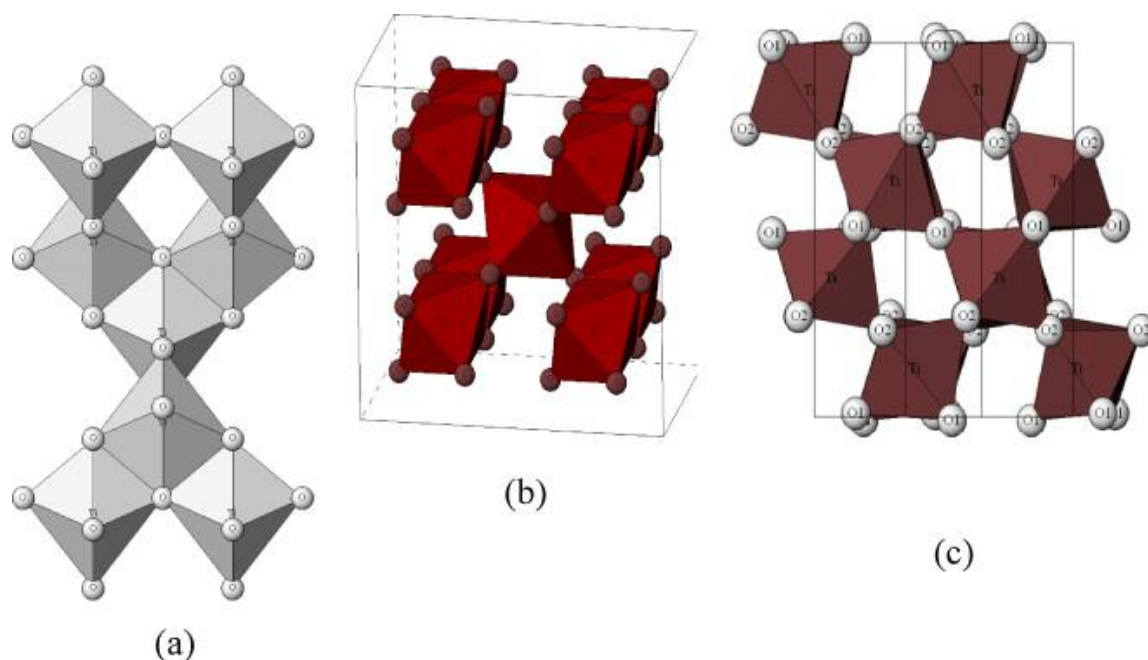


Figure 1.10. The different forms of TiO_2 : (a) anatase, (b) rutile and (c) brookite. Figure taken from [31].

Rutile is the most stable TiO_2 form. It derives its name from Latin, where *rutilus* means red, due to the colour of this mineral. Rutile has a primitive tetragonal unit cell, with unit cell parameters $a = b = 0.459$ nm and $c = 0.295$ nm. Anatase, named from Greek *anathasis* (“extension”) occurs in a form of small crystals. Pure anatase is transparent and brittle, and crystallizes in the tetragonal system, with unit cell parameters $a = b = 0.378$ nm and $c = 0.951$ nm. Brookite is the rarest form, named for James Henry Brook, an English mineralogist and crystallographer. It belongs to the orthorhombic dipyramidal crystal class. The unit cell parameters are $a = 0.546$ nm, $b = 0.918$ nm and $c = 0.514$ nm [28].

The stoichiometric titanium dioxide is a n-type semiconductor. For all different TiO_2 forms, the valence band stays in the same energy level, but there are some differences for the conduction band. Thus, the band gap is respectively 3.23 eV, 3.02 eV and 2.96 eV for anatase, brookite and rutile.

1.2.4 Application of titanium oxides

TiO_2 is one among potential candidates for photocatalysts due to its most efficient photoactivity, highest stability and lowest cost. There are two types of photochemical reaction proceeding on a TiO_2 surface when irradiated with ultraviolet (UV) light: the first one includes the photo-induced redox reactions of adsorbed substances and the other type is the photo-induced hydrophilic conversion of TiO_2 itself. Recently, a large interest has arisen for

this material in newer fields such as homogeneous or heterogeneous catalysis. In fact, the beginning of a new era in heterogeneous photocatalysis was marked by the discovery of the photocatalytic splitting of water on TiO_2 electrodes by Fujishima and Honda in 1972 [32]. TiO_2 nowadays finds various novel applications in photoelectrochemistry, photocatalysis, solar cells and gas sensors [33-35]. Besides, there is currently a large interest to hydrogen-based energy. Thus a strong effort has been focused on the use of photocatalysis for light-assisted production of hydrogen. It leads to the intensive research e.g. in the field of solar-hydrogen (i.e. photoelectrochemical splitting of water to produce gaseous hydrogen using solar energy). The pioneer work of solar-hydrogen based on TiO_2 was published during 1970s [32,36]. However, even though the reaction efficiency is very high, TiO_2 can absorb only the UV light contained in a solar spectrum, which is only about 3%. The energy conversion efficiency (ECE) in the photoelectrochemical cell (PEC) was at the level of $\sim 0.5\%$. Thus the enthusiasm in the research of the H_2 production was over in the middle of the 1980s and the research shifted to the utilization of the strong photo-produced oxidation power of TiO_2 for the destruction of pollutants. Recently, the wide-band gap semiconductor TiO_{2-x} (i.e. with a small departure ($x \neq 0$) from the stoichiometric composition) as well as the TiO_2 -based materials are again considered as the most promising candidates for photoelectrodes for solar-hydrogen where the search is focused in modifying properties to increase the ECE to the required level for commercialization [37,38]. Moreover, increased interest in TiO_2 is concerned to the development of its nanostructure forms, nanotubes, nanorods, etc. for renewable energy sources and hydrogen economy (e.g. hydrogen production, detection and even storage) [39-41]. For an extensive overview of the development of TiO_2 -based photocatalysis and its future prospects from both scientific and technological viewpoints, see refs. [42-44]. Schematic principle of a photo-electrochemical cell using TiO_2 electrode for photocatalytic water splitting [45] is presented in Fig. 1.11.

In particular, Fujishima et al. [43] highlighted the astonishing number of publications involving heterogeneous photochemical studies (in general) and those specifically involving TiO_2 : among about 2400 heterogeneous photochemistry papers published in 2008, roughly 80% involved TiO_2 -based materials, as shown in Fig. 1.12. During the last ten years the number of papers published per year related to the use of TiO_2 for solar cells has increased steadily and reached more than 1000 in 2010 [45], as shown in Fig. 1.13.

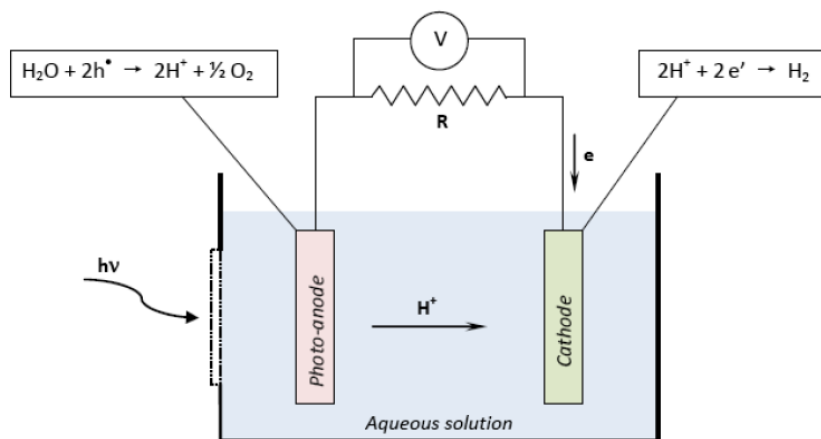


Figure 1.11. Schematic principle of a photo-electrochemical cell (PEC) for photocatalytic water splitting (taken from Figure 1 in the paper of M.-I. Baraton [45], adapted from Figure 1 of J. Nowotny et al. [38]).

Due to its very high refractive index and strong ability to UV light absorption, TiO_2 is used as component for [46-48]:

- white pigment (standard of whiteness called titanium white, Pigment White 6, or CI 77891): in medicine (pills, tablets), cosmetics (toothpaste), coatings (optical coatings for laser mirrors, interference filters), paints, food (milk) or paper,
- transparent plastic,
- agrotechnical foils,
- food packaging (reduces the vitamins decomposition),
- cosmetics (sunscreens, skin protection creams).

Due to its photocatalytic properties, TiO_2 is applicable for [49-52]:

- in self-cleaning surfaces (windows, foils, fabric, car mirrors),
- in the purification processes: of fumes (NO_x reduction), of water and sewage (pesticide decomposition),
- organic synthesis catalyst,
- cement production,
- nanocrystal solar cells (cheaper than silica cells),
- gas sensors,
- photocatalysis for light-assisted production of hydrogen.

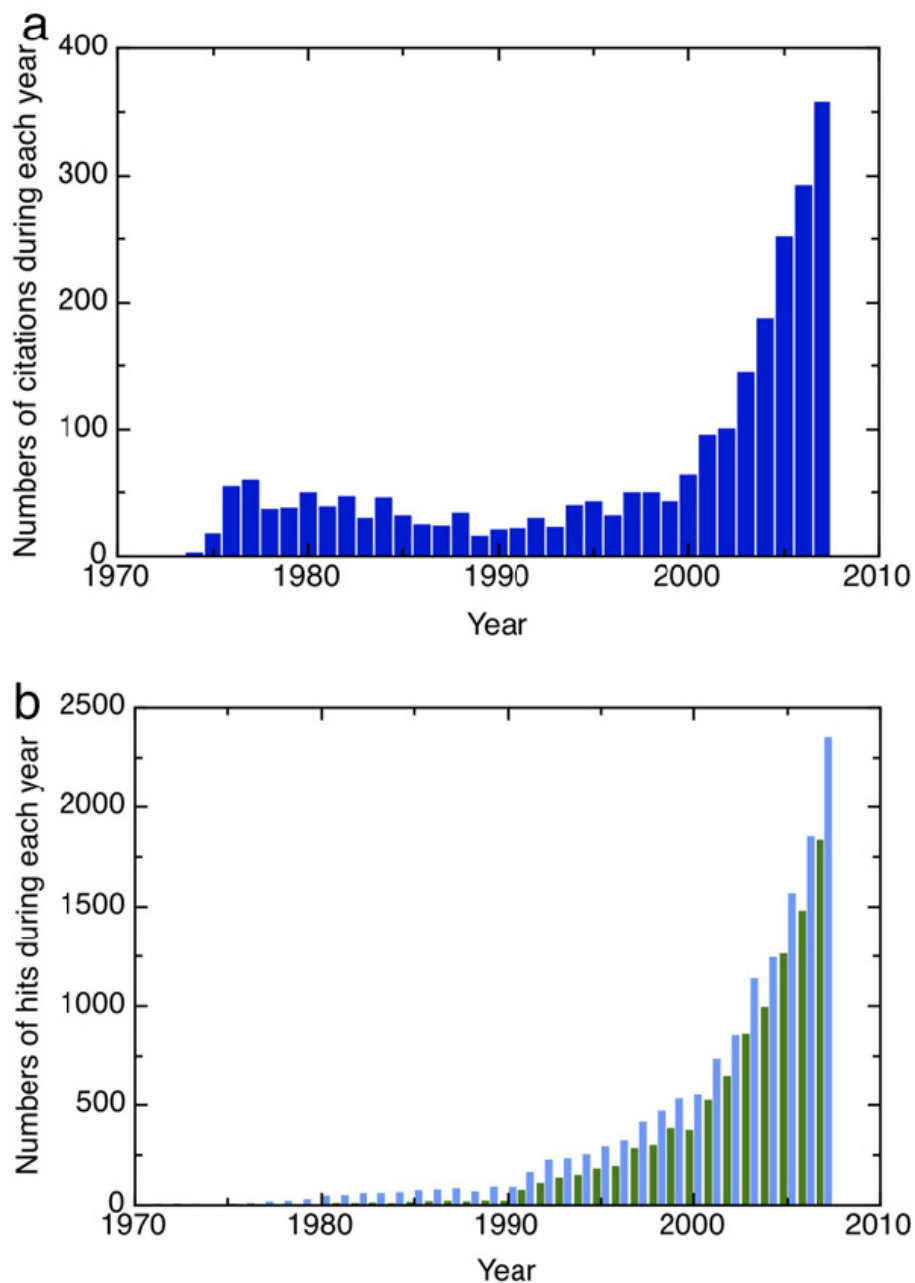


Figure 1.12. The Fig. 2.4 in the paper of Fujishima et al. [43]: a) Citations per year of the Nature paper [65] reported the discovery of Fujishima and Honda in 1972 of the photocatalytic splitting of water on TiO₂ electrodes, b) Numbers of research articles appearing on photocatalysis per year: search results in the period of 1972–2007 with the “Web of Science” (a) by the keyword “ photocataly*” (blue bars) and (b) the keywords “ TiO₂ AND photocataly*” (green bars).

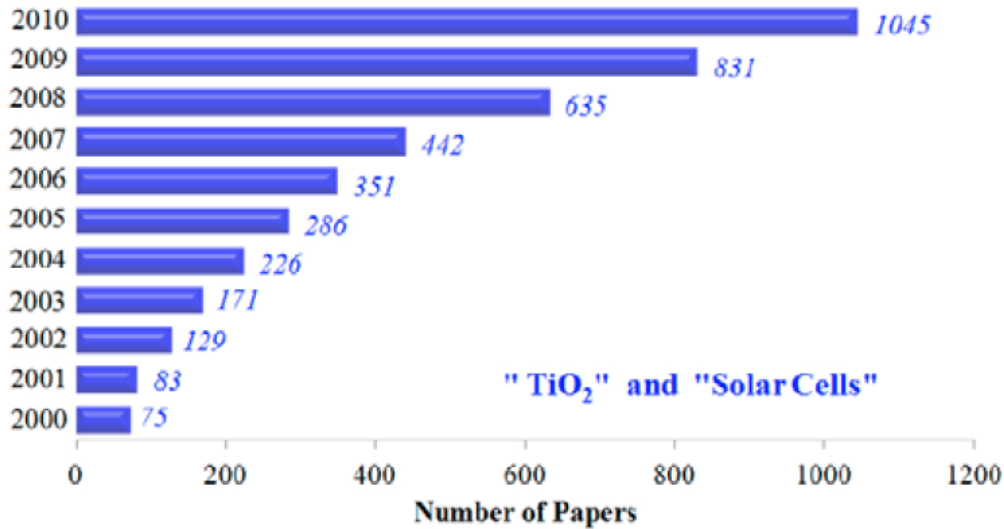


Figure 1.13. The Figure 3 in the paper of M.-I. Baraton [45]: Number of papers published per year (from a literature search in the Current Content database with the keywords “TiO₂” and “Solar cells”).

The increasing interest is recently focusing on the Ti-TiO₂ system in particular in their application in hydrogen economy. For example, TiO₂ nanotubes grown on Ti substrates by anodization could be successfully used for hydrogen storage [40]. Titanium hydride (TiH) films can be used as neutron mirror, H storage layer and standard for H quantitative analysis. Saturation of these systems with hydrogen improves their reflectivity [53]. Metal-insulator-metal (MIM) structures such as Ti/TiO₂/Ti were proposed for resistance random access memories (ReRAM) [54] because their resistance could be switched reversibly by an applied electric field. Understanding the structural and thermodynamical properties of Ti-TiO₂ system as well as their hydrogen absorption ability is critical for the successful implementation of these materials. Although it is known that diffusion of hydrogen in TiO₂ is slower than that in the pure metal, the mechanism by which the oxide influences hydrogen permeation into Ti and its alloys is still not well established [55,56].

1.2.5 Influence of hydrogen on titanium and titanium oxide

Titanium and its alloys have a high affinity for hydrogen; they can pick up a large amount of hydrogen up to more than 50 at.% H [57-59] at elevated temperature above 600 °C (without the formation of a hydride phase). Thus they are considered as promising materials for hydrogen storage applications which are a key enabling technology for the extensive use of hydrogen as an energy carrier (i.e. for hydrogen economy). Besides, the hardness of Ti hydride was found to be about 30% higher than that of pure Ti [58].

As it was described in earlier, hydrogen, when interacting with most transition metals, tends to occupy tetrahedral sites. This situation takes place also in the case of titanium. The titanium-hydrogen phase diagram, presenting the coexistence of the multiple Ti-H phases at equilibrium, is presented in Fig. 1.14.

At lower temperatures (i.e. room temperature), hydrogen in titanium forms the α phase. Its terminal solubility there is quite negligible (~ 0.04 at.%) [60,61]. At elevated temperatures, the hydrogen concentration increases. At eutectoid temperature of 298°C the concentrations of hydrogen in the α phase reaches 4.7 at.%, then the $\alpha+\delta$ phase occurs up to 42.5 at.%. Higher H-concentrations at this temperature are present in the $\beta+\delta$ phase, which transforms to the δ phase when 58.3 at.% of hydrogen is obtained. Increasing of temperatures leads to higher hydrogen concentration, and at 882°C the α to β transformation takes place. This significant increase of hydrogen concentrations is related to the changes of crystal structure. The hexagonal closed packed (*hcp*) lattice of α -Ti exhibits only 4 tetrahedral and 2 octahedral interstitial sites, when the body center cubic (*bcc*) structure of β -Ti consists of 12 tetrahedral and 6 octahedral interstices. Hydrogen atoms in titanium represent a model system for concentrated lattice gas [62]. Therefore, it can be described using the lattice gas automata (LGA) or lattice gas cellular automata (LGCA) methods.

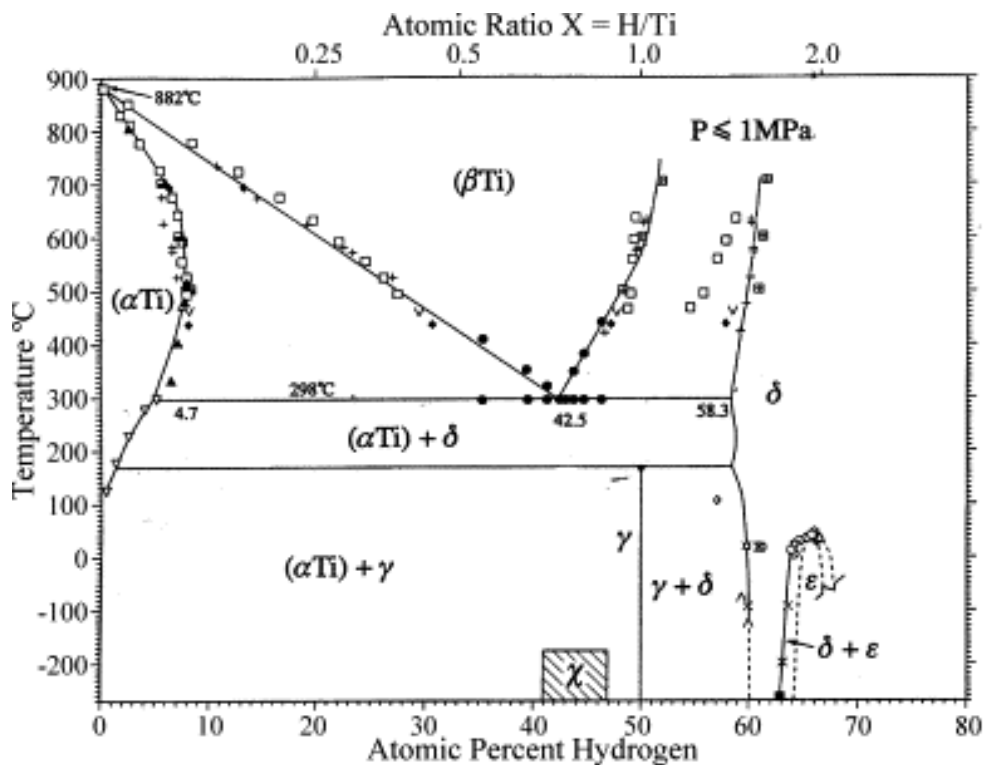


Figure 1.14. Phase diagram Ti-H. Figure taken from [63].

1.2.6 Applications of titanium hydrides

Multilayers of nickel and titanium are recently used for neutron supermirrors. Hydrogen charging of these systems allows to diminish the number of layers needed for the transport of cold neutron beams, because of improve of layers reflectivity. Titanium hydride is used as a hydrogen source for foaming metals. Due to high affinity for hydrogen, titanium hydrides are investigated for hydrogen storage, in hydrogen economy and as a candidate for engine fuels. Additionally, titanium deuteride films are applied as a neutron source in ion beam technology [64].

In industry, titanium hydride is widely used as a bonding material (glass-metal, ceramic-metal, etc.), coating for ceramics, de-oxidizers and de-carbonizer in metallurgy. TiH_2 is applied for sintering of parts used in aerospace, marine, automobiles, machinery, cutting, medical and surgery tools, sport equipment and jewelry.

1.3 Vanadium and its oxides

In this part, properties of vanadium and its oxides will be described. In particular, the astonishing features of vanadium pent-oxide and vanadium dioxide will be presented, together with their applications.

1.3.1 Physical and chemical properties of vanadium

Vanadium (V) has an atomic number 23 and mass of 50.94 g/mol. Nils Gabriel Sefström, who proved the new element by generating chlorides of vanadium, named it after the Scandinavian goddess of beauty and fertility, Vanadis (Freyja).

Vanadium has one stable (^{51}V), and one radioactive (^{50}V) isotope. Additionally, 24 artificial radioisotopes (with mass numbers between 40 and 60) have been characterized, with the most stable being ^{49}V with a half-life of 330 days. The oxidation states of vanadium are: -1, +1, +2, +3, +4 and +5.

Vanadium is a transition metal with a silver-grey colour. It is characterized with good corrosion resistance (including sulfuric and hydrochloric acids, salt solutions, i.e. sea water) and is not soluble in water. Vanadium is a light metal (with density of 6.11 g/cm^3) and shows good mechanical properties (Mohs' hardness of 7.0 and Young's modulus of 127 GPa). Both melting ($1910 \text{ }^\circ\text{C}$) and boiling ($3407 \text{ }^\circ\text{C}$) points are relatively high. Vanadium is paramagnetic and has low both electrical ($4.89 \cdot 10^6 \text{ S/m}$ at temperature of $20 \text{ }^\circ\text{C}$) and thermal conductivity ($30.7 \text{ W} \cdot \text{m}^{-1} \cdot \text{K}^{-1}$). Vanadium crystallises in body-centered-cubic structure, with the unit cell parameter $a = 0.303 \text{ nm}$.

1.3.2 Physical and chemical properties of vanadium oxides

Vanadium reacts with oxygen forming many different forms of vanadium oxides, such as V_2O_5 , VO_2 , V_2O_3 , VO and other distinct phases [65]:

- with the general formula V_nO_{2n+1} , existing between V_2O_5 and VO_2 . Examples of these phases include V_3O_7 , V_4O_9 and V_6O_{13} ,
- with the general formula V_nO_{2n-1} (Magnéli phases), existing between VO_2 and V_2O_3 , with V_4O_7 , V_5O_9 , V_6O_{11} , V_7O_{13} and V_8O_{15} as examples.

Many vanadium-oxygen phases are non-stoichiometric. The occurrence of vanadium-oxide phases is shown in Fig. 1.15.

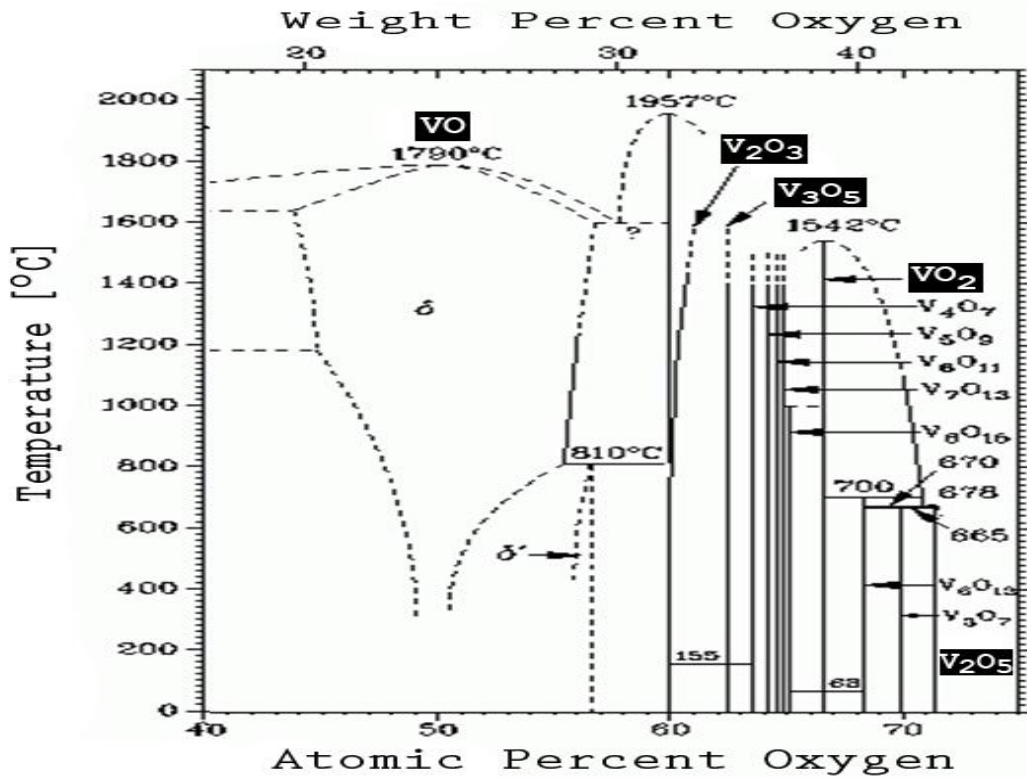


Figure 1.15. Phase diagram of V-O reported by H.A. Wriedt [66].

	Crystal structure	Molar mass	Colour	Solubility in water	T _t (°C)	T _m
VO	--	66.94	grey	insoluble	-147	--
V ₂ O ₃	monoclinic	149.88	black	insoluble	-105	197
VO ₂ (M ₁)	monoclinic	82.94	dark blue	insoluble	67	1967
V ₂ O ₅	orthorhombic	181.88	yellow	0.8 g/L (20 °C)	375	685

Table 1.1. Vanadium oxides at +2, +3, +4 and +5 state of oxidation and their basic properties.

Vanadium oxides have different properties, such as crystal structure, colour, transition temperatures, melting and boiling points. Some of them are soluble in water, some in acids, and some are completely insoluble. The most important properties of them are listed in Table 1.1. From the industrial point of view, among many vanadium oxides, vanadium pent-oxide and vanadium dioxide are most important ones.

Vanadium pent-oxide, V₂O₅ also known as vanadic acid, is the most stable of vanadium oxides. It exists as poisonous yellow-brown powder, with molar mass of 181.880 g/mol and density of 3.357 g/cm³. V₂O₅ undergoes a semiconductor-metal phase transition at 257 °C [65]. Vanadium pentoxide also possesses electrochromic properties, displaying colour changes from blue to green and to yellow in relatively short time. Below the transition temperature, V₂O₅ is characterized by the band gap energy of ~2.24 eV, as an indirect transition from the split-off oxygen 2*p* band up to the vanadium 3*d* band. The V₂O₅ structure was determined by Bachmann in 1961 [67]. It is orthorhombic, with lattice parameters *a* = 1.151 nm, *b* = 0.356 nm, *c* = 0.437 nm. Analogically the other electrochromic metal oxides, it is composed of VO₅ square pyramids (~0.44 nm apart). The pyramids form alternating double chains along the *b*-axis, what is presented in Fig. 1.16. The chains form a plane in the *a*-*b* plane due to lateral connection by bridging oxygen atom, O_b (marked in red). The planes themselves are connected by van der Waals bonds. The places of vanadium and oxygen atoms in VO₅ pyramide, with distances between vanadium and oxygen atoms are presented in Fig. 1.17. Vanadium atom (white circle) is singly coordinated by the vanadyl oxygen atom (O_v), which lies directly above or below in the *c*-direction. Three chain oxygen atoms (O_{ch}) create the chain along the *b*-axis, whereas bridge oxygen atoms (O_b) connect the chains in the *a*-direction.

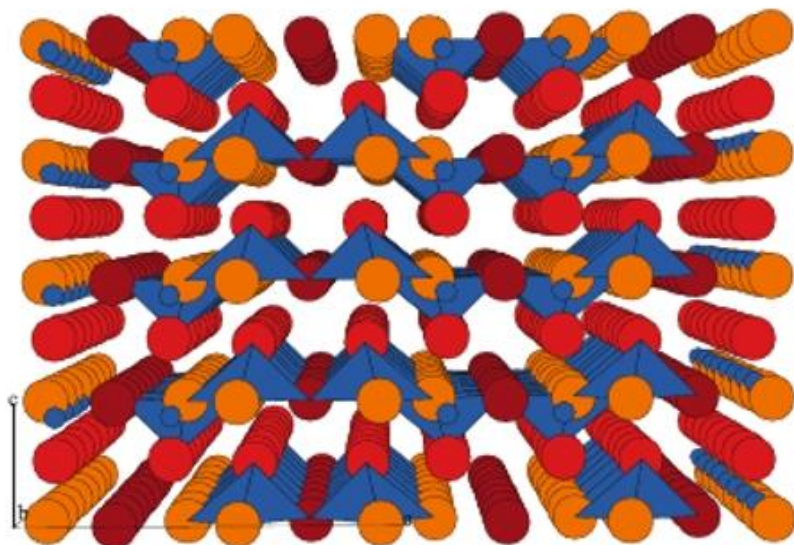


Figure 1.16. Crystal structure of vanadium pent-oxide V_2O_5 . Small blue circles represent vanadium atoms, red, orange and brown circles represent vanadyl-, chain- and bridge oxygen atoms, respectively. Each van der Waals layer in the a - b plane is comprised of alternating double chains of VO_5 pyramids, shown in blue. Figure taken from [68].

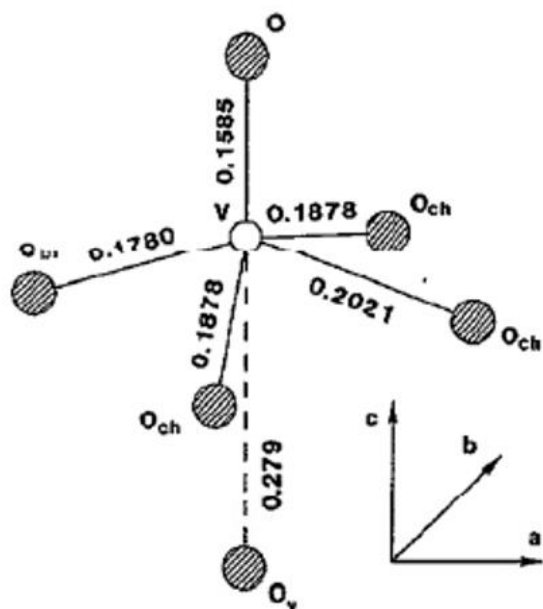


Figure 1.17. The coordination of vanadium ion in V_2O_5 . Figure taken from [69].

There are many consequences of plane-built vanadium pentoxide structure. This property, as well as the fact that the lattice is fairly open and permeable to smaller intercalating cations was used for developing V_2O_5 as a high-capacity ion storage medium in Li-ion batteries. Hermann et al. [70] investigated the surfaces of the van der Waals planes and found them polar and capable for being hydrated. Due to plane structure, also electrical properties are highly anisotropic and V_2O_5 shows significantly higher conduction within the a - b planes. This is a result of shorter distances between vanadium atoms than between the planes. Interesting feature of vanadium pentoxide is fact, that its electrical conduction is dominated by polaron transport, due to local lattice distortion moving together with the conducting electron. This property can be attributed to an anomalously high (n-type) Seebeck coefficient of $-540 \mu\text{V/K}$ [71]. However, because of low mobility of these small polarons, thermal conductivity of V_2O_5 is relatively poor. Another property of V_2O_5 is its electrochromic effect. Due to injection or extraction of charge, V_2O_5 changes its optical properties. It exhibits a transmittance increase in the near-UV region and the blue part of the visible spectrum. Moreover, a transmittance decreases in the near IR region and red part of the visible spectrum [69].

V_2O_5 is known for its catalytic properties. Recently, the system of V_2O_5/TiO_2 bilayer has been deeply investigated. In the '80s, cooperation of several European laboratories analysed and tested this system (called "Eurocat") in the *o*-xylene oxidation. The deposition of vanadium pentoxide on titania greatly influences the reactivity and structure of V_2O_5 . It was proposed [72], that the higher activity is a result of a variation of the bond energy between the catalyst surface and oxygen.

Vanadium dioxide, VO_2 exists as a dark blue solid. In the entire vanadium oxide family, only VO_2 has the transition temperature near the room temperature at 67°C . At room temperature, VO_2 has a monoclinic M_1 crystal structure with lattice parameters $a = 0.573 \text{ nm}$, $b = 0.452 \text{ nm}$, $c = 0.537 \text{ nm}$ and $\beta = 122.60^\circ$ [73]. The M_1 crystal lattice of VO_2 is presented in Fig. 1.18. Doping of vanadium dioxide leads to M_2 monoclinic arrangement. Below the transition temperature, VO_2 is a semiconductor and is highly IR transparent.

Above 67°C , VO_2 has a tetragonal crystal structure, with lattice parameters $a = b = 0.4553 \text{ nm}$ and $c = 0.285 \text{ nm}$. The octahedra is formed by vanadium in a +4 state coordinated to six nearest oxygen atoms. These octahedra are symmetrical and form edge-sharing chains along the c -axis of the crystal. The lattice is characterized by small c/a ratio in comparison to other rutile structured materials. Therefore, adjacent vanadium atom are placed closed together along c -axis. The crystal structure of VO_2 , referred to as the metallic R-phase, is shown in Fig. 1.19.

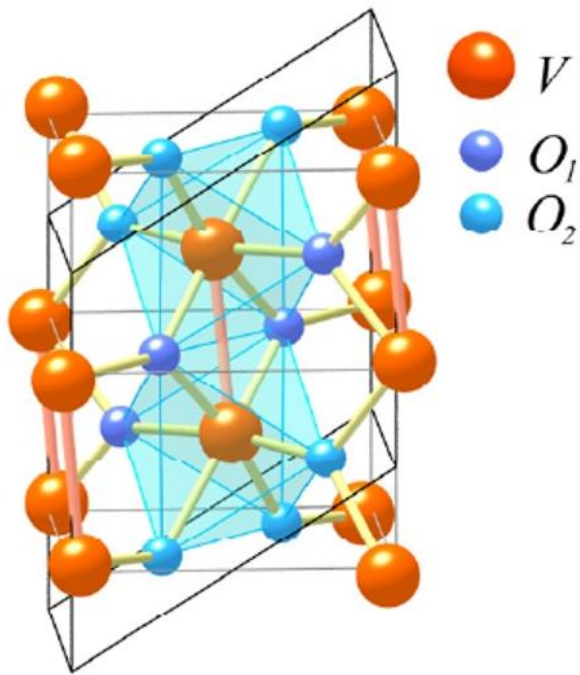


Figure 1.18. Monoclinic M_1 crystal structure of VO_2 [73].

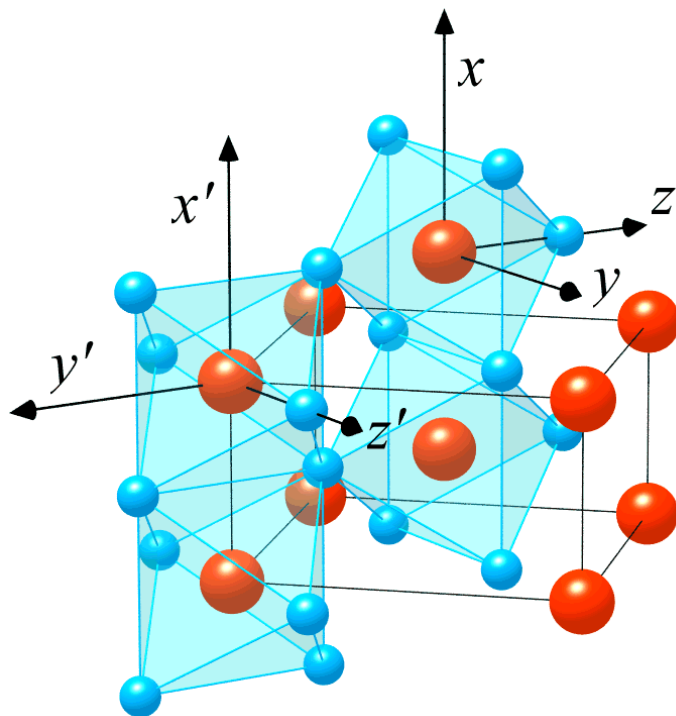


Figure 1.19. The rutile structure of VO_2 . The large red circles represent V^{4+} ions, whereas the small blue circles O^{2-} ions [73].

At the transition temperature 67 °C, VO₂ undergoes the semiconductor-metal transition revealed by a dramatic drop in electrical resistivity of ~5 orders of magnitude. The dramatic change of electrical resistivity is accompanied by an increase of infrared reflectivity. The nature of the transition has been thoroughly investigated. The Mott-Hubbard model of correlated electrons was postulated [74] and/or the model based on molecular orbitals and band structure diagram was suggested [75]. Density functional theory, in particular LDA calculations have been also carried out. The most important question was whether the change in crystal structure induces the electrical changes, or vice versa. The phase transition was found to last at least 80 fs [76], which is almost the half of lattice vibration period. These data indicate that transition is driven by electron-electron correlations, previously suggested Mott-Hubbard model.

Different dopants are used to lower the transition temperature and to modify the physical properties. As an example in Fig. 1.20, the electrical resistivity of (V, Cr)O_x system was shown revealing the large change of the electrical resistivity drop as a function of Cr-doped content [77].

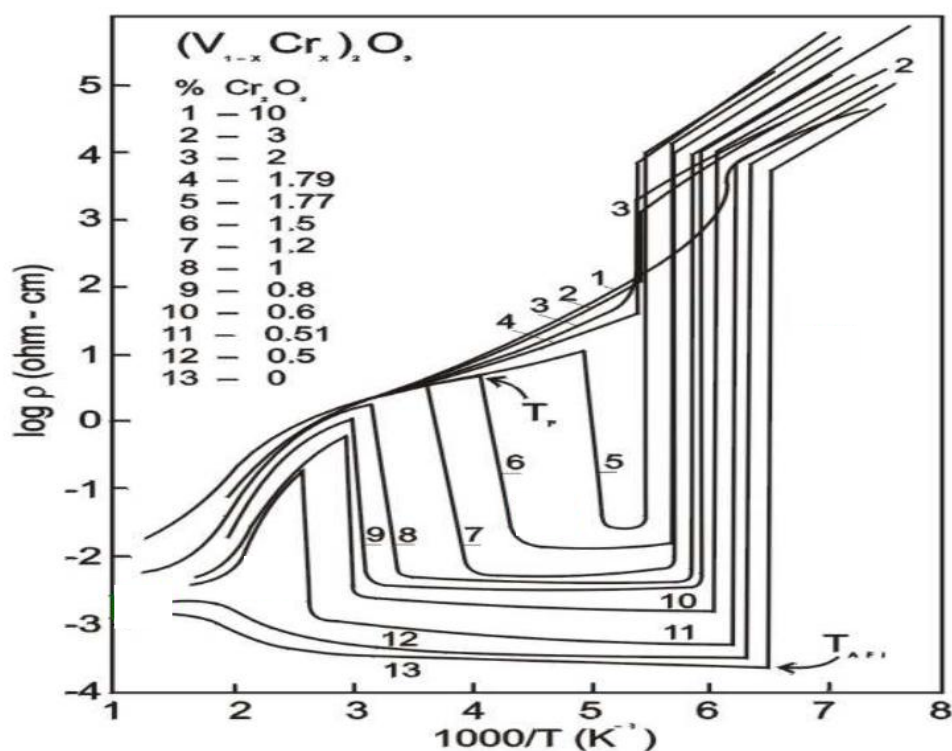


Figure 1.20. Electrical properties of the (V,Cr)O_x system reported by H. Kuwamoto et al. [77].

Different dopants are used to modify optical properties, too. In particular, tungsten doping allows for significant reduce of transition temperature – 2% of W in VO₂ films decreases it to 25 °C [78]. The hysteresis loops for differently doped vanadium dioxide films are presented in Fig. 1.21. Hydrogen charging of crystalline VO₂ also influences the parameters of transitions and shifts the transition temperature toward lower-temperature region [79].

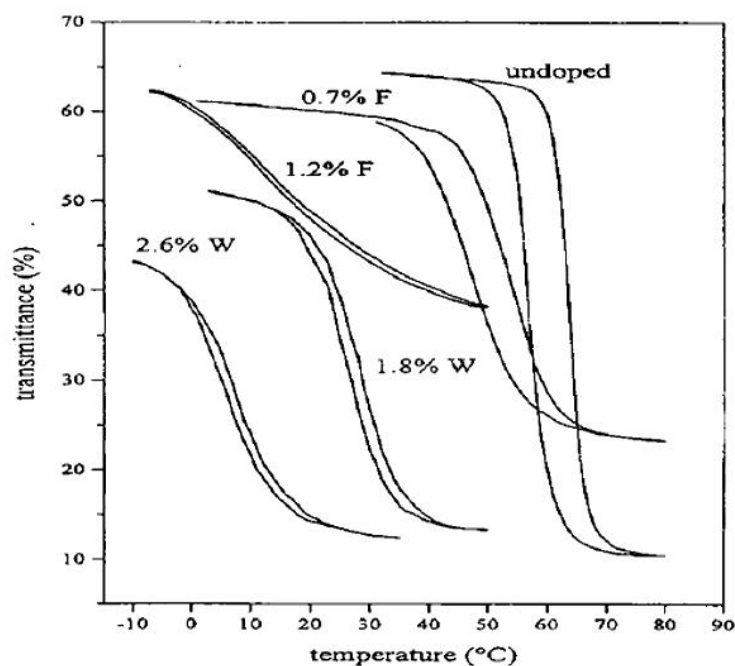


Figure 1.21. Hysteresis loops of optical transmittance for VO₂ layers doped with tungsten and fluorine. Picture taken from [79].

1.3.3 Application of vanadium oxides

The plane structure of vanadium pentoxide, well suited for the intercalation of cations, makes it the efficient material for hydrogen storage. This property is widely used also in Li-ion batteries, which nowadays are the most popular power sources for small electronic devices and are being tested for hybrid electric vehicles. Further improvements of such batteries are still required for large scale applications. Due to its electrochromic properties, V₂O₅ can be used for production of smart windows with adjustable reflectivity. These windows can be used in buildings, cars or aircrafts. Nanostructured V₂O₅ is applied in the fields of sensors, catalysis in organic reaction and actuators. It is commonly used for production of sulfur acid. Moreover, it is used as precursor for other vanadium salts and in the preparation of bismuth vanadate ceramics, used in solid oxide fuel cells [80]. V₂O₅ can be

also used as a detector material in bolometers and microbolometer arrays for thermal imaging, thanks to its high coefficient of thermal resistance. Thermochromic properties of V_2O_5 allow it to be applied as temperature sensors and Seebeck elements. Additionally, it can be used as an ethanol sensor in ppm levels (up to 0.1 ppm). Recently, V_2O_5 nanoribbons and nanotubes are investigated for applications as biosensors and bioassays [81].

VO_2 , due to the dramatic change of its physical properties at easily and commonly reachable temperature, has been intensively studied for industrial applications. Increase of IR reflectivity allows VO_2 to be applied as a window coating, which helps in regulating heat transmission inside buildings or cars. Moreover, it is used as extremely fast optical shutters and optical modulators. In army, VO_2 is used as a laser protective device [82] and infrared modulators for missile guidance systems. Change of electrical resistivity is a feature, which is applied in many electronic devices, such as variable resistors (varistors), for data storage and memory devices.

1.4 Ti-TiO_x and V-VO_x thin films

The Ti-TiO₂ and V-VO_x bulk systems, as well as their hydrogen-charged ones, have been investigated [57,83-85]. Their thin films and multilayers, and in particular the behaviour of hydrogen in them, are still interesting research topics especially the enhanced changes of the properties as a function of size-reduction of the systems.

1.4.1 Ti-TiO_x thin films

Recently, titanium thin films are successfully applied as material for improvement of steel mechanical properties or in medical tools. Thin films of titanium hydrides are being investigated for applications e.g. in electronics.

The main characteristic of physical properties of titanium thin films, and comparison with bulk titanium after hydrogen charging is included in work of E. Tal – Gutelmacher et.al [84]. Stress measurements showed that hydrogen built up in titanium crystal lattice led to increase of crystal lattice volume. As a result, a strain of -1.75 GPa occurred, as well as plastic deformation processes for higher hydrogen concentrations. Changes of crystal structure are shown in Fig. 1.22. It is visible, that at H/Ti = 0.4 the second peak appears at 40.8°, what is related to appearance of the another phase and presence of two-phase region. Further hydrogen charging caused disappear of the peak related to α phase at H/Ti = 0.7. The peak related to hydride phase appeared. However, for α phase region, relative expansion of interplanar spacing, d , with hydrogen absorption in Ti α -phase is linear. This is also indicated by the shift of the broad (0002) titanium peak toward lower diffraction angles.

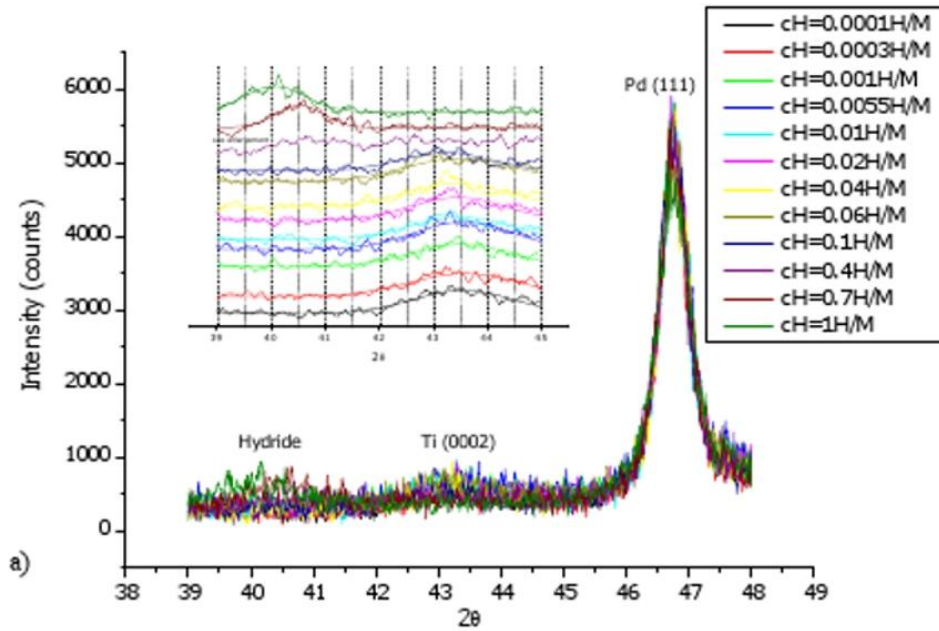


Figure 1.22. XRD result of titanium film with different hydrogen concentration. Results of the work in ref. [84].

Influence of hydrogen on titanium crystal lattice is visible also in electrical resistivity of this metal. For small amounts of hydrogen, up to $H/Ti = 0.1$, hydrogen forms a disordered interstitial solution in titanium lattice, and hydrogen atoms are additional scattering centers for conducting electrons. These results in increase of resistivity. Increasing the hydrogen concentration and formation of ordered β phase leads to decrease of resistivity. This happens because contribution of additional conducting electrons, gained to conducting gas from hydrogen, is larger than scattering on protons in crystal lattice. The dependence of electrical resistivity in a function of hydrogen content [85] is plotted in Fig. 1.23.

The changes of resistivity of titanium after hydrogen charging is recently widely used in electronics. Thin titanium films are applied as the adlayers improving the Embedded – Nonvolatile Memories (NVMs). In their work, Walczyk et al. [86] investigated bipolar resistive switching in $TiN/HfO_2/TiN$ devices. The thin Ti layer were deposited either on top, or on the bottom of HfO_2 layer. Hysteretic current-voltage characteristics have been studied by the *dc* voltage sweep measurements with 1000 cycles for both cases. The results are presented in Fig. 1.24. As it is clearly visible, only for Ti top adlayer the hysteresis was obtained, whereas a Ti bottom adlayer integration did not show any resistive switching effect. For a Ti top layer, applying positive voltage until specific value V_{set} leads to decrease of resistance, and negative voltage beyond the value of V_{reset} may cause drop of current to zero. XPS spectra for these multilayers reveals an increased nitrogen- and oxygen-gettering activity at the Ti top adlayer/ HfO_2 interface.

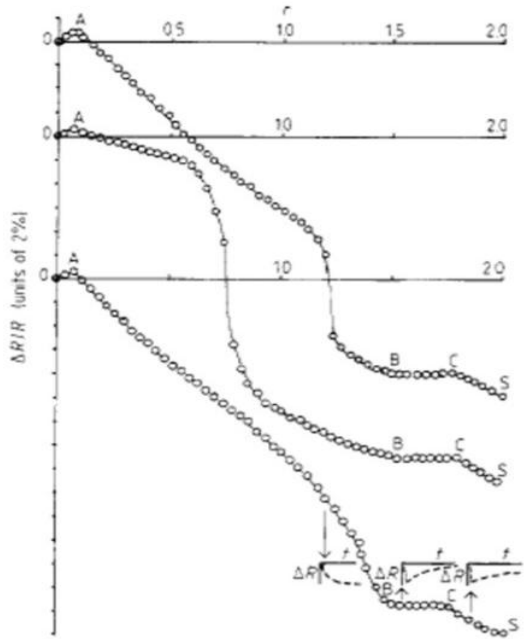


Figure 1.23. Resistivity measurements for titanium films of different thickness with different hydrogen concentration. Results taken from [85].

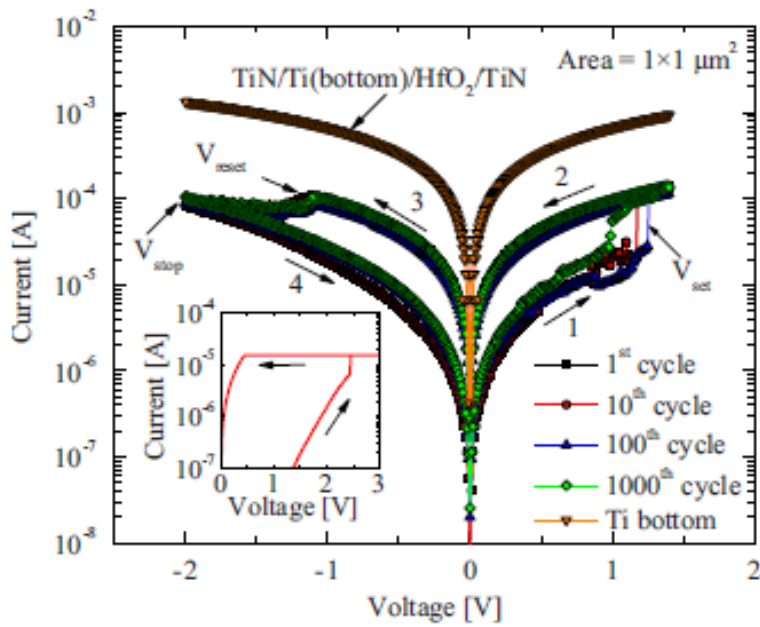


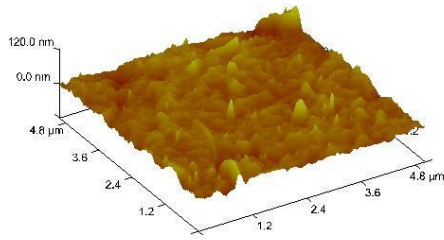
Figure 1.24. *I-V* characteristics of a TiN/HfO₂/TiN multilayer after 400 °C thermal treatment with Ti layers under and below HfO₂ layer. Arrows indicate sweeping directions [86].

Due to its relatively wide band gap of about 3.0 eV, TiO₂ thin films are transparent to visible light. Very high refractive index of about 2.5 combined with exceptional abrasion resistance and chemical inertness were extensively exploited in the optical coatings for laser mirrors, interference filters, etc. Thin films of TiO₂, are recently applied as a material used during the processes of pollution elimination by photocatalytic decomposition. They are also used in air-conditioner filters, especially these in the public places. TiO₂ layers are sputtered onto sound-absorbing screens and concrete roads, as well as on ceramic materials used in industrial constructions, as self-cleaning windows, non-sweating mirrors or wall tiles [87]. Moreover, Kawasaki et al. [88] examined TiO₂/TiN/TiO₂ multilayers and proved their UV-photocatalytic properties. Due to them, TiO₂/TiN heat mirrors are expected through the precise control of the composition of the top TiO₂ layer to become a self-cleaning material.

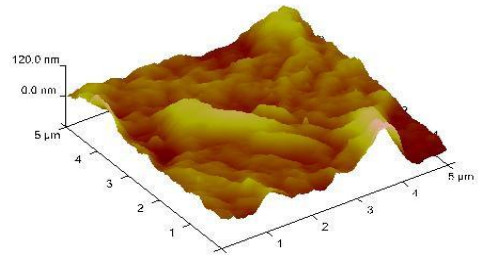
1.4.2 V-VO_x thin films

Vanadium oxide thin films have found applications especially as optical and electrical devices. Recently they are applied in electrochromic devices (ECDs) as counter electrodes, or passive lithium reservoirs. V₂O₅ thin films, as a wide band gap and n-type semiconductor materials, are also widely investigated due to their interesting electrochemical performance. Han et al. [89] investigated V₂O₅/V/V₂O₅ multilayers properties, considering their application for uncooled microbolometers. They found that annealing of such systems in oxygen atmosphere leads to phase mixing and significantly improves electrical properties, what allows for industrial application. On the other hand, Cele [90] reported annealing of V₂O₅ films and found, that film annealed at 300 °C tends to peel in some places. This could be due to stress that develops during the annealing process, which causes the film to peel off. The sample annealed at 800 °C shows the increase of particles on the surface. This shows that as the temperature is increased, the roughness of the film increases as well. The AFM results are presented in Fig. 1.25. Moreover, annealing of V₂O₅ films in Ar-H₂ mixture leads to reduction of vanadium pent-oxide and occurrence of other Magneli phases with lower oxygen stoichiometry. XRD patterns for V₂O₅ film annealed at temperature range between 300 °C and 900 °C are shown in Fig. 1.26. The V₂O₅ (001) peak at the approximate 2θ of 41.8° appears in all the annealing temperatures. This peak is decreasing in intensity and starts to disappear when film is annealed in temperature range between 500 °C and 900 °C. The V₃O₇ peak was found at the approximate 2θ of 29.1° which follows the as deposited samples. The broadness and intensity of the peaks were varying. The V₆O₁₃ peak was found from the 700 °C and 800 °C samples at the approximate 2θ of 54.7°. and the V₄O₉ peak was found around 2θ of 31.7°.

a)



b)



c)

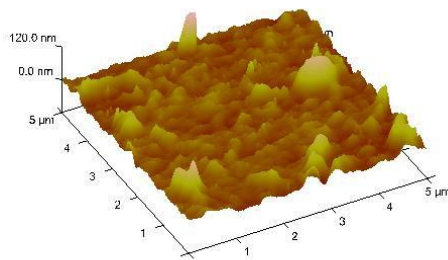


Figure 1.25. The AFM images of the V_2O_5 film annealed in H_2+Ar atmosphere. (a) As-deposited film, (b) annealed at 300 °C, (c) annealed at 800 °C [90].

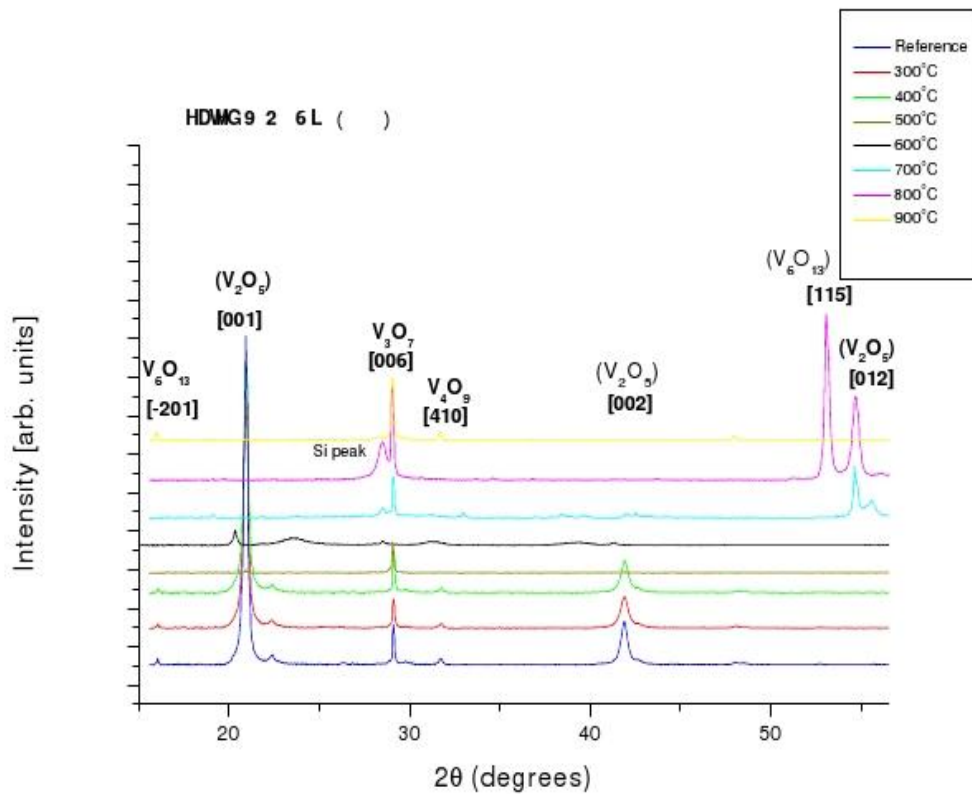


Figure 1.26. XRD data for V_2O_5 thin film annealed in $Ar+H_2$ atmosphere at different temperatures [90].

Ultra-thin V_2O_5 layers are used as the model systems of gas sensing surfaces and in sensors of aromatic hydrocarbons [91,92], when are combined with SnO layers. Vanadium pent-oxide reveals very high lithium insertion capability (theoretically up to two equivalent of lithium per vanadium), what makes the V_2O_5 films very promising candidates for a cathode in high-capacity Li batteries. Other vanadium oxides, V_2O_3 and VO_2 reveals thermotropic switching properties when the characteristic temperature is obtained. Thin films of such vanadium oxides are used to control transmittance and infrared emissivity of a glazing.

VO_2 films have been widely investigated as a potential candidate for application in industry of coatings to conservation of energy. Recently they are used as window coating or as laser protective device, because they can help in regulating heat transmission (IR) in buildings or vehicles. The idea is presented in Fig. 1.27. Because such coatings require extremely high smoothness, dependence of VO_2 films roughness on different conditions were also investigated. It was found, that the electrical and optical switching of VO_2 thin films depends on the synthesis conditions of the deposition technique and its parameters. For example, an increase in deposition temperature gives rise to an increase in grain size and causes deterioration of the orientation (texture) of the grain, and, consequently, results in decreases of the optical and electrical properties of the film. Results reported by Chen et al. [93] show, that the metallic phase exceeds the semiconducting phase in the infrared region independently on temperature if the film thickness is lower than 100 nm.

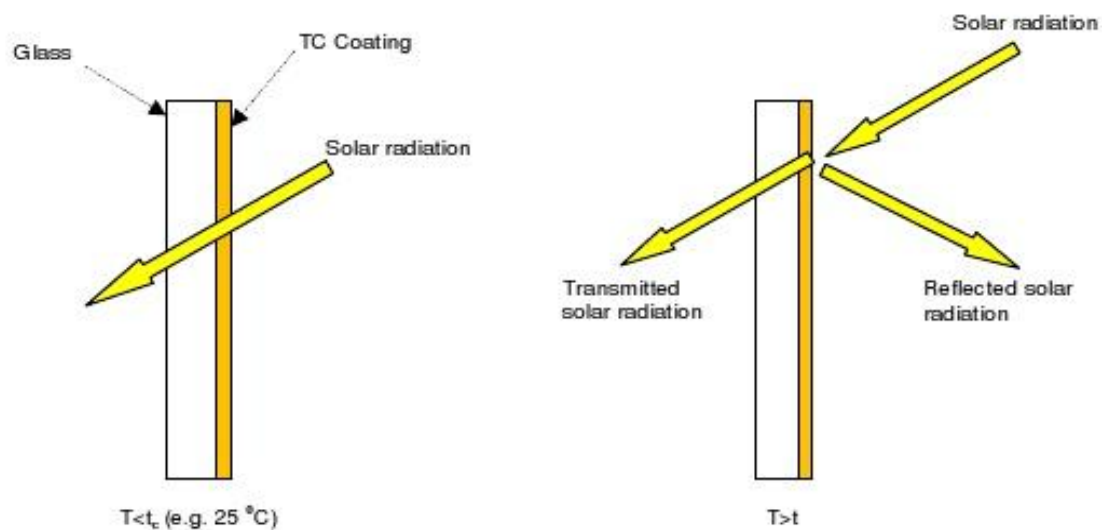


Figure 1.27. Principle of operation of heat-regulating mirrors [90].

Msomi et al. [94] investigated changes in optical properties for VO₂ films produced at different temperatures (450 °C, 500 °C and 550 °C). Fig. 1.26 presents the hysteresis loops of optical transmittance of VO₂ thin films obtained at different deposition temperatures at fixed wavelength of 1100nm. Vanadium dioxide film deposited at 450 °C exhibits higher transmission switching efficiency than films produced at higher temperatures. For this film, the hysteresis width is about 5 °C, whereas films deposited at 500 °C and 550 °C reveal the width of about 10 °C. Moreover it was shown, that transition temperature slightly decreases when deposition was performed at higher temperatures. It was suggested, that higher deposition temperatures cause increase of grain size and their random arrangement and it results with this decrease.

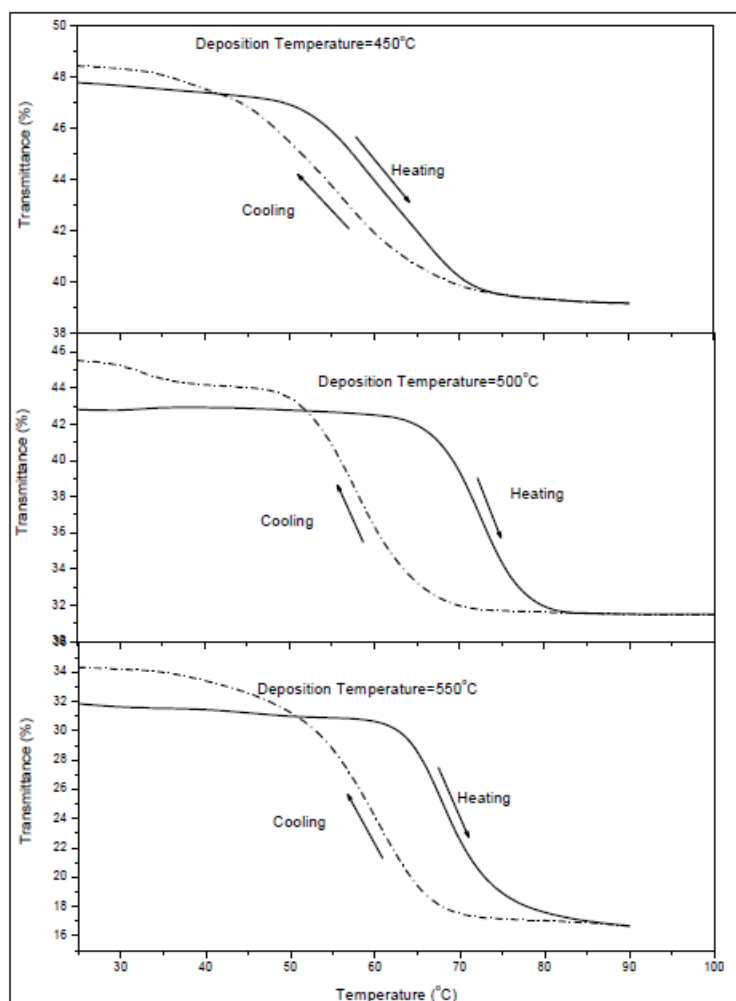


Figure 1.28. Optical transmittance of VO₂ thin films deposited at different temperatures, for a wavelength of 1100 nm [94].

1.4.3 TiO₂ – VO_x Thin films

Despite of extensive investigations of VO_x thin films, a large interest is still focusing on modification of such systems to gain the optimal and desired properties suitable for technical applications. It is expected that the mixture of TiO₂-VO_x films as well as deposition of VO_x films on TiO₂ substrates can strongly modify their properties [95]. The interaction of V₂O₅ with TiO₂ would affect the structural properties and reactivity. Interaction/interchange of oxygen atoms between V₂O₅ and TiO₂ would lead to dispersion of vanadium and formation of two-dimensional structure [96]. Such theoretical multilayer is defined as the amount of V₂O₅ units necessary to completely cover the TiO₂ surface (0.146 wt% of V₂O₅ per m² of TiO₂ substrate) [97]. Vanadium dispersion have been described by several hypotheses. According to Vejux and Courtine [98], the preferential interaction takes place between (010) planes of V₂O₅ and (001) planes of TiO₂ anatase, what results with increase of surface density of V=O groups. Such phenomena can find application e.g. in active sites for *o*-xylene oxidation. Other approach was proposed by Kozłowski et al. [99], who explained the dispersion of V₂O₅ by chemical reaction between vanadium and titanium oxide. This reaction leads to formation of isolated and polymeric vanadium species. As it was reported by Haber [100], during this reaction formation of VO₄ units, with two terminal oxygen atoms in the V=O group and two bridge oxygen atoms in the V-O-Ti group takes place.

Three different vanadium species on TiO₂ surface can be obtained depending on vanadium content in vanadium oxide, as presented in Fig. 1.29:

- 1) Monomeric and isolated tetrahedral VO_x species, strongly bounded to the TiO₂ anatase substrate, are observed at low vanadium content (~10 % of the monolayer),
- 2) Polyvanadates – polymeric [VO_x]_n species, weakly bounded to TiO₂ substrate, observed from ~20 % of the monolayer and
- 3) Amorphous or crystalline V₂O₅, observed from 1 complete monolayer [101].

These different vanadium species reveal different catalytic performances. It was found, that polyvanadates are more active than pure vanadium in bulk vanadia, and for lower vanadium concentrations the terminal V=O oxygen is more active than the bridged V-O-Ti oxygen [102]. Moreover, Silvia [103] showed, that monomeric vanadyl is the most active specie in the selective oxidation of toluene to benzoic acid, and this specie is also responsible for catalytic activity of V/Ti/O.

Thermochromic properties of VO₂ films as well as TiO₂/VO₂/TiO₂ and TiO₂/VO₂/TiO₂/VO₂/TiO₂ multilayers have been studied by Mlyuka et al. [104]. The results of spectrophotometrical measurements of transmittance for VO₂ film and TiO₂/VO₂/TiO₂ multilayer, below and above the transition temperature of VO₂ (at 20 °C and 100 °C) are presented in Fig. 1.30 (left). Fig. 1.30 (right) shows results of the same measurements for VO₂ and TiO₂/VO₂/TiO₂/VO₂/TiO₂. It is clearly visible, that multilayers of VO₂-TiO₂ have

significantly higher luminous transmittance in comparison to single VO₂ film. Moreover, TiO₂/VO₂/TiO₂/VO₂/TiO₂ multilayer could yield a large change of solar transmittance, for temperatures below and above transition temperature of VO₂.

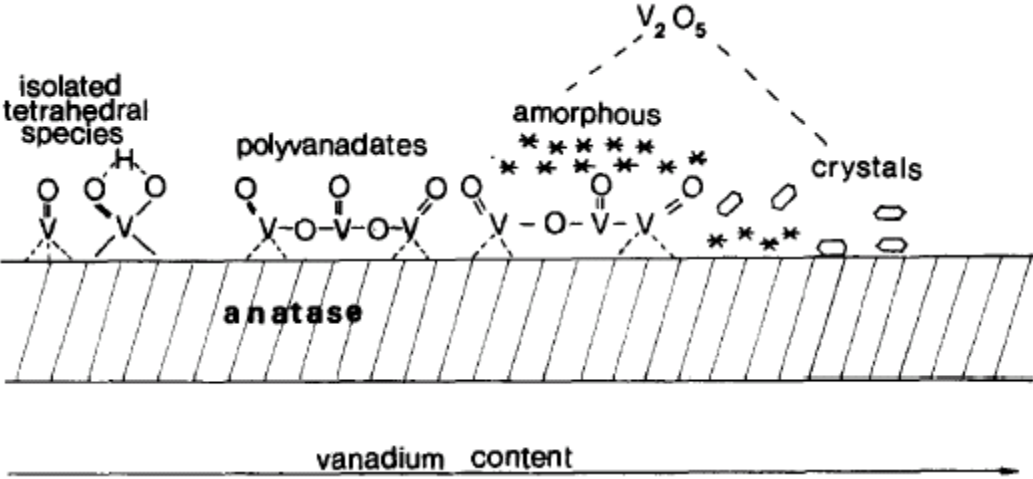


Figure 1.29. Vanadium species on TiO₂ anatase substrate [103].

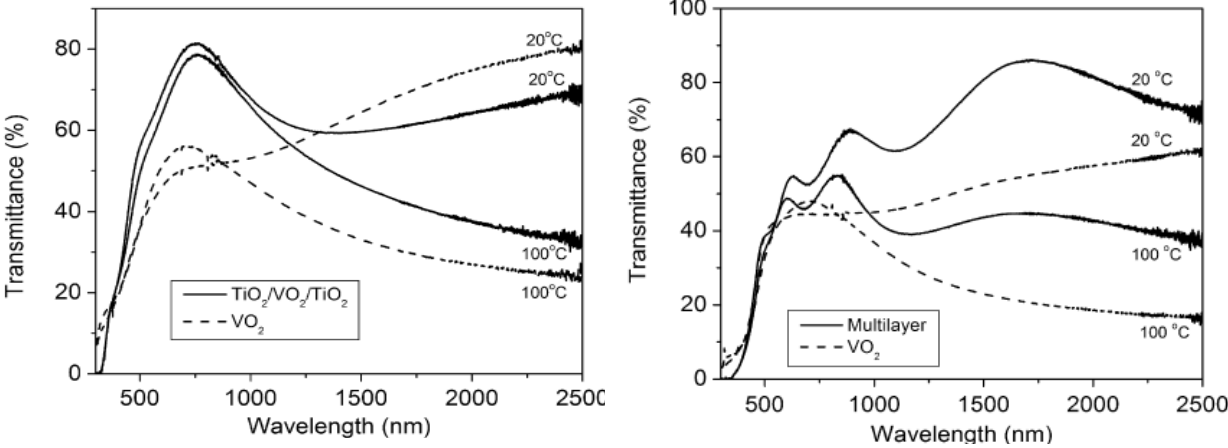


Figure 1.30. Spectral normal transmittance of VO₂ compared with TiO₂/VO₂/TiO₂ multilayer (left) and TiO₂/VO₂/TiO₂/VO₂/TiO₂ multilayer (right), for temperatures below and above metal-insulator transition temperature of VO₂. Figures taken from [104].

The TiO₂-based thin films have been extensively investigated for photocatalytical applications and gas sensors in the group of Prof. K. Zakrzewska in AGH University, Krakow. The general overview in this subject as well as the work done by the AGH group can be found in refs. [105-108]. In fact all the films included in this work have been prepared and investigated in the scope of close cooperation with her group.

1.5 Nickel as a dopant

It was shown, that the transition metal elements like Ti, V and Ni would act as a catalyst for the hydrogen absorption on the e.g. Mg surface and would improve the kinetics of hydrogen absorption [109,110]. Ouyang et al. [111] have investigated the MgNi/Pd thin films and found that the hydrogen absorption and desorption content reached respectively 4.6 wt.% and 3.4 wt.% at room temperature. Mixing vanadium and titanium with other metals, like Zr and Ni was found to allow obtaining a relatively high hydrogen capacity [112,113].

Hydrogen diffusivity can be highest for *bcc*-lattice metals (tetrahedral interstitial sites), lower for *fcc*-lattice metals and smallest in case of CsCl-lattice materials (both with octahedral sites). Smaller diffusivities are correlated with larger distances d between the nearest-neighbour interstitial sites in lattices, which correspond to higher energy barriers between the interstitial sites and, consequently, to higher activation energies for hydrogen diffusion. A comparison of hydrogen diffusivity coefficients for several metals is presented in Fig. 1.31.

The hydrogen-to-metal atom ratio (x) for several metals [114], under equilibrium conditions, as a function of the reciprocal temperature in presence of a hydrogen gas pressure of 1 bar is shown in Fig. 1.32. The corresponding values of the enthalpy of solutions is also given. Titanium and vanadium have a high and positive value of enthalpy, while nickel (having *fcc* crystal lattice) possesses a small and negative enthalpy (-0.16 eV). Thus from the first sight, nickel does not seem to be an interesting candidate for application in hydrogen economy. On the other hand, it is worth studying the systems with nickel as a dopant, since it implies a slight change of their properties and/or optimize some properties for specific applications. For instance, Ni-Ti alloys (with CsCl crystal structure) are widely used in electronics as shape memories. Hydrogen charging of Ni-Ti system affects its electrical properties [115]. D. Cauceglia et al. [116] compared Ti-V-Ni and pure vanadium layers and their hydrogen kinetics. Their results present nearly the same hydrogen storage capacity of ~1 wt% for Ti-V-Ni as for pure vanadium and mechanically alloyed V-C. However, temperature and pressure required to obtain such capacity in case of Ti-V-Ni was significantly lower and the kinetics was faster.

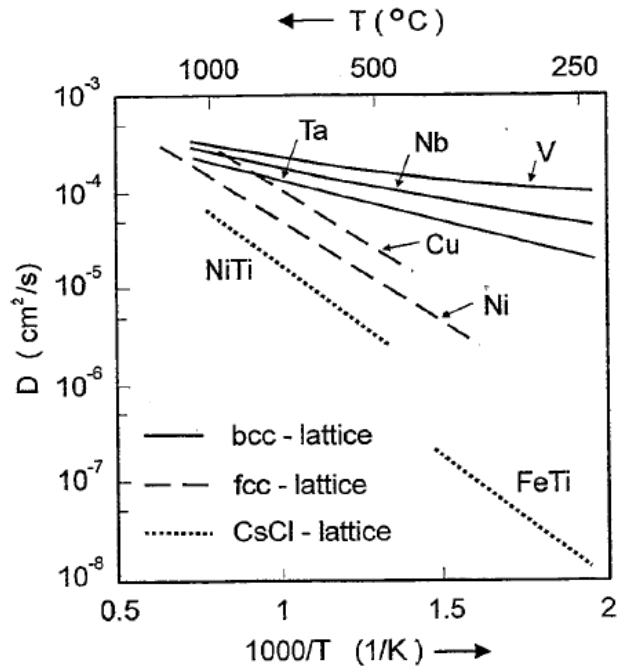


Figure 1.31. Arrhenius plot of the diffusion coefficient D of hydrogen in metals with *bcc*, *fcc* and CsCl structures [114].

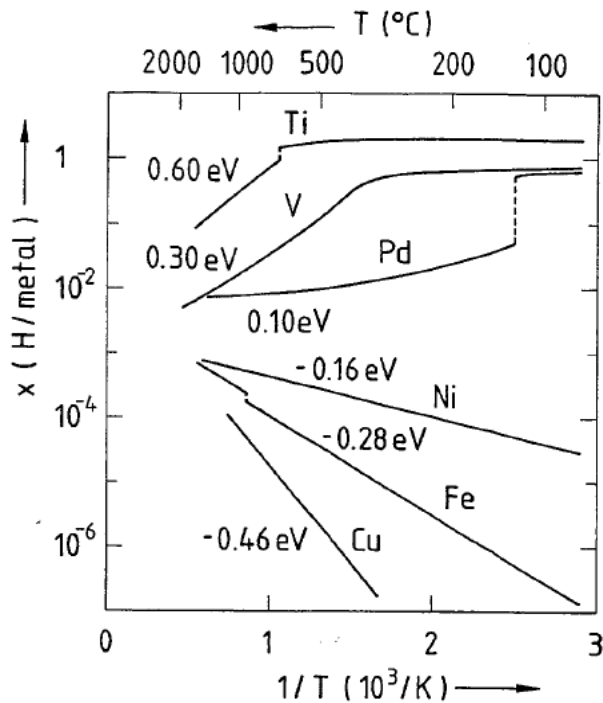


Figure 1.32. Hydrogen to metal ratio (x) obtained for several metals a function of the reciprocal temperature ($1/T$) in presence of a hydrogen gas pressure of 1 bar. The corresponding values of the enthalpy of solutions are also given [115].

Chapter 2

Samples preparation and experimental techniques

In this chapter the sample preparation and the hydrogenation process will be described first. The samples have been characterized and investigated by a wide variety of techniques which could be divided into two groups: 1) the standard techniques for material characterization such as HRSEM, XRD, XRR and RBS and 2) the techniques specially for description of hydrogen and its behaviour in the materials such as SIMS and N-15.

2.1 Samples preparation

The titanium and titanium dioxide thin films were prepared in a planar, balanced, self-made magnetron sputtering system located at the Department of Electronics, Faculty of Computer Science, Electronics and Telecommunications, AGH University of Science and Technology, Kraków. The scheme of this system is shown in Fig. 2.1. A detail description of the system has been published elsewhere [117-119].

The Titanium target of purity 99.99% (4N) was sputtered either in high purity argon (for Ti layer deposition) or in Ar+O₂ reactive gas atmosphere (for TiO₂ layer deposition). Gases were introduced into the chamber individually through separate gas admission lines.

Substrates for film deposition were placed on a rotatable holder at a distance of 35 mm below the target. Up to 8 samples could be obtained in one deposition cycle without breaking the vacuum condition, thanks to a special construction of the shutter. The substrates prior and during deposition were heated up to 250°C to provide good thickness homogeneity and film crystallinity. An oil diffusion pump evacuated the chamber and the obtained vacuum was of $2 \cdot 10^{-5}$ mbar. The magnetron discharge was driven by a *dc* pulse power supply (Dora Power System—DPS) the details of which are given in [119]. The substrate holder was at the ground potential, no bias was applied, the cathode current was stabilized at 2 A. The power for each deposition run was maintained at 0.9 kW. A closed-loop system with the optical control of plasma emission (optical emission spectroscopy (OES)) was used to stabilize the deposition rate in the intermediate region between the two stable sputtering modes: metallic and reactive. The system is based on a continuous monitoring of the intensity of a chosen plasma emission line I_{Me} which is a result of de-excitation of metal species during the sputtering process. Light extracted from the plasma ring is transmitted via an optical fiber to the SPM2 Zeiss monochromator (M). Photomultiplier (PM) is applied to detect the intensity I_{λ} of light at a given wavelength. Then I_{λ} is served as a feedback signal for admission of the reactive gas in the flow regulation via electromagnetic valve (EV).

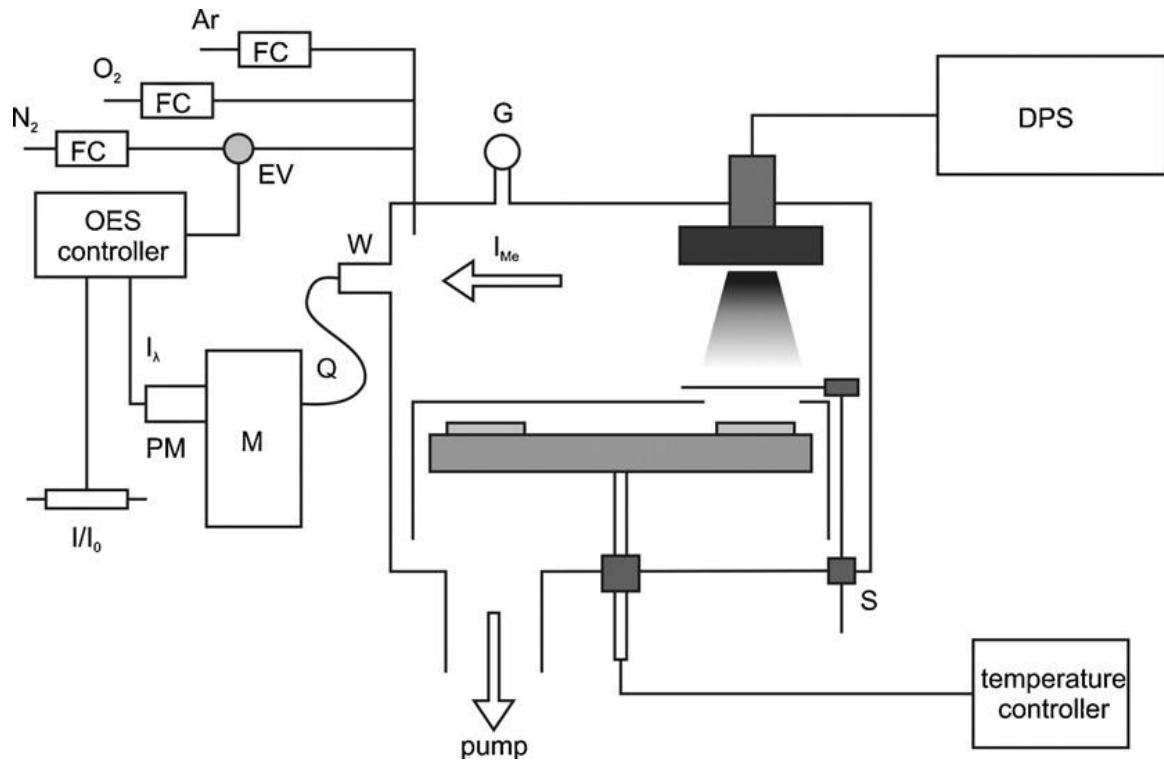


Figure 2.1. Scheme of magnetron sputtering system. DPS – pulse power supply, FC- gas admission lines, OES – optical emission signal controller, W – optical window, Q - optical fiber, M/PM - monochromator/ photomultiplier, EV - electromagnetic valve, MKS – gas flow controller [120].

The relative ratio of intensity I/I_0 of Ti emission line at wavelength of 500 nm is used as a parameter controlling the sputtering rate during deposition of oxides, through its influence on the state of target poisoning. I_0 corresponds to the intensity of the same emission line for deposition of Ti in a pure metallic mode (at 100% of Ar). The ratio I/I_0 is an indirect measure of the Ti species flux which arrive at the substrate. Thus, low value of the ratio reveals low sputtering rate of Ti target in gases-rich atmosphere. For a given deposition process, gas flows of argon (for Ti layers) η_{Ar} and oxygen (for TiO_2 layers) η_{O_2} were set up at constant values by MKS gas flow controllers. The layer thicknesses during deposition is controlled by time measurements.

One series of films was subjected for an additional Pd covering. Namely, after titanium and titanium dioxide layer deposition, they were partially (about 1/3 of the film surface) covered by 20 nm-thick palladium layer by Molecular Beam Epitaxy (MBE) technique. Palladium target was put into alumina effusion cell, wrapped in tungsten wire. The applied current, due to Joule-Lentz's heating, caused Pd evaporation and deposition on Ti or TiO_2 layers. The MBE growth process was performed in an ultra-high vacuum (UHV) of $1.5 - 6.0 \cdot 10^{-9}$ mbar. The layer thickness was controlled *in situ* using a quartz crystal microbalance. The duration of Pd deposition with a layer thickness of 20 nm was about 1400s.

Such a MBE growth of the Pd layer was carried out by using the MBE equipment located at Department of Materials Science, Institute of Nuclear Physics PAN, Krakow.

Vanadium oxide films were deposited by rf reactive sputtering from metallic V target in Ar+O₂ flow controlled gas atmosphere. Prior to the deposition process, the target pre-sputtering in Ar+O₂ was performed to stabilize the sputtering conditions and to equilibrate the oxidized target surface. Deposition run was carried out under the predefined conditions of the total gas pressure, constant oxygen (2.0 cm³/s) and argon (6.7 cm³/s) flows, constant input power (220 W) and voltage (1350 V) as well as the controlled substrate temperature ($T_{\text{sub}} = 298 \text{ K}$).

2.2 Hydrogenation

Two different hydrogenation processes were employed in this work. The hydrogen charging process at 1 bar and at temperature of 300 °C was performed in self-made gas charging system at the Institute of Materials Science, Technische Universität Darmstadt. The samples were put into a glass tube and the tube was placed in the charging system consisted of vacuum system and an electric oven. The vacuum of about 10⁻³ mbar was obtained by rotary vane pump. The annealing was performed using an electrical oven which could be heated up to 1600 °C. The temperature was measured *in-situ* during charging process by a Dual Data Logger thermometer with a RS 1316 thermocouple produced by TES Electrical Electronic Corp. The glass tube was filled with hydrogen and then pumped again. It was repeated several times to ensure the cleanness of the hydrogen atmosphere in the tube, before it was heated up to the required temperature.

The hydrogenation of selected Ti-TiO₂ films at high pressure was carried out in the hydrogenation apparatus at the Department of Condensed Matter Physics, Charles University in Prague. The samples was exposed to H₂ gas up to 102 bar in a reactor for hydrogenation. Fig. 2.2 shows a schematic drawing of the hydrogenation equipment [121].

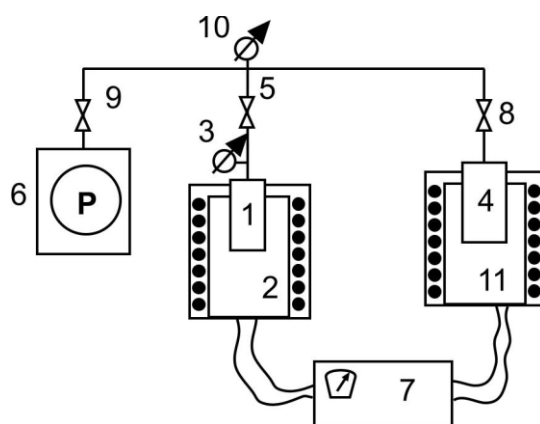


Figure 2.2. Scheme of the hydrogenation equipment (high-pressure part): 1 – reactor; 2, 11 – furnaces; 3, 10 – vacuum-meters; 4 – LaNi₅H₆ container; 5, 8, 9 – valves; 6 – vacuum pump; 7 – temperature control units [121].

2.3 High-resolution SEM

A scanning electron microscope (SEM) is a type of electron microscope in which the image of the sample surface is a result of interactions between focused beam of accelerated electrons with the electrons in the material. SEM is used for various purposes: topographic studies, microstructure and chemical analysis as well as for elemental mapping. Depending on investigated material, SEM can work with high vacuum, low vacuum or even in wet conditions when environmental specimen are observed.

2.3.1 Scanning process and image formation

The typical SEM construction is shown in Fig 2.3. An electron gun, fitted with a tungsten or lanthanum hexaboride filament cathode, thermionically emits an electron beam. The cathodes are usually produced of tungsten due to its highest melting point and lowest vapour pressure among all metals. The emitted electron beam with an energy ranging between 0.2 keV to 40 keV becomes focused to a spot with a diameter size 0.4 – 5 nm by condenser magnetic lenses. Then the beam passes through scanning coils or deflector plates in the electron column. They are used in the final lens and allow for beam deflection in the x and y axes.

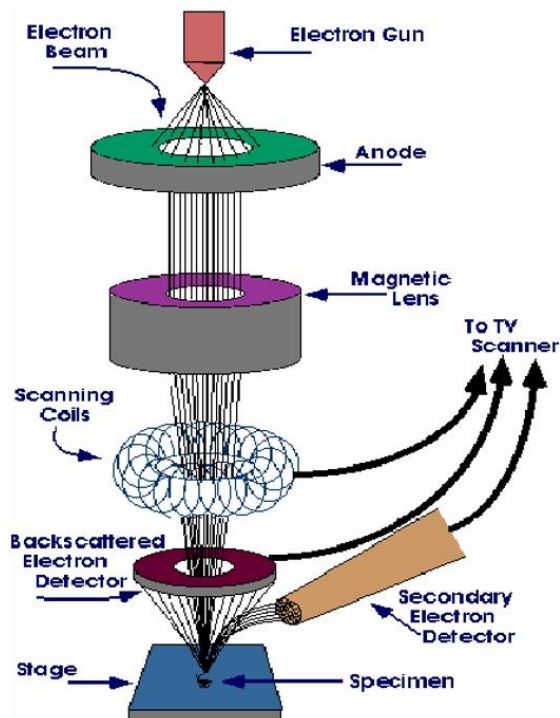


Figure 2.3. Scheme of scanning electron microscope (SEM) [122].

The specimen, or at least its surface, has to be electrically conductive. In case of non-conductive samples, they are coated with ultrathin layer of conductive material (typically gold, platinum or graphite). To prevent the accumulation of electrostatic charge, the sample and holder have to be electrically grounded. The primary electrons interact with the sample; decelerate and lose energy by inelastic transfer to atomic electron and lattice. These processes take place within the interaction volume – a teardrop shaped volume of the sample, as presented in Fig. 2.4. The size of the interaction volume is typically $1\mu\text{m}$ in average, but strongly depends on the electron landing energy and the atomic number and density of sample material. Thus, it can achieve the sizes less than 100 nm or even around few micrometers. Fig. 2.4 presents also the possible results of the energy exchange between the electron and sample: interaction of high-energy electrons by elastic scattering, emission of secondary electrons by inelastic scattering and the emission of electromagnetic radiation. The signals are amplified by electronic amplifiers and displayed on a monitor or TV scanner. Moreover, the position dependent electric current can be registered, amplified and displayed on a monitor or TV scanner as well as the other registered signals.

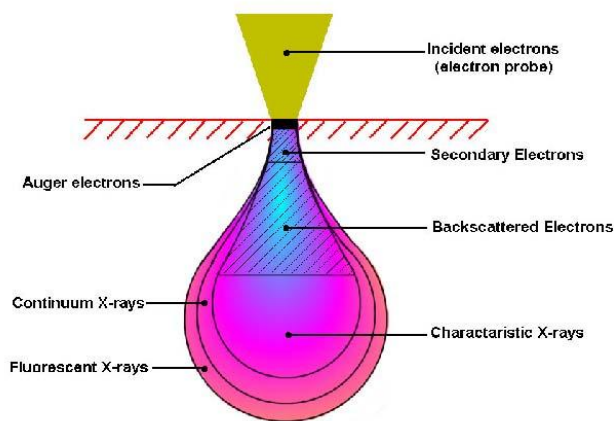


Figure 2.4. A teardrop shaped interaction volume of electron beam [123].

Electron Beam Interaction Diagram

2.3.2 SEM resolution

The resolution of obtained images depends on the sizes of electron spot and the interaction volume. Because both of these quantities are dramatically larger than the distance between atoms, resolution of electron microscopes is too small to observe the atoms. Moreover, the spot size is related to wavelength of electrons and the electron-optical system generating the scanning beam. On the other hand, SEM is a very useful tool for imaging the large areas of the specimen and bulk materials. The resolution for typical SEM instrument is between 1 and 20 nm. The highest resolution of 0.4 nm (at the voltage of 30 kV) was achieved with the Hitachi S-5500, whereas at low beam energies (1 kV) the Magellan XHR obtained the resolution of 0.9 nm.

The high resolution SEM images presented in this Thesis were obtained at the Institute of Materials Science, Technische Universität Darmstadt with Philips XL 30 FEG microscope with field emission electron gun.

Cross-section and surface images of chosen Ti-TiO₂ films were also obtained by Scanning Electron Microscopy SEM for thin films using a Hitachi SU-70 apparatus at the Institute of Physics, PAN in Warsaw.

2.4 X-ray Diffraction

X-ray Diffraction (XRD) is a versatile, non-destructive technique that reveals detailed informations about the crystallographic structure of investigated material. This method allows for qualitative and quantitative analysis. Qualitative analysis is applied for identification of phases in a specimen by comparison with the reference pattern, determination of phases amount, as well as estimation of proportions of different phases. Quantitative analysis determines the structural characteristics and phase proportions with numerical precision [124].

2.4.1 Physical background

X-rays are produced during interaction of electrons with energy in the range 10-40 keV with the metal target inside the X-ray tube. The maximum energy of the produced X-ray photons is limited by the energy of incident energy. When a monochromatic X-ray beam with wavelength λ is projected onto a crystalline material at an angle θ , the diffraction of the beam is possible if the following condition is fulfilled: the distance travelled by the rays reflected from successive planes differs by integer multiple of the wavelength of the radiation. as shown in Fig. 2.5.

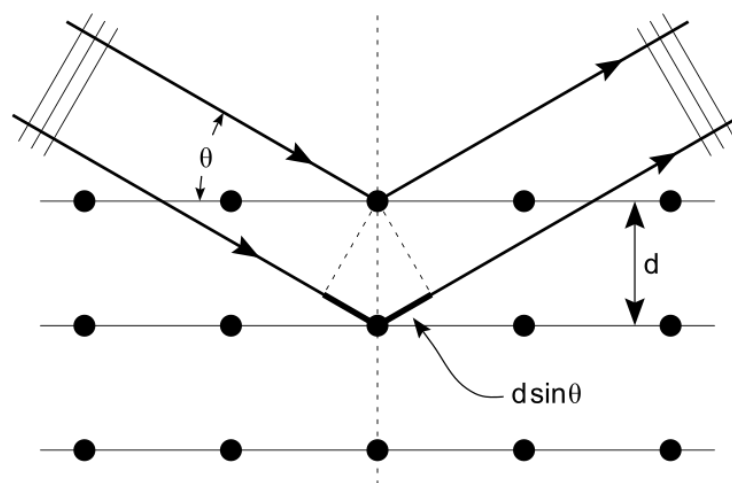


Figure 2.5. Scheme of X-ray interaction with crystal planes.

The atoms in the crystal lattice are arranged periodically, thus the X-rays diffracted beam can constructively interfere. The condition for it was determined by Sir William Lawrence Bragg in 1912, the so-called the Bragg's law:

$$n \lambda = 2 d_{hkl} \sin\theta_{hkl}, \quad (3.1)$$

where n is an integer 1, 2, 3, ..., λ is the wavelength of incident X-ray, d_{hkl} is the distance between the atomic planes in a crystal (d-spacing) and θ_{hkl} is the diffraction angle (from the hkl planes).

2.4.2 XRD measurements

The XRD measurements were performed in the Bragg-Brentano geometry (geometry θ - 2θ) and at the Grazing Incidence Diffraction (GID). The experiment scheme was presented Fig. 2.6. In such a configuration, the X-ray incidents to the sample surface at a very low angle ω . The vector of X-ray diffraction changes its direction during the measurements making the angle $2\theta/2-\omega$ with the normal to the sample surface.

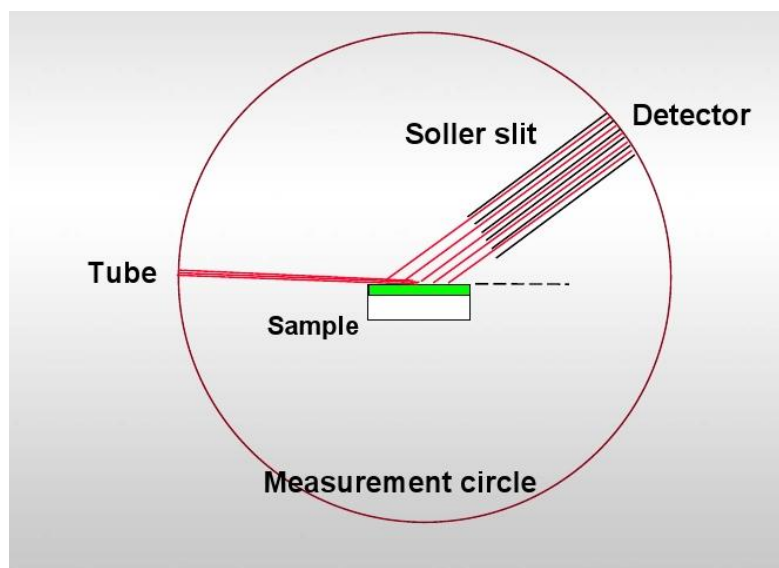


Figure 2.6. Grazing Incidence Diffraction (GID) [125].

2.5 X-ray reflectivity

2.5.1 The theoretical background

X-ray reflectivity (XRR) is a surface-sensitive non-destructive technique. In this method, the beam of x-rays incidents the surface of the sample and reflects in the specular direction. The idea is shown schematically in Fig. 2.7. The X-rays undergo total reflection when the incident angle on a flat surface of a material at a grazing angle is smaller than the critical angle for a total reflection θ_C . X-ray reflectivity is related to the values of refractive index and X-ray wavelength. X-ray reflectivity decreases rapidly (proportionally to θ^4) with increasing incident angle above the critical angle.

XRR spectra allows to determine layer thickness (by observation of reflectivity oscillations with θ), surface roughness is related to oscillation decay rate at higher angles, whereas critical angle θ_C gives the information about the layer density.

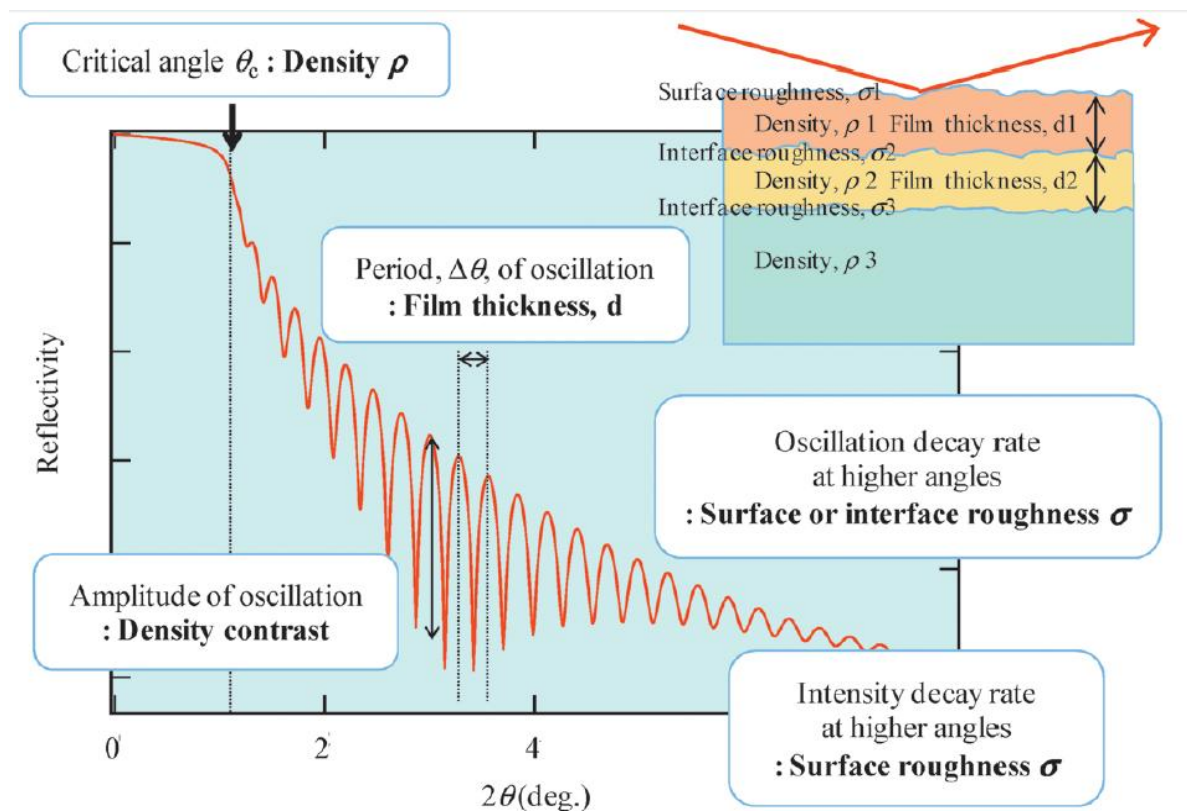


Figure 2.7. Scheme of XRR measurement for thin film and obtained spectra with possible determined structure properties [126].

The XRR method can be applied for:

- Studies of single crystals, polycrystalline and amorphous materials,
- Investigations of opaque material under visible light,
- Measurements of thin film thickness (up to ~500 nm),
- Determination of multilayer structures,
- Evaluation of surface and interface roughness (non-destructively).

2.5.2 XRR measurements

Experiments were performed at the Department of Electronics, Faculty of Computer Science, Electronics and Telecommunications, AGH University of Science and Technology, Kraków using X'Pert MPD Philips instrument with CuK_α filtered radiation. The X-ray source was operated at the voltage of 45 kV and current of 40 mA. Diffraction patterns were recorded within the range of diffraction angles 2θ ranged from 20° to 110° for Bragg-Brentano geometry and at the angles of incidence ω equal to 1, 3 and 6° in Grazing Incidence Diffraction (GID) configuration. More details of XRR measurements in GID configuration can be seen in Fig. 3.2 of Chapter 3.

WinGixa program of Philips was used for data analysis of the layered structure, the thickness and density of each layer as well as the roughness of the interfaces. As the beam in this configuration of experiment covers completely the sample, even small inhomogeneity in the film thickness is a source of the systematic error of the XRR analysis.

2.6 Rutherford Backscattering

One of the main outcomes of this research work is the sample characterization by means of Rutherford Backscattering technique. Thus in this section, besides of general information, we will give a detail description of the RBS apparatus employed for our research at the Institute of Nuclear Physics, Johann Wolfgang Goethe-Universität, Frankfurt am Main, Germany.

Rutherford backscattering spectroscopy (RBS) is an analytical technique used in materials science, which allows to determine the composition and structure of samples by measuring the backscattering of a beam of high energy ions scattered from this sample. RBS obtains the best results on the thin films and near surface structures.

2.6.1 History

Rutherford was the mastermind of an experiment done by Hans Geiger and Ernest Marsden in 1909 at the Physical Laboratories of the University of Manchester (the so-called gold-foil experiments or later Rutherford Backscattering experiments) [127]. Geiger and Marsden simply bombarded thin metal foils with a beam of monoenergetic and collimated alpha particles generated by radon. Their description of the basic required conditions of their experiment: “To obtain measurable effects, an intense pencil of alpha particles is required. It is further necessary that the path of the alpha particles should be in an evacuated chamber to avoid complications due to the absorption of scattering in air” [128]. While almost all particles reappeared behind the foil and were recorded by scintillation screen, they observed that a small amount of particles deflected at angles larger than 90 degrees, and a few percentage scattered back, towards the source (i.e. at angles close to 180 degrees). Ernest Rutherford could assume only one reasonable explanation of this observation: he concluded that each atom has a very small, positive – charged core that contain almost all mass of this atom (nucleus) and could repel the alpha particles. Soon this experiment was developed for exploration of overall spectrum and was called Rutherford Backscattering Spectroscopy (RBS). The first practical and nonnuclear application of RBS was applied in lunar expedition of Surveyor V in 1967 [129]. Since the success of Surveyor mission, RBS became known not only to scientific community but also to industrial researchers. The biggest advantages of Rutherford Backscattering lie in a high speed of the technique, its simplicity and a large amount of results. RBS becomes one of the most powerful tools to examine the composition of a sample as well as its depth distribution.

2.6.2 Physical background

During the bombardment of the surface of the solid state with the ions (e.g. He^+ , as in case of the measurements presented in this Thesis), the structure of a material changes. Depending on the energy of ion beam, three different cases can be observed, as illustrated in Fig. 2.8 [130]:

- backscattering,
- sputtering – when incident ions lead to elastic collisions of atoms in the material, what causes the sputtering of surface atoms. The transfer of energy takes place by the atoms in the sample,
- recoil sputtering – the incident beam ion directly transfers its energy to surface ions and lead to its ejection.

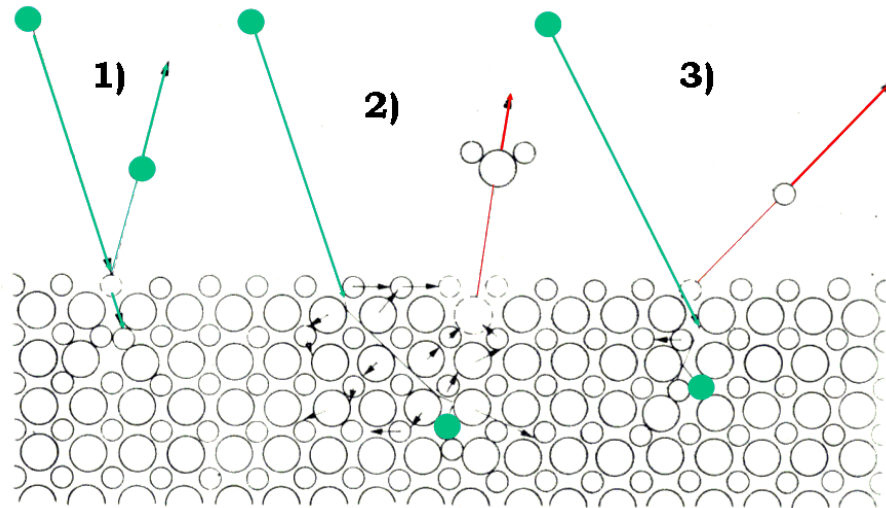


Figure 2.8. Different effects as a result of surface bombardment: 1) backscattering, 2) sputtering, 3) recoil sputtering [130].

In cases 2) and 3) the incident ions stay in the sample, when the material atoms are ejected. The release of material atoms is possible if the energies of incident ions are relatively low – in ranges of keV. Then, the dominant part of energy is transferred to investigated material. On the other hand, if the energy of incident particles is increased, they interact with material within short time. This time is not long enough for energy transfer and the structure of material cannot be changed. This case is presented as a case 1) in Fig. 2.8. Such experiments require the energies of MeV.

Binary Elastic Collisions and Kinetic Factor

Rutherford Backscattering is based on binary elastic collisions of two isolated particles described by the principles of conservation of energy and momentum. Let us consider the collision between two atoms, with masses m and M respectively. Before the collision the velocity of atom m is v_0 and its energy is E_0 , while the target atom of mass M is at rest. After the collision let v_1 and v_2 be the velocities and E_1 and E_2 the energies of projectile and target atoms, respectively. The scattering angle is θ and recoil angle is φ . It is schematically shown in Fig. 3.9. From the energy and momentum conservation, we have:

$$\frac{1}{2} m v_0^2 = \frac{1}{2} m v_1^2 + \frac{1}{2} M v_2^2, \quad (2.2)$$

$$m v_0 = m v_1 \cos \theta + M v_2 \cos \varphi, \quad (2.3)$$

$$0 = m v_1 \sin \theta - M v_2 \sin \varphi. \quad (2.4)$$

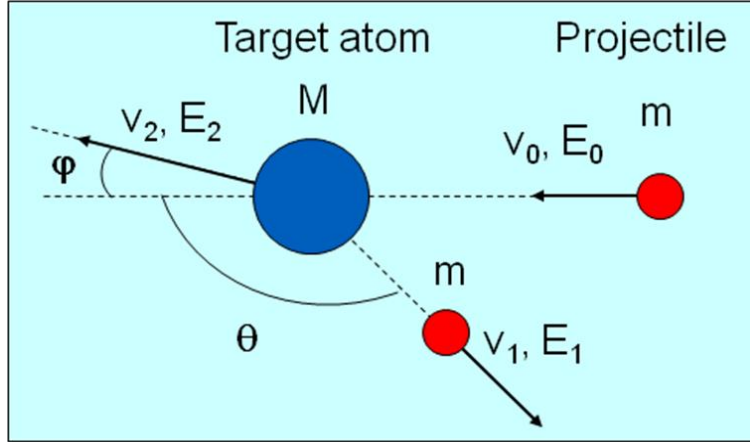


Figure 2.9. Schematic representation of an elastic collision between a projectile of mass m and a target mass M . v_0 and E_0 is the velocity and energy of projectile atom m before the collision. The target atom of mass M is at rest. v_1 , v_2 , E_1 and E_2 are respectively the velocity and energy of projectile and target atoms after the collision. θ and ϕ is the scattering angle and recoil angle, respectively.

Eliminating ϕ and v_2 we will get [131]:

$$\frac{v_1}{v_0} = \frac{[\pm(M^2 - m^2 \sin^2 \theta)^{1/2} + m_1 \cos \theta]}{m + M} \quad (2.5)$$

The kinetic factor K , defined as a ratio of projectile energy after the elastic collision to that before the collision, is:

$$K = \frac{E_1(\theta)}{E_0} = \left[\frac{(m/M) \cos \theta + \sqrt{1 - (m/M)^2 \sin^2 \theta}}{1 + (m/M)} \right]^2 \quad (2.6)$$

The kinetic factor K depends only on scattering angle θ and the ratio of the projectile to target masses m/M . For any combination of projectile and target mass the kinetic factor K always has the lowest value at 180° . When the projectile and the target mass are equal, K is zero for angles larger than 90° . It means that when projectile collides with a stationary atom equal to its own mass it cannot be scattered backward but only forward. When we know exactly the mass and energy of impinging projectile (m_1 and E_0) and if the energy of backscattered atom after the collision E_2 can be measured, and if the scattering angle θ is known, using the Equation 2.6, the mass of target atom of examined surface (m_2) is easily calculated.

In a standard backscattering spectroscopy, the detector is usually placed at 170° to avoid obstruction of impinging projectiles which would take place when placed at 180° .

The scattering cross section

The scattering cross section is a physical quantity defined as an area measured on the plane perpendicular to direction of projectile. Knowing the cross section, we can calculate the probability of scattering. Scattering cross section, from the other hand, is a quantity which describes frequency of atoms backscattered at a certain angle. Let us consider simple conceptual experiment in which a thin uniform target is bombarded by a narrow beam of fast particles. Then an ideal detector which counts each particle in the differential solid angle $d\Omega$ is placed at a scattering angle θ . If Q is the total number of particles that have hit the target and dQ is the number of particles recorded by the detector, then the differential scattering cross section $d\sigma/d\Omega$ can be defined:

$$\frac{d\sigma}{d\Omega} = \frac{1}{NtQ} \frac{dQ}{d\Omega}, \quad (2.7)$$

where N stands for volume density of atoms in the target and t is its thickness. Hence the product of N multiplied by t is the number of target atoms per unit area (i.e. the areal density). Simplified layout of a scattering experiment to demonstrate the concept of the differential scattering cross section is shown in Fig. 2.10.

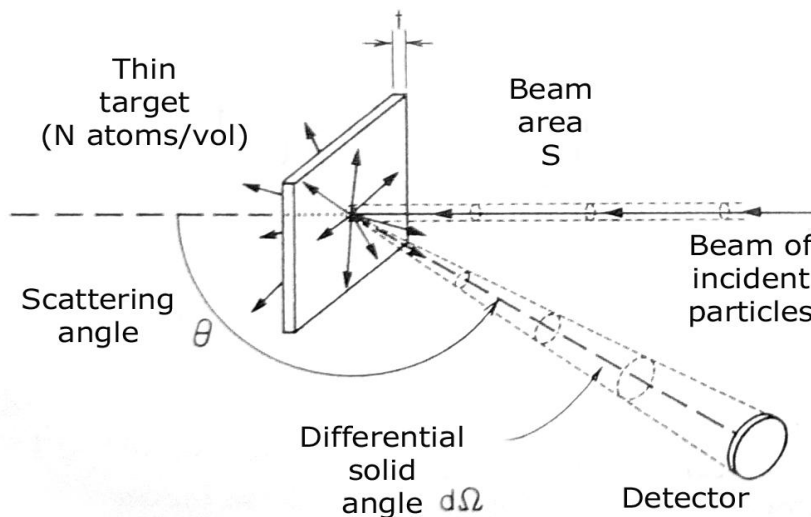


Figure 2.10. Simplified layout of a scattering experiment to demonstrate the concept of the differential scattering cross section [128].

To calculate the number of scattering events within a finite angle Ω the probability is described by integral scattering cross section Σ :

$$\Sigma = \int_{\Omega} (d\sigma / d\Omega) d\Omega. \quad (2.8)$$

This quantity in its geometrical interpretation is the same as in differential scattering cross section.

The average differential scattering cross section σ is defined as:

$$\sigma \equiv (1/\Omega) \int_{\Omega} (d\sigma / d\Omega) d\Omega. \quad (2.9)$$

For a very small detector angles Ω , we then have $\sigma \rightarrow d\sigma / d\Omega$ [131]. It is the average differential scattering cross section which value is usually used in backscattering spectrometry.

The Rutherford's formula for the differential scattering cross section is usually used (the so-called Rutherford's cross section):

$$\left(\frac{d\sigma}{d\Omega} \right)_c = \left[\frac{Z_1 Z_2 e^2}{4E_c \sin^2(\theta_c / 2)} \right]^2. \quad (2.10)$$

Here Z_1 and Z_2 are the atomic numbers of the projectile and target atom with mass respectively m_1 and m_2 respectively. E_c is the energy of the projectile immediately before scattering, e stands for electric charge. The index c indicates that the values are given in center-of-mass coordinates. For $m \ll M$ this formula is true also for values in the laboratory frame of reference. For the general case this equation in laboratory frame of references is given by:

$$\frac{d\sigma}{d\Omega} = \left(\frac{Z_1 Z_2 e^2}{4E} \right)^2 \frac{4}{\sin^4\theta} \frac{\left(\cos\theta + \sqrt{1 - (m/M)^2 \sin^2\theta} \right)^2}{\sqrt{1 - (m/M)^2 \sin^2\theta}}. \quad (3.11)$$

When we ignore the factor $\left(\frac{Z_1 Z_2 e^2}{4E} \right)^2$, the Rutherford differential scattering cross section

depends only on the ratio m/M and the scattering angle θ . For any combination of masses $d\sigma/d\Omega$ has its lowest value for $\theta = 180^\circ$. For angles near 180° scattering cross section does not change considerably with changing the scattering angle. This fact allows to obtain an accurate value of the calculated cross section near 180° with usage of the average acceptance angle of the particle detector.

The RBS measurement depends on gathering the information about the counts and energies of backscattered particles. These quantities depend not only on atom masses and cross sections, but also, in case of channeling experiments, on crystal structure of investigated material.

The formulas above describe the ideal situation for ions backscattered on the surface only once. In reality, the double or even triple backscattering processes are possible. This situation is presented in Fig. 2.11.

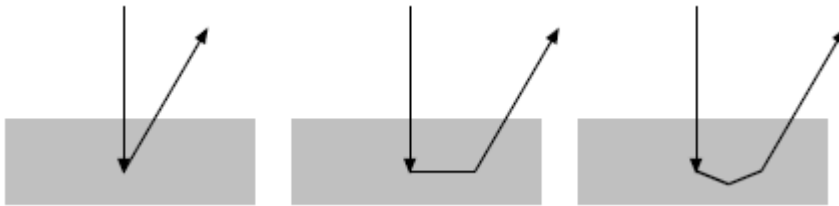


Figure 2.11. The illustration of ion trajectory after single, double and triple backscattering [132].

Many valuable information can be obtained the RBS method:

- the position and intensity of the peaks determine the chemical composition and concentration of elements in the sample,
- the width of peaks is correlated to layer thickness,
- the curves between peaks inform about the diffusion, interface creation and possible existence of another phase.

Rutherford Backscattering Spectroscopy is very efficient for heavy elements. The sensitivity decreases with decrease of element masses.

2.6.3 Instrumentation and Experimental Techniques

The tested target is bombarded by a beam of monoenergetic high-energy particles, mainly helium ions. On the target itself we observe backscattering of particles and later some of these deflected particles are analysed, counted and changed into information which is stored by a computer system. A schematic diagram of the RBS spectrometry is shown in Figure 2.12. The most widely accelerator used in RBS experiments is Van de Graaff accelerator. A photo of VDG accelerator is shown in Fig. 2.13. We used the He^+ ion beam with energy 1.6 – 2.0 MeV.

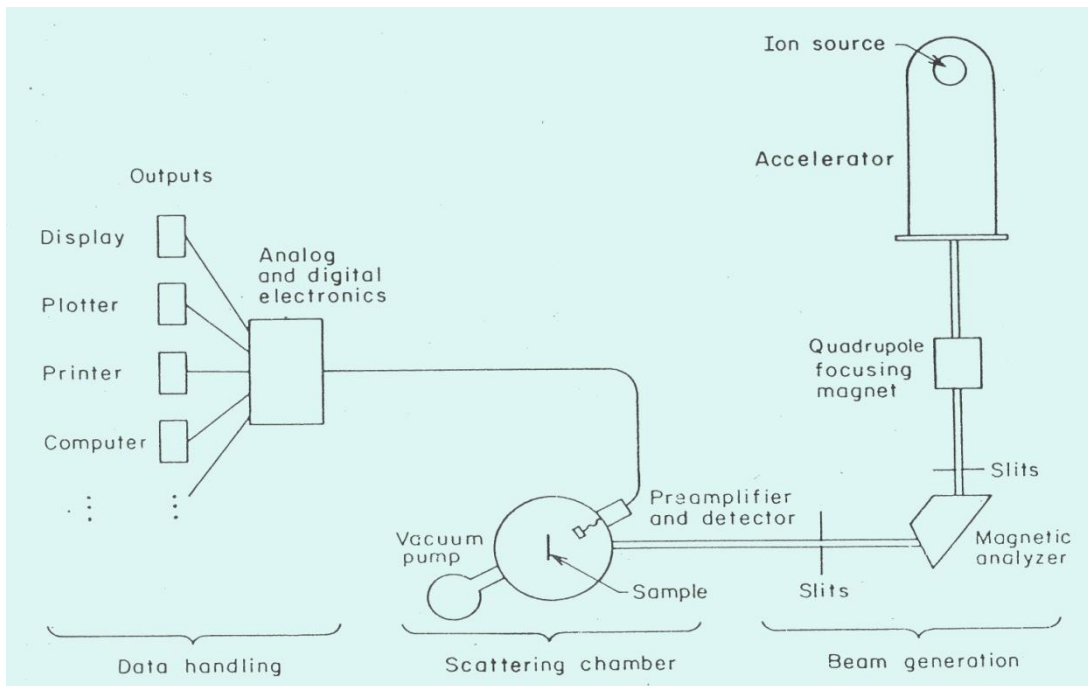


Figure 2.12. Scheme of an ion backscattering apparatus [131].

Figure 2.13. Van de Graaf Accelerator (He^+ 1.7-2.0 MeV) at the Inst. of Nuclear Physics, Johann Wolfgang Goethe-Universität, Frankfurt am Main, Germany.



The beam line is simply a beam of ions traveling from the accelerator to the experimental chamber. The ion beam produced by an ion source has to be first of all collimated. The collimators therefore are the main component of beam line. The $^4\text{He}^+$ ion beam spot before collimation is shown in Fig. 2.14.

The main components of backscattering spectrometry (the accelerator, the beam line and most important the experimental chamber) have to remain under the control of vacuum

system (turbo-molecular and diffusion pumps). The required vacuum for best accelerator – beam line collaboration range from 10^{-5} to 10^{-7} Torr. The pumping system is shown in Fig. 2.15.

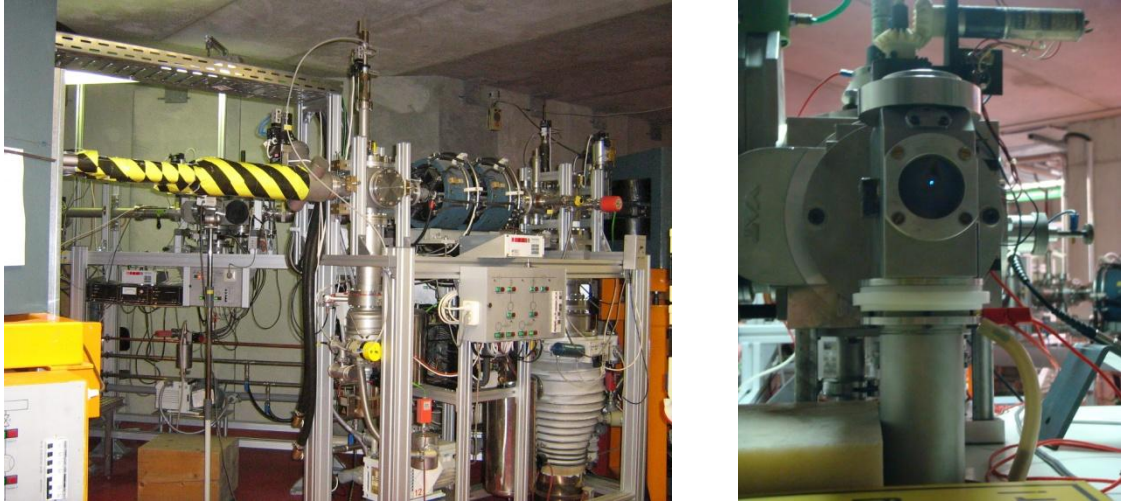


Figure 2.14. The beam line and the ${}^4\text{He}^+$ ion beam spot (blue spot) before collimation (i.e. a larger size to be seen).

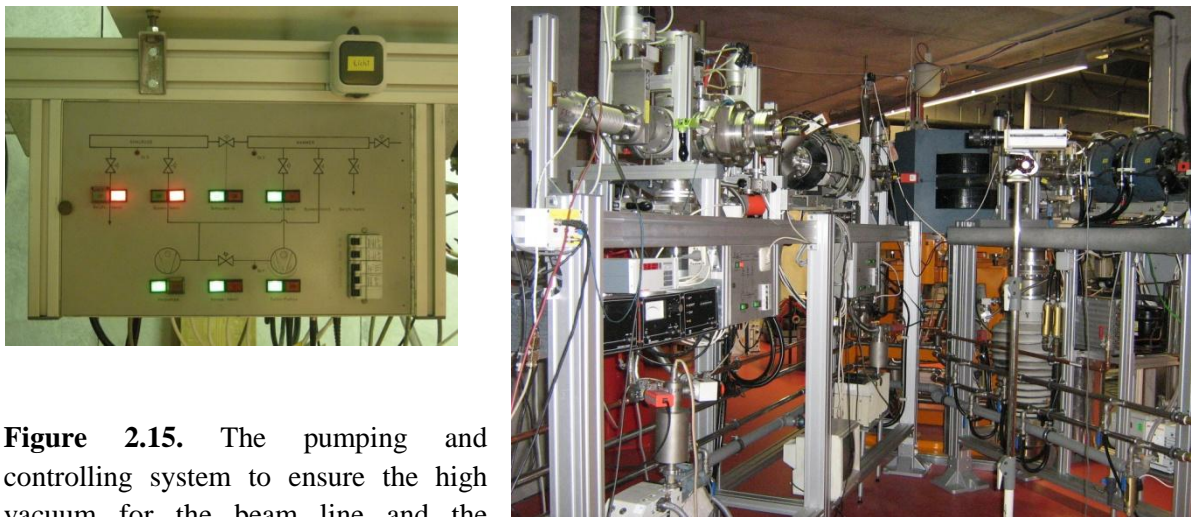


Figure 2.15. The pumping and controlling system to ensure the high vacuum for the beam line and the experimental chamber.

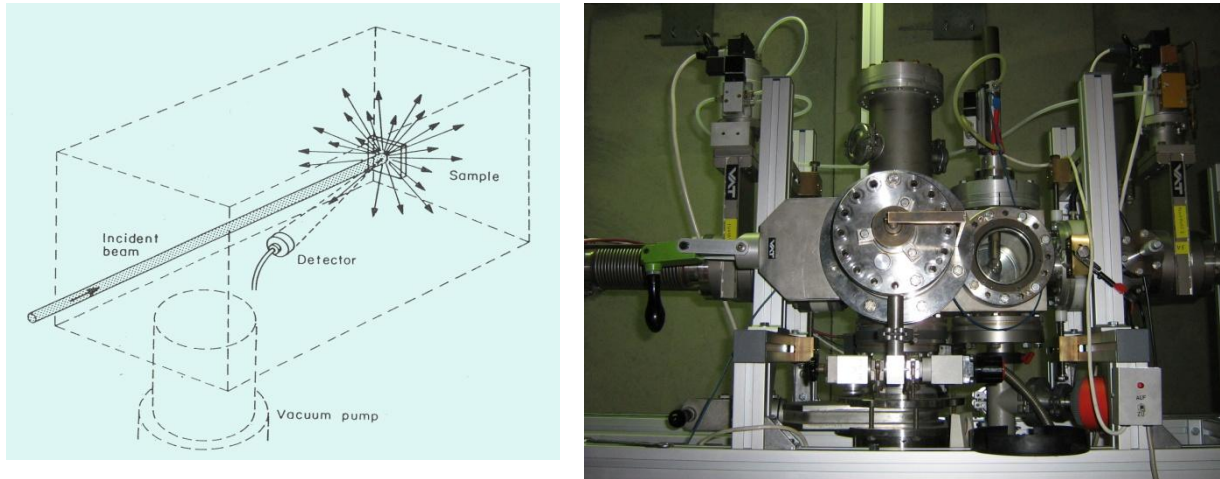


Figure 2.16. Experimental chamber for RBS, a simplified view (left) [131] and a photo (right).

Figure 2.17. Sample holder for RBS measurements.



The experimental chamber consists of a detector and a sample analyzer. In most RBS apparatus, the scattering angle is fixed (with respect to the angle between the detector and the incoming beam direction, while the incidence angles can be changed in the range of e.g. 0° - 50° (by turning the sample holder). In Fig. 2.16 a simplified view and photo of an experimental chamber for RBS and of a sample holder was shown in Fig. 2.17. For our experiments the scattering angle θ is 171° , and the incident angle α is in the range 0° - 45° .

The Si detector was used. All signals and counts from detector have to be transferred to analyzing system. All information collected and amplified by a detecting system finally get to multichannel analyzer, which is simply a special computer to data storage and interpretation. The accelerator, the ion beam and RBS measurements were controlled automatically through the controlling system shown in Fig. 2.18.

Figure 2.18. Ion Beam and measuring control system for RBS measurements.



2.6.4 Data evaluation and computer simulations

SIMNRA and RUMP simulation programs

For evaluation and analysis the RBS data, the SIMNRA (simulation program for the Analysis of NRA (nuclear reactions), RBS and ERDA (elastic recoil detection analysis)) and RUMP simulation (**RBS Universal Master Package**) are widely used.

SIMNRA is one of the best and most commonly used simulation programs. It was developed in Max-Planck-Institute for Plasmaphysics in Garching, Germany [132]. SIMNRA is a software which works in Microsoft Windows system. SIMNRA provides simulation of backscattering spectra for ion beam analysis and is mainly intended for nuclear reactions, elastic recoil detection analysis and non-Rutherford backscattering, but can also be used for RBS. It can calculate for any combination of impinging ions and target atoms at any geometry of experimental equipments. The data base of the program contains more than three hundred cross sections of different nuclear reactions for many incident particles like: protons, deuterons, ^3He , ^4He and Li-ions. SIMNRA has a fully graphical interface and varies data analysis tools that provide calculation of scattering kinematics, positions of elements and peak integrals. Many different stopping powers and energy loss stragglings is provided.

RUMP (**RBS Universal Master Package** (or **Rutherford Universal Manipulation Program**)) is the second most commonly used simulation program for RBS. It is developed at Cornell University. The first version of RUMP was written in FORTRAN language but later was based on ANSI C. Original computer code was created by L.R. Doolittle, M.O.

Thompson and R.C. Cochran, all members of Dr. J.W. Mayer's research group at Cornell University [133]. This program lost its leadership among simulation programs just recently to SIMNRA. The most important fact is, that this program was specifically designed for the simulations and analysis of Rutherford Backscattering Spectrometry data. RUMP is sold with additional back up simulation program called GENPLOT. Stopping powers in RUMP were ensured for helium, hydrogen and deuterium for energies ranging up to 3 MeV.

SIMNRA analysis

Before performing the simulation, the experiment setting, such as incident ions, their energy, geometry of experiment, calibration (energy per channel), as well as expected sample composition need to be initiated. Then, the simulated spectra is generated and could be compared to experimental data. The main point is to obtain the spectra, which agrees with the experimental data with the best accuracy, but on the other hand it should correspond to the real situation.

In SIMNRA, the “virtual” equivalent of the real sample should be created. This virtual sample should be theoretically divided into several sub-layers, called “calculation layers”. This situation is illustrated in Fig. 2.19.

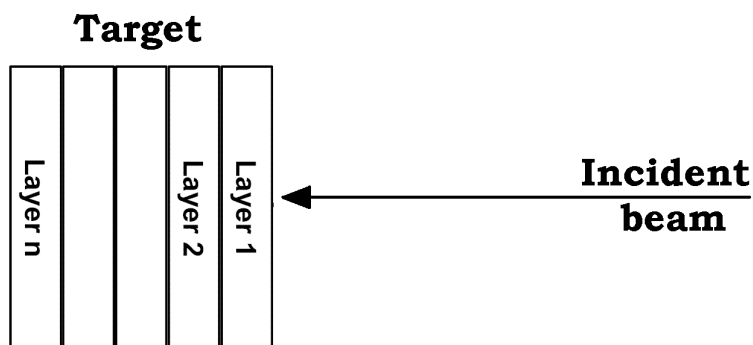


Figure 2.19. The “virtual” sample divided on n – calculation layers.

Increasing the number of calculation layers leads to a smoother and more accurate fit, but this number should not be significantly different than that in the real sample. In each calculation layer, the possible element concentrations in [%] and its thickness (in units of surface density, [10^{15} at/cm²]) should be proposed.

The comparison of simulated spectra to experimental data should take into account two aspects: the reliability and the physical sense of obtained fits. It is always possible, that the obtained simulated spectra will not fit well to experimental data due to insufficient

characterisation of all processes which are possible during RBS measurements. This results also in a potential lack in computational algorithms. On the other hand, the obtained simulated spectra may present a good agreement to the data, but may not have any physical sense. Thus it is very important to find a compromise between these two facts during simulating the RBS data.

From the obtained simulated spectra, the depth profile can be constructed, i.e. the element concentration as a function of the sample thickness. The obtained thicknesses of calculation layers in [10^{15} at/cm²] need to be converted into the real layer thickness in [nm].

In the first step, the atomic density, ρ_{atomic} , should be calculated using the formula:

$$\rho_{atomic} [at/cm^3] = \frac{\rho_{mass} [g/cm^3] \cdot N_A [at/mol] \cdot Z}{M_{mol} [g/mol]}, \quad (2.12)$$

where ρ_{mass} is mass density, M_{mol} is the molar mass and Z is the number of atoms which form the compound. The value of atomic density is important, because it can be different if the layer reveals significant diffusion or several compounds mixing. The atomic density is set in the unit [10^{22} at./cm³]. Despite the fact, that Formula 2.12 does not take into consideration the compound crystallographic structure, the density value is often good enough for the RBS data analysis.

The numerical calculations in SIMNRA are based on the surface areal thickness t_{areal} . The dependence between the areal thickness and the atomic density is presented by formula:

$$t_{areal} [at/cm^2] = \rho_{atomic} [at/cm^3] \cdot d [cm], \quad (2.13)$$

where d is the sample thickness set in [10^{-7} cm] and the areal thickness is in [10^{15} at/cm²].

The scaling factor will be then formulated:

$$A_0 [nm \cdot cm^2/at] = \frac{d [nm]}{t_{areal} [at/cm^2]}, \quad (2.14)$$

This is a proportional coefficient for the areal density of $1 \cdot 10^{15}$ at/cm² for a layer thickness of 1 nm (10^{-7} cm). Since each material is characterized by a different atomic density, the value of scaling factor varies for different materials. If the layer consists of many compounds, the arithmetical mean of A_0 is required to be calculated accordingly to the contribution (in percentage) of each compound.

The areal layer thickness obtained from SIMNRA d_{sim} (in the unit of [10^{15} at./cm²]) can be converted into the real thickness d_{real} (in [nm]) by using the equation:

$$d_{real}[nm] = d_{sim}[at/cm^2] \cdot A_0[nm \cdot cm^2/at]. \quad (2.15)$$

The calculations can be done also in the opposite direction, i.e. if the real layer thickness is known, the surface areal density can be determined and used as an input parameter for SIMNRA computer simulation.

In SIMNRA one can take account the electronic stopping power data by Ziegler and Biersack, Chu+Yang's theory for electronic energy-loss straggling and Andersen's screening function to Rutherford cross-section. The contribution from a double and/or multiple scattering into the RBS spectra can be also taken into account using the calculating facilities of SIMNRA.

2.7 Secondary Ion Mass Spectrometry

Secondary Ion Mass Spectrometry (SIMS) is a damaging technique for materials science. This method is basically considered as a qualitative technique, however, quantitative estimation can be also possible. When a solid sample is sputtered by primary ions of few keV energy, a fraction of the particles emitted from the target is ionized. SIMS consists of analyzing these secondary ions with a mass spectrometer [134]. In this method, a focused primary ion beam (O_2^+ , Cs^+ , Ga^+ , Ar^+ or cluster ions: SF_5^+ , Au_3^+ , Bi_3^+ , Bi_2^{3+}) sputters the surface and eject the sample atoms (secondary ions). During this process, a crater is created. The mass/charge ratios of these secondary ions are measured with a mass spectrometer to determine the elemental, isotopic or molecular composition. The main principle of SIMS technique is presented in Fig. 2.20. The SIMS technique provides a unique combination of very high sensitivity for all elements, high lateral resolution imaging and a very low background. SIMS is one of the most sensitive surface analysis technique: the elemental detection limits range from parts per million to parts per billion (ppb) level for many elements.

The typical SIMS spectrometer is presented in Fig. 2.21. SIMS equipment works under UHV conditions. Vacuum is required to prevent collisions of secondary ions with background gases on their way to the detector.

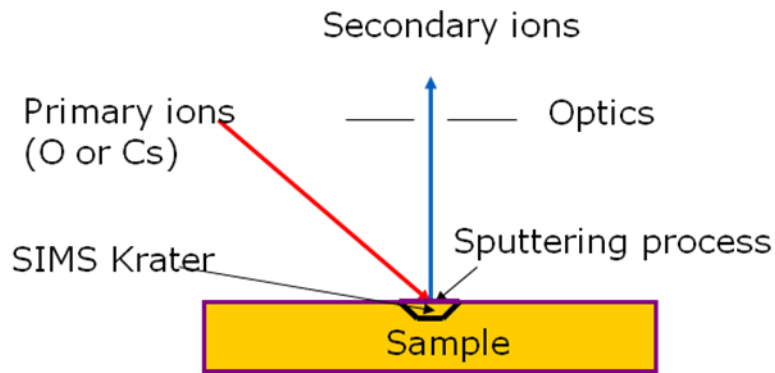


Figure 2.20. Basic principle of SIMS technique.

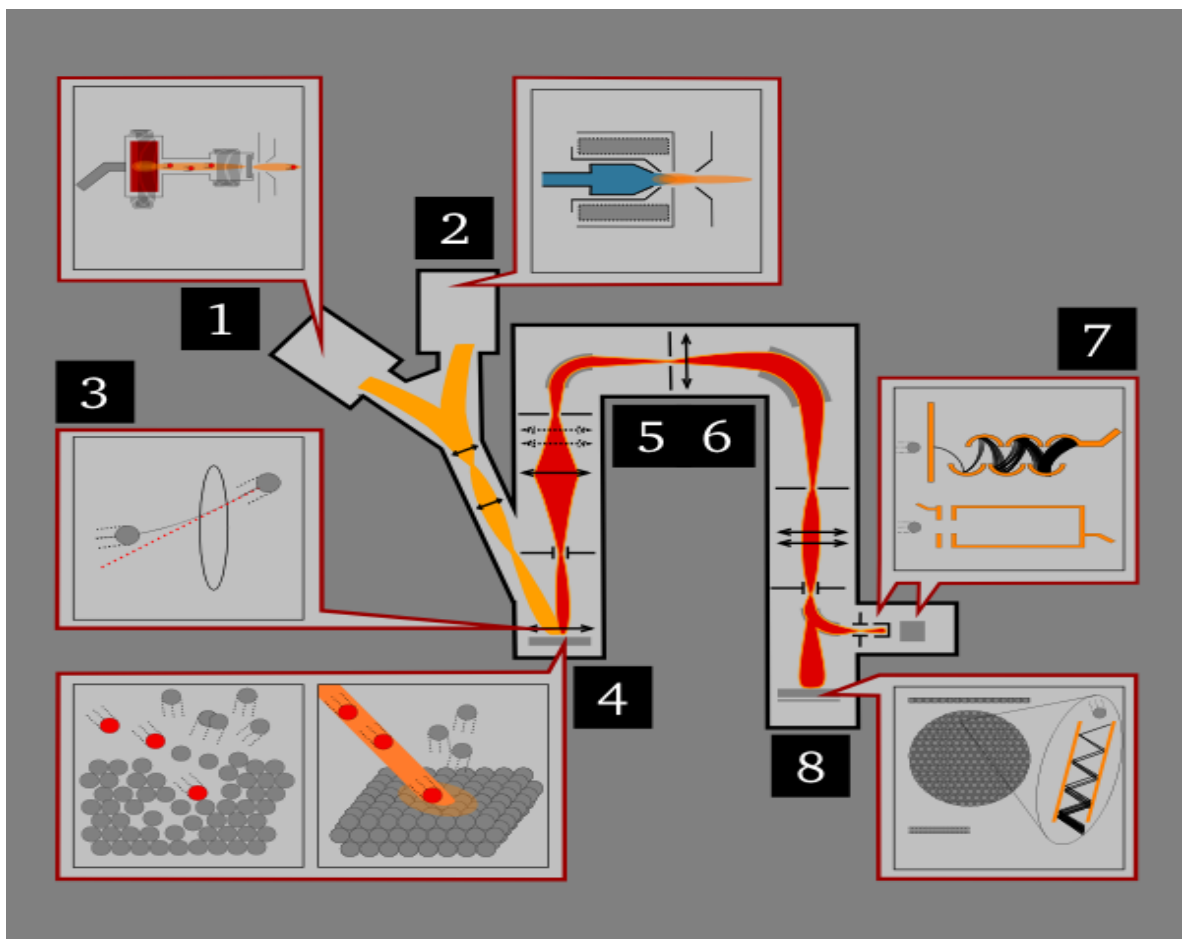


Figure 2.21. Scheme of SIMS equipment with steps of SIMS measurement [134].

The spectrometer consists of primary ion gun, generating the primary ion beam (picture 1 and 2 in Fig. 2.21). Depending on the kind of the primary ion, three different types of ion guns are used.

- In the first type, ions of gaseous elements (noble gases: Ar^+ , Xe^+ , oxygen: O^+ , O_2^+) or ionized molecules as SF_5^+ , C_{60}^+ are generated by electron ionization or with duoplasmatrons. This gun generates high current ion beams and is easy to operate. However, the beam is not perfectly focused.
- The second type of a gun is a surface ionization source. This gun is used for generation the Cs^+ primary ions. The cesium atoms are ionized during evaporation through a porous tungsten plug. As in the case of previous type, the gun can generate fine focus or high current, what is related to its design.
- The liquid metal ion gun (LMIG) is the third type of ion guns. It works with metals or metallic alloys in a liquid state at room temperatures. Ions are emitted by a tungsten tip covered with liquid metal when an intense electric field is applied. Due to its ability for focusing a beam (less than 50 nm) and generation of short pulsed ion beams, it is commonly used in recent SIMS equipment.

The primary ion beam is accelerated and focused on the sample by the primary ion column. Some devices allow to separate the primary ion species, e.g. by Wien filter. When the primary ion beam achieves the target sample (picture 3), the process of sputtering and ejection starts (picture 4). These secondary ions are then collected by ion lenses (picture 5). Then the mass analysers filter the secondary ions according to atomic mass (picture 6). The analyzers can be grouped as a sector field mass, quadrupole and time-to-flight devices. A sector field mass spectrometer separates the secondary ions by their mass-to-charge ratio using a combination of a magnetic and electrostatic analysers. Resonant electric field allows only one selected mass to pass through, and it is a principle of quadrupole mass analyser. The time-to-flight analyzer is the only analyzer type able to detect all generated secondary ions simultaneously. It is based on the feature, that ions with the same kinetic energy have different velocity (and therefore time of drift) due to different masses. Recently it is a standard analyzer for static SIMS equipment. After separation of the secondary ions, they are projected onto an ion detection unit: electron multiplier (picture 7 top), Faraday cup (picture 7, bottom) or CCD screen (picture 8).

The obtained spectrum consists of secondary ion counts in function of primary ion deposition time. To transform the deposition time into depth scale, first, the crater depth has to be measured. Dividing this value by total experiment time gives the information about the “velocity” of ejection process, and, when multiplied by specific time of experiment, the specific depth can be obtained.

The SIMS measurements have been performed at Institute of Materials Science, Technische Universität Darmstadt using Cs⁺ primary ions recording positive secondary ions by a CAMECA ims 5f equipment with a base pressure of 3 · 10⁻¹⁰ mbar.

2.8 Nuclear Reaction Analysis – N-15 method

RBS technique, due to the Z^2 dependence of the cross-section, has a very low sensitivity for light elements. Thus investigation of materials consisted of light elements in particular hydrogen often requires other nuclear based methods, such as nuclear reaction analysis (NRA) using Nitrogen beam (N-15) or elastic recoil detection analysis (ERDA).

2.8.1 Physical background

A commonly used nuclear reaction to profile hydrogen is:



with a resonance at e.g. 6.385 MeV. This reaction is denoted as $^1\text{H}(^{15}\text{N}, \alpha, \gamma)^{12}\text{C}$.

The N-15 isotope beam bombards the hydrogen containing sample. If the energy of a beam is equal or higher than E_{res} , the oxygen atom is created as a result of the fusion of N-15 atoms with hydrogen. This oxygen atom throws out an α particle, what results in its transformation into excited carbon atom. When carbon cools down, turning into its ground state, the γ quant with energy of 4.965 MeV is emitted. Detected by a scintillation counter, the measured gamma yield gives the information about hydrogen concentration in the sample, since the proportionality between these two quantities occurs. The H concentration profile is then obtained by scanning the ^{15}N incident beam energy.

The N-15 method based on a strong, isolated resonance in the cross section of nuclear reaction $^1\text{H}(^{15}\text{N}, \alpha, \gamma)^{12}\text{C}$ for hydrogen detection is illustrated in Fig. 2.22 [135].

The reaction takes place when the energy of N-15 isotopes is no lower than 6.41 MeV. At this energy, the resonance occurs. The projectiles with such energy equal to the resonance energy can only perform nuclear reactions at the sample surface (i.e. the N-15 beam can react only with hydrogen in the surface). By increasing the acceleration energy of the incoming ion beam one shifts the resonance reaction in a certain depth: the reactions take place not until the incoming ions are slowed down to E_{Res} , i.e. the nitrogen ions then react with hydrogen in the deeper parts of a sample. If composition and density of the sample are known one can generate via energy loss a depth profile. Principle of hydrogen profiling with the ^{15}N method is illustrated in Fig. 2.23.

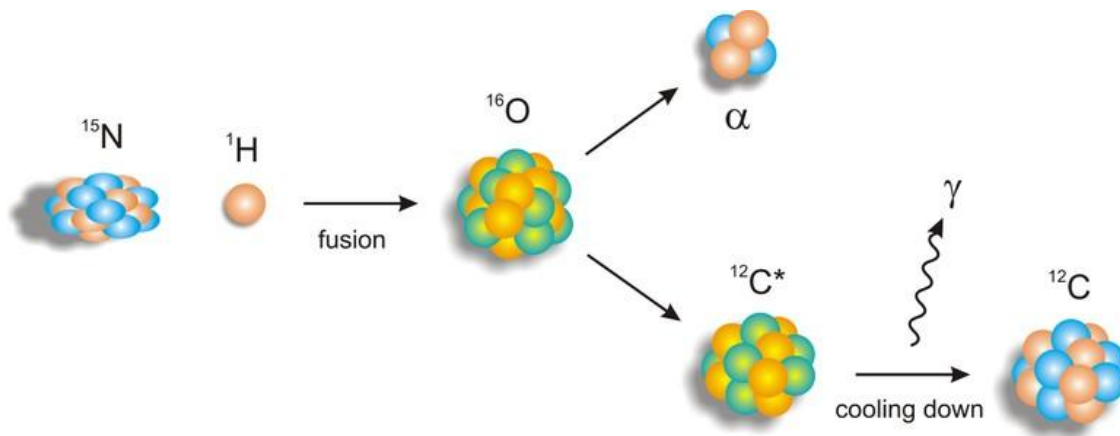


Figure 2.22. Scheme of nuclear reaction in N-15 method [135].



Figure 2.23. Principle of hydrogen profiling with the ^{15}N method [135].

In our research we used N-15 - NRA method at the resonance energy of 6.417 MeV was used to obtain the results. The measurements have been performed at the Dynamitron Tandem Labor, Ruhr-Universität Bochum, Germany.

2.8.2 Data evaluation and computer simulation

For data evaluation of N-15 measurements the computer code SRIM (Stopping and Range of Ions in Matter) was used [136]. SRIM has an easy-to-use interface and includes built-in default parameters for all ions and materials. It uses a Monte Carlo simulation method

for obtaining the results, such as: distribution of the ions in the material with the information about penetration depth, straggle, atom cascades, vacancies concentrations and photon production in the target material. SRIM allows for calculation of the energy-loss rate by the ion in the target, defined as dE/dx – the energy loss per unit distance in the material. Thus SRIM calculations allow to re-scale the energy of N-15 beam into the depth profile in the sample.

2.9 Optical reflectivity measurements

For some Ti-TiO₂ thin films the film characterization was performed by means of optical spectroscopy, at the Department of Electronics, Faculty of Computer Science, Electronics and Telecommunications, AGH University of Science and Technology, Kraków.

Optical reflectance $R(\lambda)$ and transmittance $T(\lambda)$ spectra over the wavelength range λ from 220 nm to 2200 nm were detected by means of UV-VIS-NIR Perkin-Elmer double beam Lambda 19 spectrophotometer equipped with an integrating sphere. In all cases the diffuse component was negligible (<1%). In order to estimate the optical constants (refractive index n and extinction coefficient k) of the components of a layered structure, single layers of Ti and TiO₂ with nominal 50 nm thickness were deposited onto transparent amorphous silica substrates. Moreover, the optical measurements of uncovered Si(111) wafers were performed with the aim to establish n and k of the substrate. Modeling of the optical spectra was carried out with the help of FilmWizard commercial software.

Chapter 3

Investigations of layer geometry and properties of as-deposited Ti-TiO₂ thin films

Numerous Ti-TiO₂ thin films with single-, bi- and tri-layer structure deposited on different substrates (such as Si(111) substrate, C-foil, silica SiO₂) by means of *dc* pulsed magnetron sputtering technique have been prepared and investigated. We first focused on characterization of the as-sputtered (as-deposited) films, such as the chemical composition, and the film thickness and the interface properties. Indeed the film thickness is a very important parameter in both photocatalysis and hydrogen storage. For instance the photoactivity and photocatalytic activity of TiO₂ films deposited on soda-lime glass substrates by Atomic Layer Deposition have been found to reach their maximum at a film thickness of 15 nm [137]. Application of hydrogen would affect microstructure and properties of thin-film and multilayer structures. On the other hand, the atom mixing, diffusion across the interfaces can also influence the hydrogen uptake. Thus selected bi- and three-layered Ti-TiO₂ films subjected for hydrogen charging at atmospheric pressure and/or at high pressures were then investigated focusing on the film stability, the hydrogen uptake and hydrogen storage under different conditions.

The work described in this chapter concerns in the characterization of the layer structure and properties of Ti-TiO₂ thin films after deposition (as-deposited state). The effect of hydrogen on the films will be presented in the next chapter (Chapter 4).

We have prepared the following films:

- Single-, bi- and tri-layer films grown on Si(111) substrate: Ti/Si, Ti/TiO₂/Si, Ti/TiO₂/Ti/Si,
- Single-, bi- and tri-layer films grown on C-foil: Ti/C, Ti/TiO₂/C, Ti/TiO₂/Ti/C,
- Single layer of Ti on SiO₂.

The nominal thickness of each layer (*d*) was in the range of 10 nm to 250 nm selected and served accordingly to different plans of investigations. For instance the thin films (*d* = 10 – 50 nm) were the subject for investigation of the layer quality. The thicker single-layer films (*d* = 50 – 250 nm) or the tri-layer films with similar (total) thickness were for hydrogenation. One series of tri-layer films was subjected for an additional Pd covering. Namely, after titanium and titanium dioxide layer deposition, they were partially (about one third of the film surface) covered by 20 nm-thick palladium layer by physical vapour deposition.

The oxygen signal in the films deposited on C-foils appeared as a well-separated peak in the Rutherford back-scattering spectra, while it exists as a small peak on a high background from Si signal from the substrates. The atomic mass of Oxygen is 16 so that the O-signal would lie on the right-hand side of the C-edge where the background is almost zero. The atomic mass of Si is 28. Thus the O-signal would lie on the left-hand side of the Si-edge, i.e. on the high background signal from Si substrate. Thus the oxygen content can be analysed in more details in those films deposited on C-foils and would give additional supporting information for the films deposited on Si substrates. The films deposited onto amorphous silica transparent substrates are used for the measurements of the optical transmittance.

The film chemical composition, depth profile, layer thickness and structure were determined by combined analysis of XRD, XRR, RBS and optical reflectivity spectra. The simulated areal density value from SIMNRA analysis of the RBS data was converted into the layer thickness in [nm], so that it can be compared with the (thickness) value estimated from other methods. Details of our RBS analysis in particular the conversion of the RBS layer thickness into [nm] was described in Chapter 2 in which we have used the film density determined from XRR experiments. The film geometry, estimated layer-thickness and film-notations of different films used in our experiments (presented in Chapter 3 and 4) were given in Table 3.1.

3.1 The thin Ti-TiO₂ films deposited on Si(111) substrates

The Ti/Si(111), TiO₂/Ti/Si(111) and Ti/TiO₂/Ti/Si(111) with a nominal thickness of 50 nm are presented in this section. For a comparison, the results for a single layer of Ti deposited onto amorphous silica SiO₂, i.e. Ti/SiO₂ with a similar thickness are also shown.

Details of XRR measurements in GID configuration (GIXR) are shown in Fig. 3.1. XRR measurements were carried out in a parallel beam of 0.1 mm width. XRR θ - 2θ scans were recorded within the angular range of 0°-2°. The critical angle Θ_c of the order of 0.27°-0.3° has been established experimentally, depending on the degree of oxidation.

Notation	Film geometry	Layer thickness d (nm)			
		Ti(1)	TiO ₂ (2)	Ti(3)	Pd
S1	Ti/Si(111)	47			
S2	Ti/Si(111) **	67			
S3	Ti/Si(111) **	240			
D1	TiO ₂ /Ti/Si(111)	46	46		
D2	TiO ₂ /Ti/Si(111)	100	110		
D3+Pd (partial)	Pd/ TiO ₂ /Ti/Si(111) *	79	97		20
D4	TiO ₂ /Ti/Si(111)	100	160		
D4-C	TiO ₂ /Ti/C-foil	100	160		
D5	TiO ₂ /Ti/Si(111) **	15	60		
T1	Ti/TiO ₂ /Ti/Si(111)	49	51	40	
T2	Ti/TiO ₂ /Ti/Si(111) *	100	110	50	
T3+Pd (partial)	Pd/Ti/TiO ₂ /Ti/Si(111) *	80	96	40	19
T4	Ti/TiO ₂ /Ti/Si(111)	100	150	120	
T4-C	Ti/TiO ₂ /Ti/C-foil	100	150	120	
T5	Ti/TiO ₂ /Ti/Si(111) **	15	60	20	

Table 3.1. The film geometry and the layer-thickness (d (nm)) for different layers estimated by combined analysis (see text). The notation for single, bi- and tri-layered films deposited on Si(111) is respectively S (single), D (double) and T (triple). The added letter ‘-C’ was for those deposited on Carbon foils, while those with “+Pd” noted the films covered partially by palladium. The number in parenthesis denote the layer sequence: Ti(1) is the first Ti layer deposited directly onto the Si(111) substrate and on C-foil), TiO₂(2) is the second TiO₂ layer deposited onto the Ti(1) layer and Ti(3) is the third Ti layer deposited onto the TiO₂(2) layer. The additional Pd layer was deposited onto about a half of the surface of the two films (Pd (partial)) used for investigation of hydrogenation. Films used for the hydrogenation at 1 bar and at high pressures were marked respectively by (*) and (**).

small inhomogeneity in the film thickness is a source of the systematic error of the XRR analysis.

Fig. 3.2 demonstrates the cross-section and surface SEM images of a triple layer structure Ti/TiO₂/Ti/Si(111). Different modes of growth for bottom layer of Ti, intermediate layer of TiO₂ and the top layer of Ti can be distinguished. The bottom Ti nucleates and grows as a compact layer on the well-defined (111) plane of Si wafer. The intermediate TiO₂ layer exhibits columnar structure while the uppermost layer of Ti is deposited on top of caps of columns. In this case a possible Ti diffusion along the channels formed between columns should be taken into account. Thus, it is difficult to determine the exact value of thickness of each layer from the SEM images. As the boundaries between sublayers can be assigned somewhat arbitrary, their thicknesses as determined from RBS are marked in Fig. 3.2.

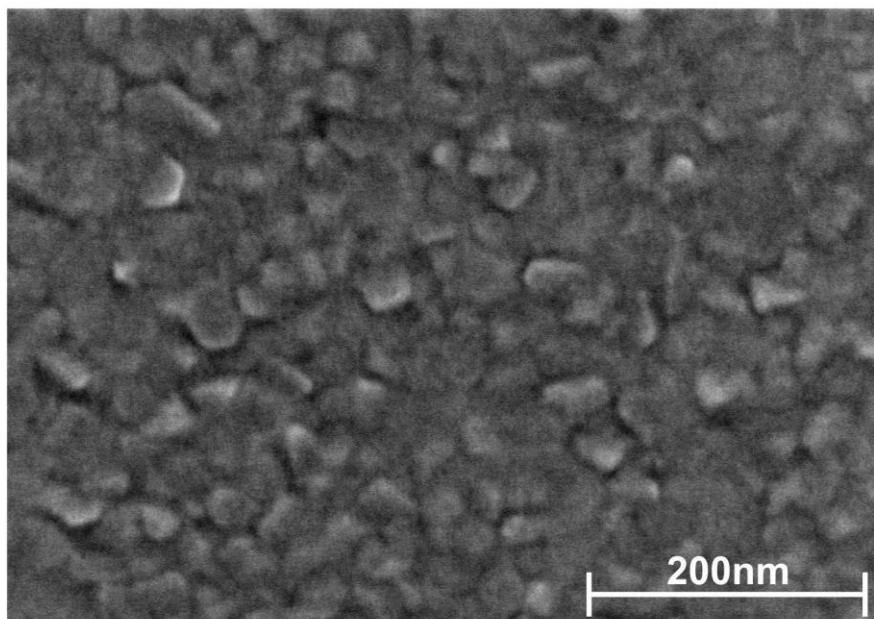
XRD patterns of the deposited layered structures: Ti/Si(111), TiO₂/Ti/Si(111) and Ti/TiO₂/Ti/Si(111) are shown in Fig. 3.3 (top). For comparison, the XRD pattern for a single layer of Ti deposited onto amorphous silica SiO₂ is also given in the same figure. Background rise at small angles in this case is due to the amorphous nature of the substrate used. In spite of a sufficiently long counting time (20 s per step), the intensity of diffraction peaks is relatively low (peak-to-background intensity in most cases is smaller than 1) while their width of about 1°-2° is substantial enough. Moreover, the Ti films, crystallizing in the hexagonal structure [138], exhibit a strong preferred orientation with (00.1) plane parallel to the substrate, as indicated by an intense diffraction from (10.3) planes.

In GID configuration, the vector of X-ray diffraction changes its direction during the measurements making the angle $(2\theta/2) - \omega$ with the normal to the sample surface (dashed line) as shown in Fig. 4.1. The Bragg condition is fulfilled for the crystallographic planes inclined at $(2\theta_{hkl}/2) - \omega$ and the distances d_{hkl} obeying the relationship (2.1).

In powder samples, there always exist the crystallites of the orientation in agreement with the above equation. In this configuration, the intensities of the diffraction peaks will be very close to the values obtained in the measurements performed in the symmetrical Bragg-Brentano geometry for the same powder sample.

Here, in this work, we can see that the intensity of all diffraction lines is very small except for the peak corresponding to (10.3) crystallographic plane (Fig. 3.3). Normal to this plane forms an angle of 31.4° with the *c*-axis, while in the geometry of measurement the diffraction vector for this plane is inclined at the angle of 32.2° with respect to the normal to the sample surface. Taking into account that the diffraction peaks are rather broad (>1°) low difference between these angles favours the increase in the intensity of (10.3) peak intensity. As for other planes such a coincidence does not occur, it is reasonable to assume that the orientation of Ti crystallites is such that the *c*-axis of its hexagonal cell is perpendicular to the substrate.

a)



b)

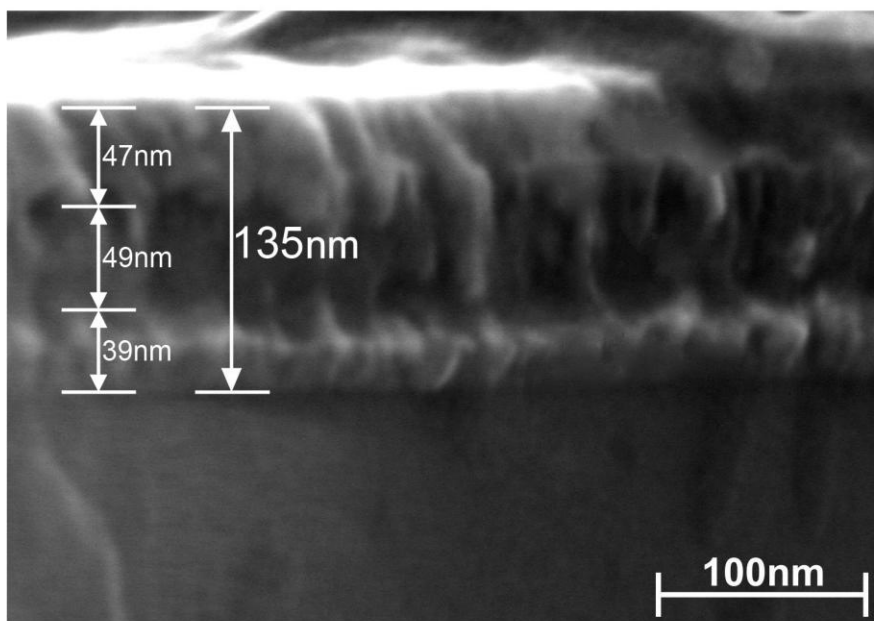


Figure 3.2. SEM images of surface (a) and cross-section (b) of Ti/TiO₂/Ti/Si(111) film deposited by magnetron sputtering. The sublayer-thicknesses determined from RBS and GIXR are indicated.

The observed preferential orientation of Ti crystallites is not forced by the substrate Si(111) because it is preserved even in the uppermost Ti layer of a triple structure of Ti/TiO₂/Ti. It should be noticed that the same preferential growth of single Ti layer can be seen even in the case of amorphous silica SiO₂ substrate (Fig. 3.3). The presence of TiO₂ rutile polymorphic form can be detected in the diffraction patterns of double TiO₂/Ti/Si(111) and triple Ti/TiO₂/Ti/Si(111) layers. Weak traces of this phase can be seen at $2\theta=27.4^\circ$ (rutile (110) plane), 55° (very broad peak from rutile (211) and (220) planes), and at about 90° (rutile (222) plane). The most intense rutile TiO₂ diffraction peaks are seen easily when TiO₂ is the uppermost layer in the structure. When the Ti layer with a thickness of about 40-50 nm is deposited on top of TiO₂, the peaks from the TiO₂ layer almost disappear with the exception of the strongest one attributed to (110) plane in the rutile structure.

Fig. 3.3 (bottom) shows XRR curves for the same 3 films. Quite reasonable fits to the experimental data were obtained for all three structures. The model of a single layer requires 5 fitting parameters among which the most important are its thickness and density as well as the interface roughness. Three layer structure requires 11-parameter fit. The proposed structure used for fitting is given in the inset of Fig. 3.3 (bottom). All the parameters of the best-fit procedure are listed in Table 3.2. As shown, the film density is 4.57 - 4.62 g/cm³ for Ti close to the bulk value and 3.72 - 4.07 g/cm³ for TiO₂, lower than the bulk value [139]. The interface roughness is found to be of the order of 1.3-3.2 nm, which is typical for samples grown by the magnetron sputtering.

The measured and simulated RBS spectra of all three samples are shown in Fig. 3.4. A large Ti-peak related to the backscattered signal from the first Ti layer deposited on the Si(111) substrate (denoted as the Ti(1) layer) was observed at the energy of about 1400 keV. The backscattered signal from the TiO₂ layer deposited on top of the Ti(1) layer (TiO₂ (2) layer) leads to an appearance of a shoulder on the right hand side of the Ti(1)-peak and a widening of the Ti peak as well as a visible oxygen peak around 700 keV. In the case of tri-layer film, a double maxima feature and a twice larger peak-width were observed, as a result of the backscattered signal from the Ti layer (Ti(3) layer) deposited onto the TiO₂ layer. The estimated layer thickness determined from the areal density by SIMNRA and using the value for the film density from XRR is given in Table 3.3. The RBS analysis shows that for all films with different layer geometries (i.e. with single, bi- and tri- layers), there is no Ti-interdiffusion (within the RBS error-limit) from the first Ti layer into the Si substrate and a sharp interface was always obtained.

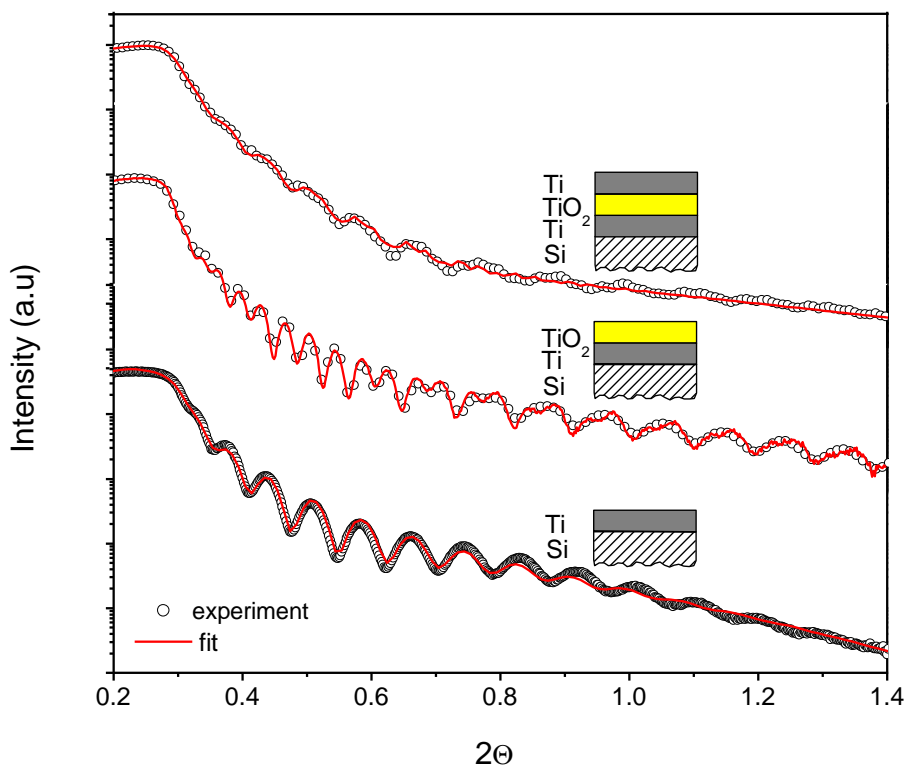
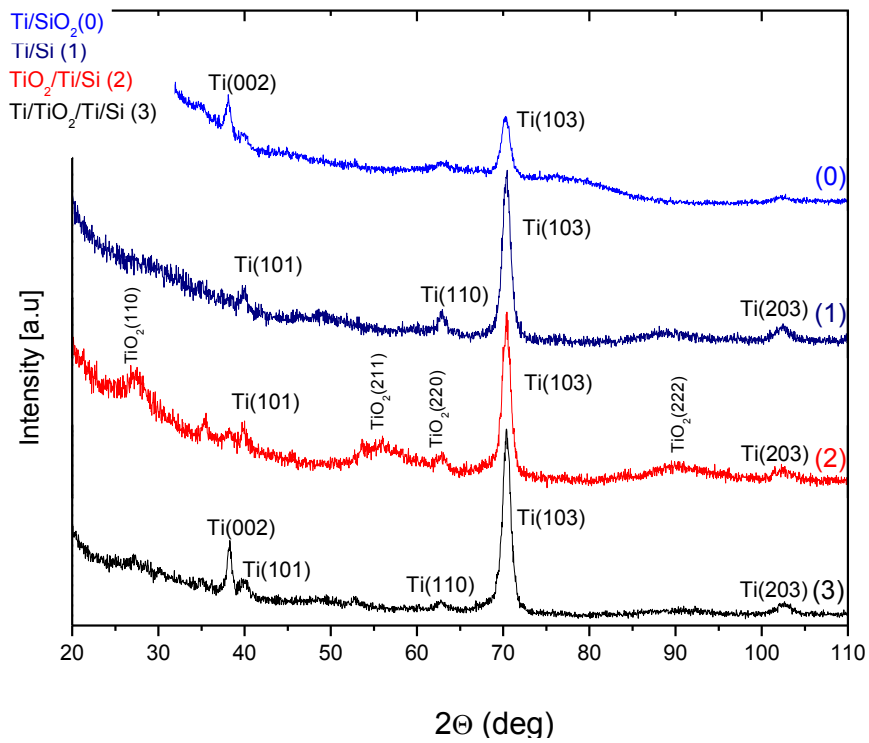


Figure 3.3. XRD pattern (top) and XRR curves (bottom) for Ti/Si(111), TiO₂/Ti/Si(111), Ti/TiO₂/Ti/Si(111) film with the layer thickness of each layer at about 50 nm (sample S1, D1, T1 in Table 3.1). The XRD pattern of the Ti/SiO₂ film is shown for comparison. The layer structure of the films used for XRR fitting is also labelled. The curves were shifted for clarity.

Sample	Ti (1)			TiO ₂ (2)			Ti (3)		
	<i>d</i>	ρ	<i>r</i>	<i>d</i>	ρ	<i>r</i>	<i>d</i>	ρ	<i>r</i>
Ti/Si(111)	47±1	4.62	3.2						
TiO ₂ /Ti/Si(111)	46±1	4.59	1.0	46±1	4.07	2.4			
Ti/TiO ₂ /Ti/Si(111)	40±2	4.60	1.3	51±2	3.72	1.8	49±2	4.57	1.9

Table 3.2. The layer- thickness (*d* (nm)), density (ρ (g/cm³)) and roughness (*r* (nm)) for different layers in three samples estimated from XRR. The number in parenthesis denote the layer sequence: Ti (1) - the first layer (Ti) deposited directly onto the Si(111) substrate, (2) - the second layer (TiO₂) deposited onto the Ti(1) layer, Ti(3) - the third layer deposited onto the TiO₂(2) layer. (Sample S1, D1, T1 in Table 3.1).

Some small interdiffusion can be seen at the Ti-TiO₂ interface for the bi-layer film and at both Ti-TiO₂ and TiO₂-Ti interface of the tri-layer film. However, since we use the standard RBS, it would be ambiguous to discuss about the (interface) layer with a thickness of several nanometers. And thus we take the interface roughness determined from XRR measurements.

Optical spectrophotometry allows to determine the optical constants: refractive index *n* and extinction coefficient *k* of thin films from the measured transmittance *T*(λ) and reflectance *R*(λ) spectra over a given wavelength λ range. When the optical constants are known, by fitting the theoretical model to the experimental data one can obtain a good estimate of a layer thickness. In the case of optical measurements the commercial software Film Wizard has been used. Data analysis has been performed using a fitting model where a thin film can be divided into as many layers as necessary. Usually, one starts with a single layer according to the principle that the smallest number of fitting parameters, the more reasonable result is obtained. Different types of the dispersion relations for the refractive index *n* and extinction coefficient *k* have been tried for TiO₂. Effective medium approximation (EMA) is commonly used as a model of TiO₂ with air void fraction of up to 50%. Surface roughness and sample porosity can be simulated in such a way. But in the case of very thin films with a relatively small diffused reflectance and transmittance of light, one can neglect the roughness. In this work, the optical constants *n* and *k* of single layers of Ti and TiO₂ were calculated from the experimental data of the samples deposited intentionally on the transparent substrates. These *n* and *k* sets for all wavelengths were used to fit the film thickness for Ti/Si(111), TiO₂/Ti/Si(111), Ti/TiO₂/Ti/Si(111) structure. The experimental and

fitted $R(\lambda)$ and $T(\lambda)$ for $\text{TiO}_2/\text{SiO}_2$ and for Ti/SiO_2 films along with the optical constants derived from direct fitting of the spectra are shown respectively in Figs. 3.5 and 3.6.

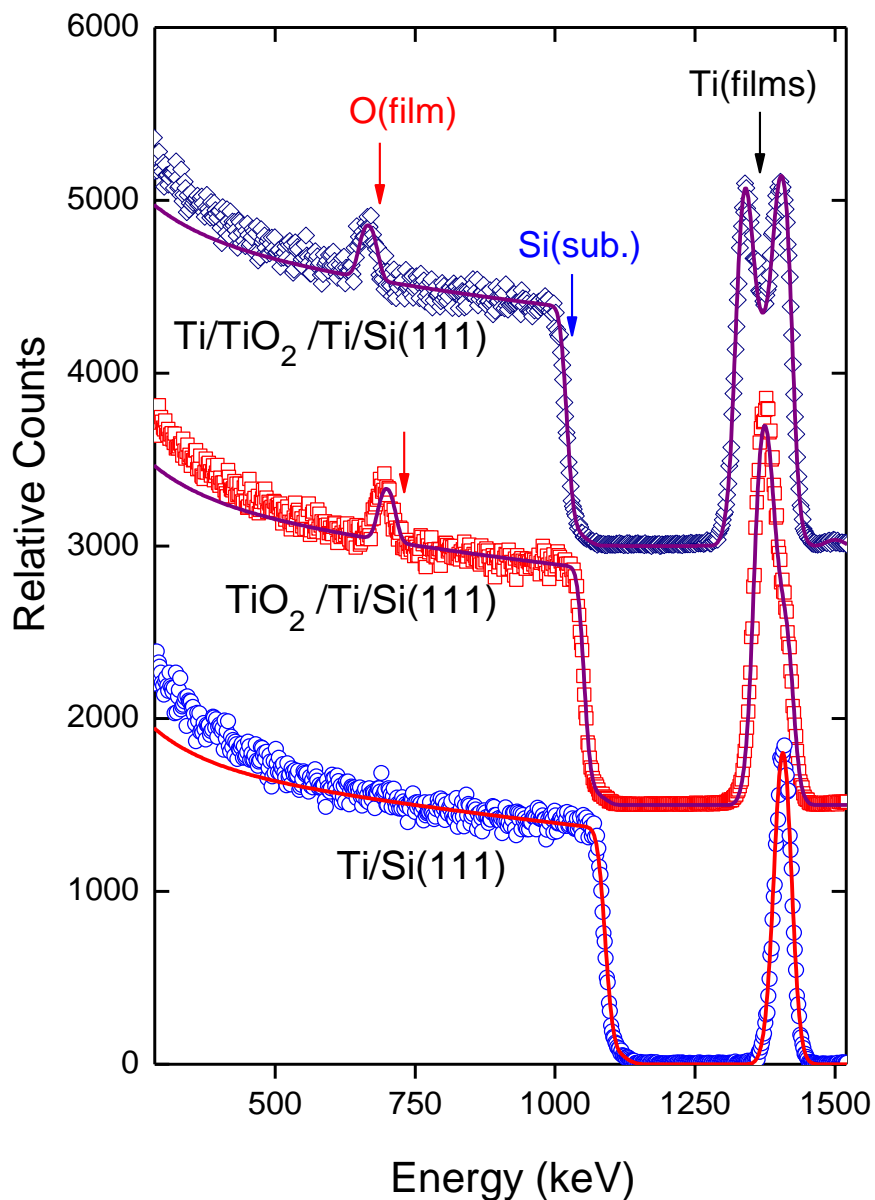


Figure 3.4. Random RBS (markers) and SIMNRA (lines) simulated spectra for $\text{Ti}/\text{Si}(111)$, $\text{TiO}_2/\text{Ti}/\text{Si}(111)$ and $\text{Ti}/\text{TiO}_2/\text{Ti}/\text{Si}(111)$ film with the layer thickness of each layer at about 50 nm. (Sample S1, D1, T1 in Table 3.1). The curves were shifted to guide the eyes. The arrows mark the Ti and O signals in the films (Ti(films), O(film)) and the Si signal from the substrate (Si(sub.)). RBS experiments were performed with a 2 MeV He^+ ion beam and a backscattering angle of 171° .

Sample	XRR			RBS			Optical measurements		
	Ti (1)	TiO ₂ (2)	Ti (3)	Ti (1)	TiO ₂ (2)	Ti (3)	Ti (1)	TiO ₂ (2)	Ti (3)
Ti/Si(111)	47±1	-	-	41.1			46±1		
TiO ₂ /Ti/Si(111)	46±1	46±1	-	47.3	47.8		46±1	42±1	
Ti/TiO ₂ /Ti/Si(111)	40±2	51±2	49±2	39.4	49.4	47.3	-	-	-

Table 3.3. Comparison the layer-thickness (in (nm)) for Ti/Si(111), TiO₂/Ti/Si(111) and Ti/TiO₂/Ti/Si(111) film estimated from 3 different measurements; X-ray reflectometry (XRR), Rutherford back-scattering (RBS) and optical measurements. The layer notation is the same as that in Table 4.2. (sample S1, D1, T1 in Table 3.1).

We notice here that the optical constants of TiO₂ and Ti films deposited by magnetron sputtering differ from the bulk values reported in the literature [139] due to the differences in the film morphology and a higher porosity resulting from the columnar growth and lower density. The film density affects the refractive index while the extinction coefficient reflects the changes in the film stoichiometry.

Fig. 3.7 demonstrates the result of modelling of $R(\lambda)$ spectra for the deposited layered structures of Ti/Si(111) and TiO₂/Ti/Si(111). The only fitting parameter in this case was the layer thickness (the optical constants were taken from Figs. 3.5 and 3.6). As it was shown, reasonable fits could be obtained for Ti/Si(111) and Ti/TiO₂/Ti/Si(111) films. An attempt to find the reasonable thicknesses of three layers in the case of Ti/TiO₂/Ti/Si(111) failed largely because the Ti uppermost layer is highly absorbing. The simulation of the transmittance of 50 nm Ti layer indicated that only up to 5% of incident intensity reaches the undelaying TiO₂ transparent layer.

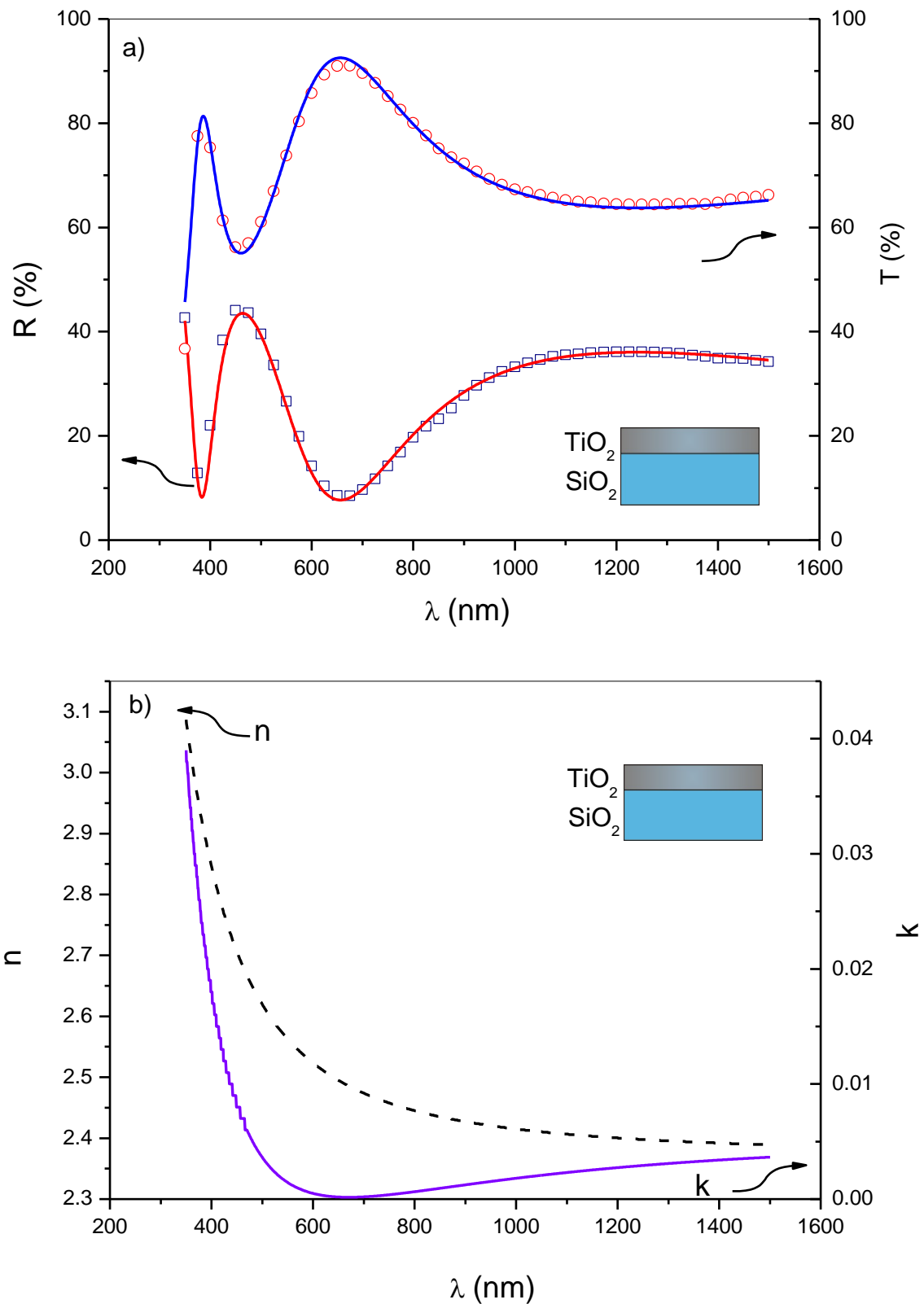


Figure 3.5. The measured (markers) and fitted (lines) reflectance $R(\lambda)$ and transmittance $T(\lambda)$ spectra (a) of a single layer TiO_2 deposited on a transparent amorphous SiO_2 substrate and the determined optical constants (b): the refractive index n (dashed) and extinction coefficient k (solid).

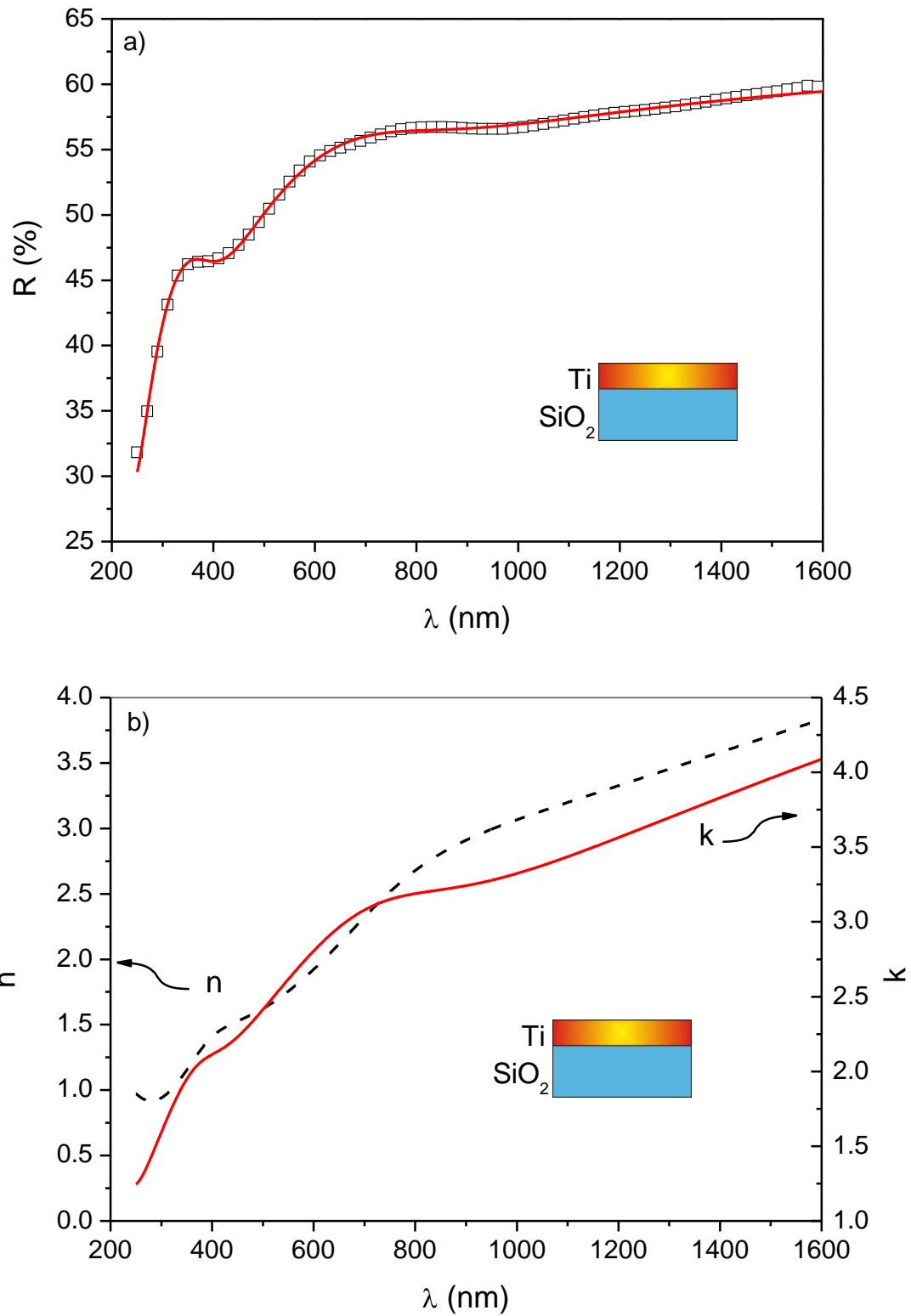


Figure 3.6. The measured (markers) and fitted (lines) reflectance $R(\lambda)$ spectra (a) of a single layer Ti deposited on a transparent amorphous SiO₂ substrate and the determined optical constants (b): the refractive index n (dashed) and extinction coefficient k (solid).

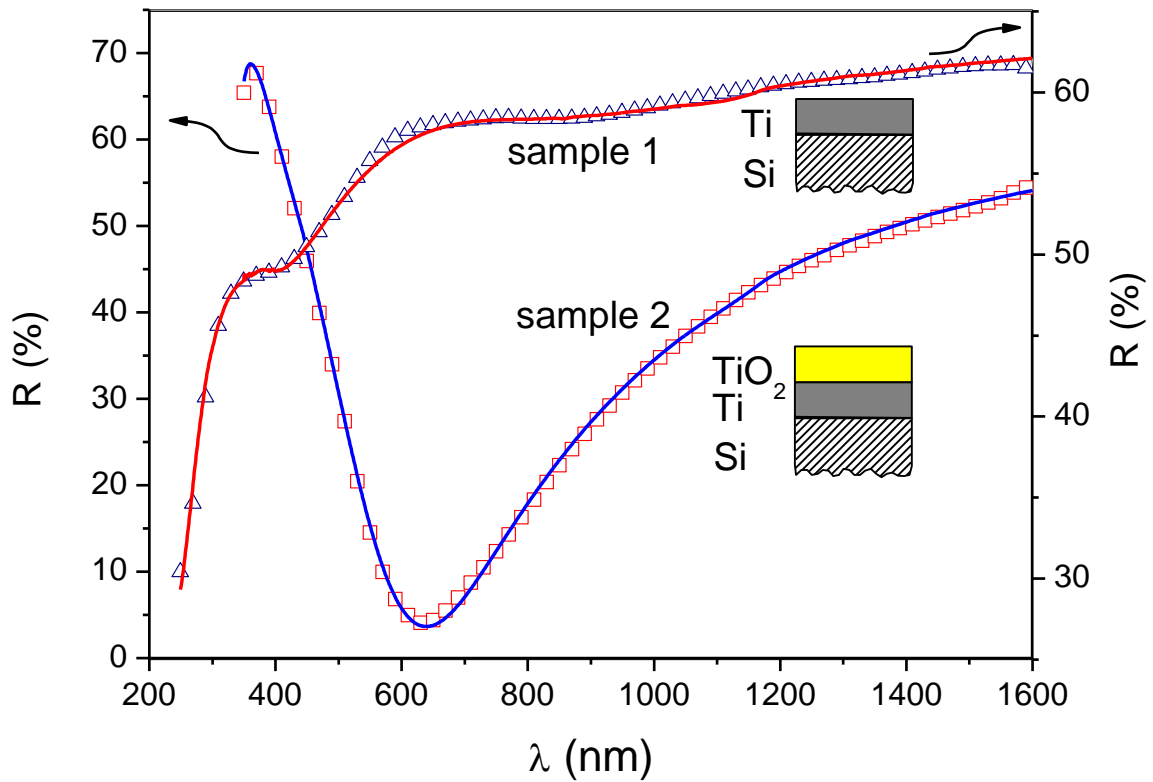


Figure 3.7. The measured (markers) and fitted (lines) reflectance $R(\lambda)$ spectra of Ti/Si(111), $\text{TiO}_2/\text{Ti}/\text{Si}(111)$ films. (Sample S1, D1 in Table 3.1).

Analyzing thickness values obtained from different fitting routines (Table 3.2) one may notice that in general there is a good agreement. However, there are two exceptions. The first one concerns the thickness of 42 nm of $\text{TiO}_2(2)$ from the optical measurements what is much smaller than that determined from XRR and RBS. Such large discrepancy may result from the presence of only one minimum in the reflectance spectrum and the fact that this structure consists of two layers. In such a case the number of fitting parameters is larger than for a single layer of Ti. The second exception is 41.1 nm for Ti(1) from the RBS studies as compared with XRR and optical measurements. However, in the RBS the film thickness is not an independent fitting parameter. One have to assume the film density and to calculate the film thickness as it was done in our case.

3.2 The thicker Ti-TiO₂ films on Si(111) substrates

We have performed RBS measurements on different films with different geometries and layer thickness. The change/development of Ti, O and Si signals for selected films are shown in Fig. 4.8. For the single-layered films, a single sharp Ti peak is always observed. Increasing the thickness of Ti (1) layer leads only to an increase of the width and intensity of the Ti(1) peak and a shift of the Si-edge to lower energies. For the bi-layer films, introduction of the TiO₂(2) layer leads to the appearance of the oxygen signal revealed by the distinguished peak on the high “background” signal from Si substrate. The shoulder-like feature in the Ti peak appeared for the films with layer-thickness below 50 nm (i.e. sample D1). With increasing the thickness of TiO₂(2) layer, the shoulder changes into a plateau as a result of a large widening of the signal coming from such a layer (the Ti(2) signal). From our more detail investigation of the shape of the RBS spectra as a function of the layer thickness, we found out that the plateau figure becomes visible for the TiO₂(2) layer thickness > 100 nm (e.g. sample D2). For the tri-layer films, the double maxima are always observed related to Ti signals. The intensity and width of these double maxima increase with increasing the layer thickness, while the minimum between them is governed by the Ti(2) signal in the TiO₂ layer. Obviously, similar intensity and width of the two maxima was obtained for the films in which the layer thickness of the Ti(1) and Ti(3) layer are similar (i.e. sample T1 and T4). In all cases, increasing the total film thickness implies a widening of the O-signal and a shift of the Si-edge to lower energies.

Introduction of the TiO₂ layer in the bi- and tri-layered films deposited on Si(111) substrate leads to the appearance of the oxygen signal revealed by the distinguished peak on the high background signal from the Si substrate. It is related to the fact that the atomic mass of oxygen (16) is smaller than that of Si (28) and thus the energy of scattered He⁺ ions from the oxygen atoms in the films is always smaller than that from the Si atoms in the substrates. Thus for these films the uncertainty is very high for fitting the data below the Si-edge, i.e. in the energy region where the oxygen and Si signals are combined.

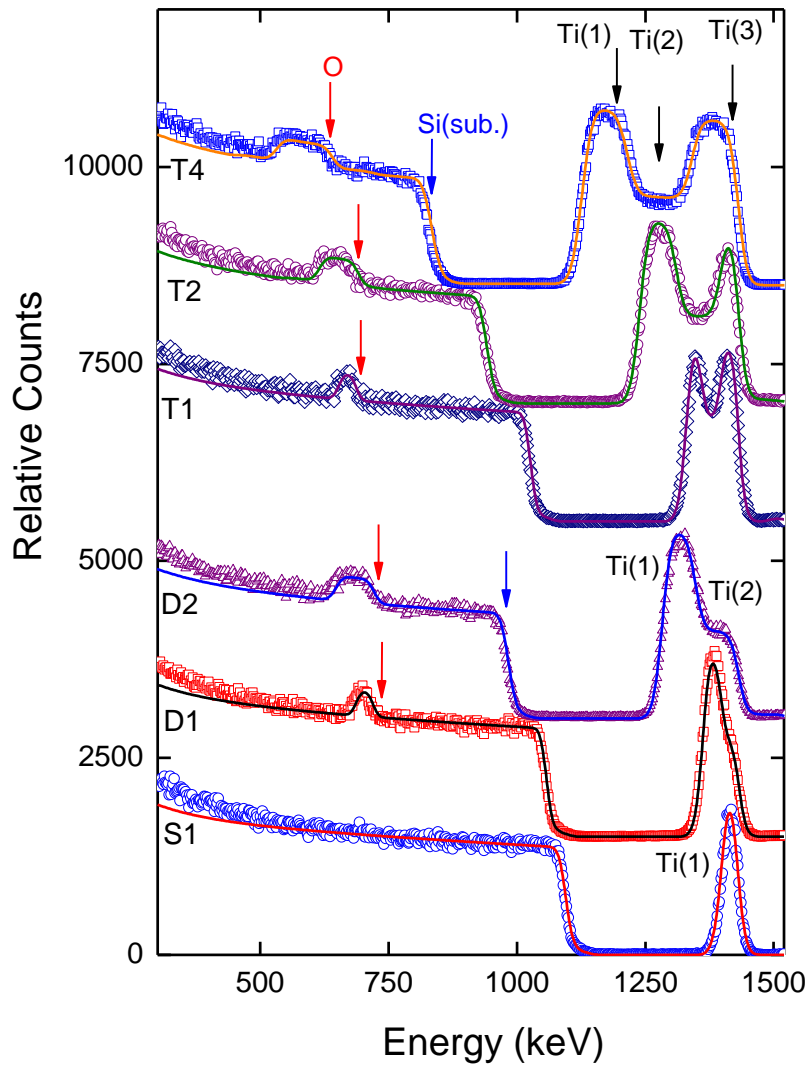


Figure 3.8. The change/development of Ti, O and Si signals in RBS spectra with changing film geometry and layer thickness. The random and SIMNRA simulated RBS spectra are shown by markers and solid lines, respectively. The sample notation and layer thickness are given in Table 3.1. The curves have been shifted as a guide for the eye. The arrows mark the Ti- and O signals in the films and the Si signal from the substrate. Ti (1): the Ti layer deposited directly on the Si substrate. Ti(2): the TiO₂ layer deposited on the Ti(1) layer. T(3): the Ti layer deposited on the TiO₂ layer. RBS experiments were performed with a 2 MeV He⁺ ion beam and a backscattering angle of 171°.

3.3 The Ti-TiO₂ films deposited on C-foils

As already mentioned, for a more precise analysis of the oxygen signal (and thus get better fits of the RBS spectra), we prepared two film series with similar layer thickness and film geometry, one on Si(111) substrates and the other one on C-foil. The atomic mass of oxygen (16) is bigger than that of carbon (12). Thus the oxygen signals from the films will be appeared separately in the RBS spectra, i.e. at energy higher than that of C-edge coming from

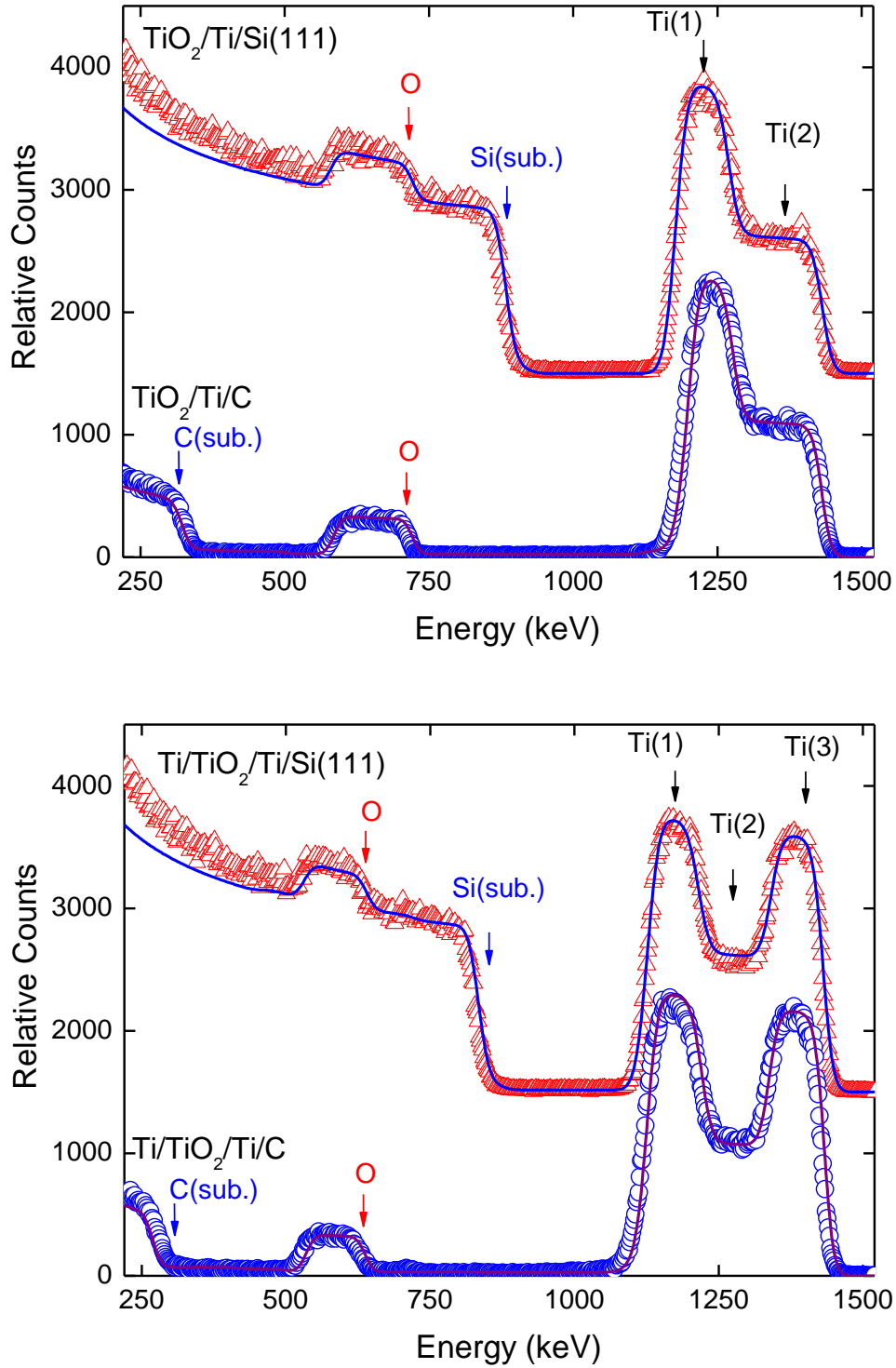


Figure 3.9. Random RBS (markers) and SIMNRA (lines) simulated spectra for $\text{TiO}_2/\text{Ti}/\text{Si}(111)$ and $\text{TiO}_2/\text{Ti}/\text{C}$ -foil (left) and $\text{Ti}/\text{TiO}_2/\text{Ti}/\text{Si}(111)$ and $\text{Ti}/\text{TiO}_2/\text{Ti}/\text{C}$ -foil (right); samples D4, D4-C, T4 and T4-C in Table 3.1. The arrows mark the Ti- and O signals in the films and the Si or C signal from the substrate (S(sub.), C(sub.)). RBS experiments were performed with 2 MeV He^+ ion beam and the backscattering angle of 171° .

the C-substrate. The oxygen concentration can be then analysed in more details in those films and would give additional supporting information for the films deposited on Si substrates. Comparison of the measured and simulated RBS spectra of selected bi- and tri-layered films deposited on Si(111) and C-foil is shown in Fig. 3.9. The thickness layer of each layer was chosen in the range of 100-150 nm (samples D4, D4-C, T4 and T4-C in Table 3.1). Indeed, the determination of layer thickness and element concentration by means of SIMNRA simulation performed on the films deposited on C-foil seems to be simpler, due to the fact that the oxygen signal appears a broad peak on the zero-background, as expected. However, while there is almost no interdiffusion in the films deposited on Si(111) substrates, a carbon diffusion (up to 10%) into the film was observed. If the film are thin (the layer thickness <30 nm), the carbon can be found even if in the surface layer. Since no carbon was detected in the surface layer for the thick films (no carbon surface contamination) with the film thickness >100 nm, we assume that the carbon on the surface of thin film was due to carbon segregation from the substrates.

In summary, the main outcome of our investigations of numerous thin films of Ti-TiO₂ system with different film-geometry and layer thickness is summarized as follow:

1/ Three complementary methods XRR, RBS and optical spectrophotometry were used to study the properties of layered structures of Ti-TiO₂ thin films with a nominal thickness of 50 nm system deposited onto Si (111) substrates by magnetron sputtering. The results show that:

- All three used methods give comparable results for the layer thickness. However, each layer thickness is smaller than the nominal value of 50 nm.
- The film density was a fitting parameter of XRR and was applied to calculate the film thickness from RBS. Density of TiO₂ thin film is smaller than that of the bulk value. The discrepancies in the thickness values can be attributed e.g. to the inhomogeneity of the film thickness and specificity of the methods used.
- SEM images indicate that there is some intergrowth between the top Ti and TiO₂ layer. The underlying layer of Ti produces a better defined interface with TiO₂. This effect is most probably due to the columnar-structure growth of TiO₂ that creates different type of substrate for the Ti growth. Namely, in the bottom layer Ti nucleates and grows on the compact, well-defined Si wafer, while the uppermost layer of Ti grows on top of caps of TiO₂ columns. There is a possibility that to some extent Ti penetrates along the columns. The uppermost layer of Ti is more rough than the layer of Ti that grows directly on the smooth Si(111).

2/ No Ti interdiffusion from the first Ti layer into the Si substrate was also revealed in the thicker Ti-TiO₂ films deposited onto Si(111) substrates, there is some small interdiffusion at the Ti-TiO₂ interface for the bi-layer films and at both Ti-TiO₂ and TiO₂-Ti interfaces of the

tri-layer film. It is related to the intergrowth between the Ti and TiO₂ layer most probably due to the columnar-structure growth of TiO₂, as revealed for the thin(ner) films.

3/ The more precise determination of layer thickness and element concentration by means of SIMNRA simulation was obtained on the films deposited on C-foils. However, a carbon diffusion (up to 10 at.%) into the film was observed.

Chapter 4

Effect of hydrogenation on the structure and physical properties of Ti-TiO₂ thin films

Application of hydrogen would affect microstructure and properties of thin-film and multilayer structures. On the other hand, the atom mixing, diffusion across the interfaces can also influence the hydrogen uptake. Thus selected bi- and tri-layer Ti-TiO₂ films subjected for hydrogen charging at atmospheric pressure and/or at high pressures were then investigated focusing on the film stability, the hydrogen uptake and hydrogen storage under different conditions. The film notation is presented in Table 3.1. in Chapter 3.

The mechanism by which the oxide influences hydrogen permeation into Ti and its alloys is still not well established, but it is known that diffusion of hydrogen in TiO₂ is slower than in the pure metal [55,56]. Additionally, the atomic transport can be improved using palladium layers. Some theoretical models, in particular based on finite elements method, have been used to simulate the behaviour of hydrogen in titanium oxide layers [64]. In this chapter we present our investigations of resistivity, surface topography and hydrogen profiles and its diffusion through the different layers in Ti-TiO₂ films and those with additional Pd layers before and after charging with hydrogen as well as our study of hydrogenation of selected Ti-TiO₂ at high pressure up to 100 bar.

4.1 Hydrogen charging of Ti-TiO₂ films covered partially by Pd

In this section the results obtained for the bi- and tri-layered Ti-TiO₂ films covered partially by Pd (with notation D3+Pd and T3+Pd in Table 3.1), subjected for hydrogen charging at atmospheric pressure (1 bar) are presented. The films were charged with different time and at temperature of 300 °C. Since about 1/3 of the film surface was covered by an additional Pd layer, it allows us to investigate the hydrogen charging in the similar films without and with Pd-cover simultaneously.

4.1.1 Film surface and composition

Prior to other experiments the film composition and thickness were studied by RBS. The experiments were performed on the films both on the area without Pd and with Pd covering. Beside of signals from backscattering of He⁺ ions on Ti-, O- and Si atoms, a sharp

peak revealed the binary elastic collision of He^+ ion on Pd atoms was observed, shown in Fig. 4.1. The thickness of the Pd layer is 19-20 nm (see Table 3.1), i.e. as nominal thickness. The RBS analysis indicates that there is no interdiffusion at the interfaces, in a good agreement with the SEM image revealing a smooth and homogenous surface layer with a sharp borderline between Ti surface layer and Pd layer (see Fig. 4.3).

Also, prior to measurements related to hydrogen influence on titanium films, the investigations of structure and chemical composition of titanium surface, with and without palladium layer, have been performed by using Auger Electron spectroscopy (AES) with energy of primary beam 3 keV. As shown in Fig. 4.2, carbon impurity is present (peak at energy of 271 eV) in both titanium and palladium layers. In the spectra of titanium, additional peak at 512 eV is observed, which corresponds to oxygen.

The topography of titanium and palladium layers studied by High Resolution Scanning Electron Microscopy (HR-SEM) was shown in Fig. 4.3. In both cases, we observed smooth and homogenous layers, without any islands or granulations (Fig. 4.3a). After hydrogen charging, granulation of titanium surface was observed (Fig. 4.3b), as it has been already described by Nakao et al. [140]. Surface of palladium layer was not changed by increasing the amount of hydrogen in the layer. Nevertheless, some cracks were observed, because of the elevated charging temperature of 300°C.

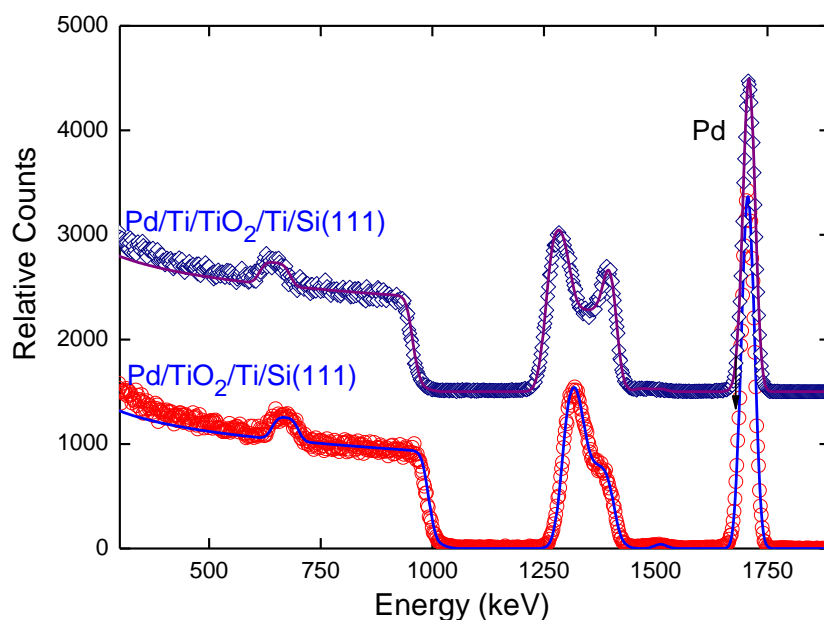


Figure 4.1. Random RBS (markers) and SIMNRA (lines) simulated spectra for $\text{TiO}_2/\text{Ti}/\text{Si}(111)$ and $\text{Ti}/\text{TiO}_2/\text{Ti}/\text{Si}(111)$ films covered by 20 nm-thick Pd layer used for H-charging experiments (samples D3+Pd, T3+Pd in Table 3.1). The Pd signal was indicated by the sharp peak at around 1.7 MeV. RBS experiments were performed with 2 MeV He^+ ion beam and the backscattering angle of 171° .

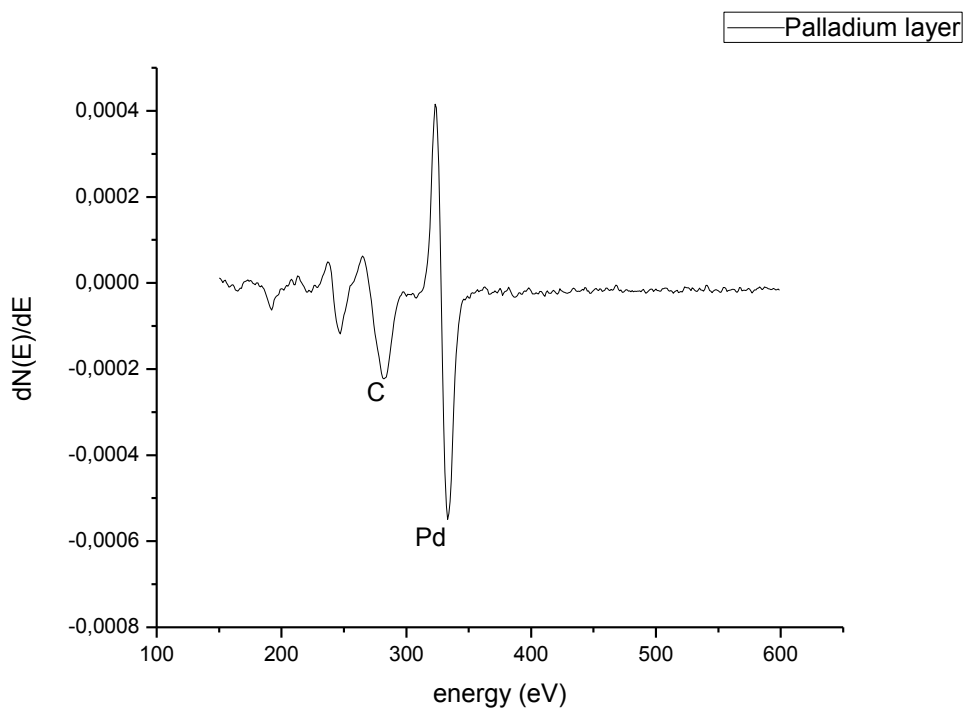
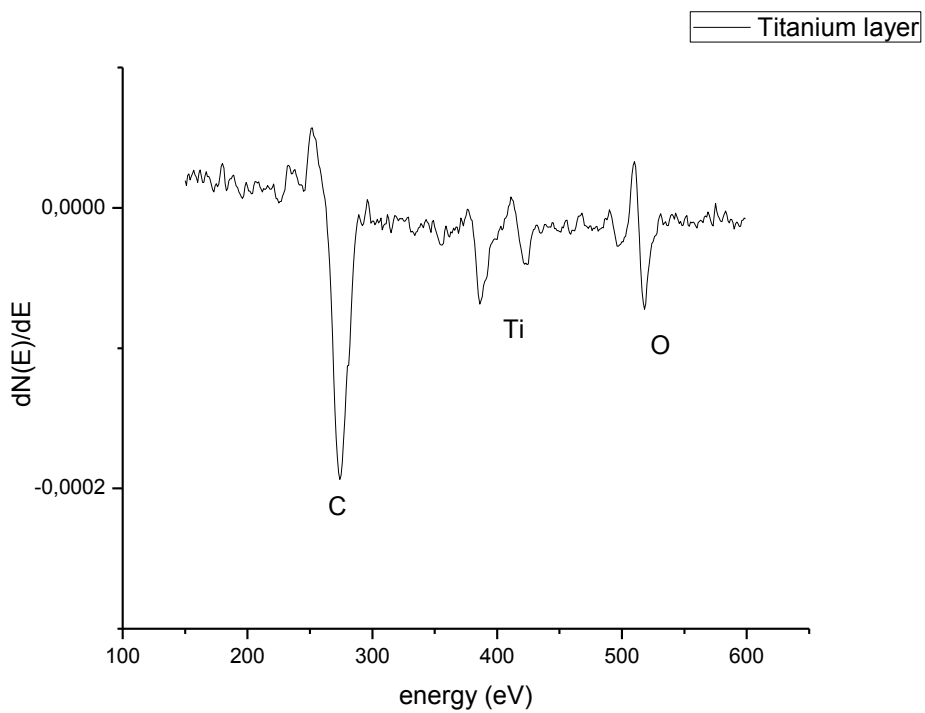


Figure 4.2. AES data for titanium and palladium layers.

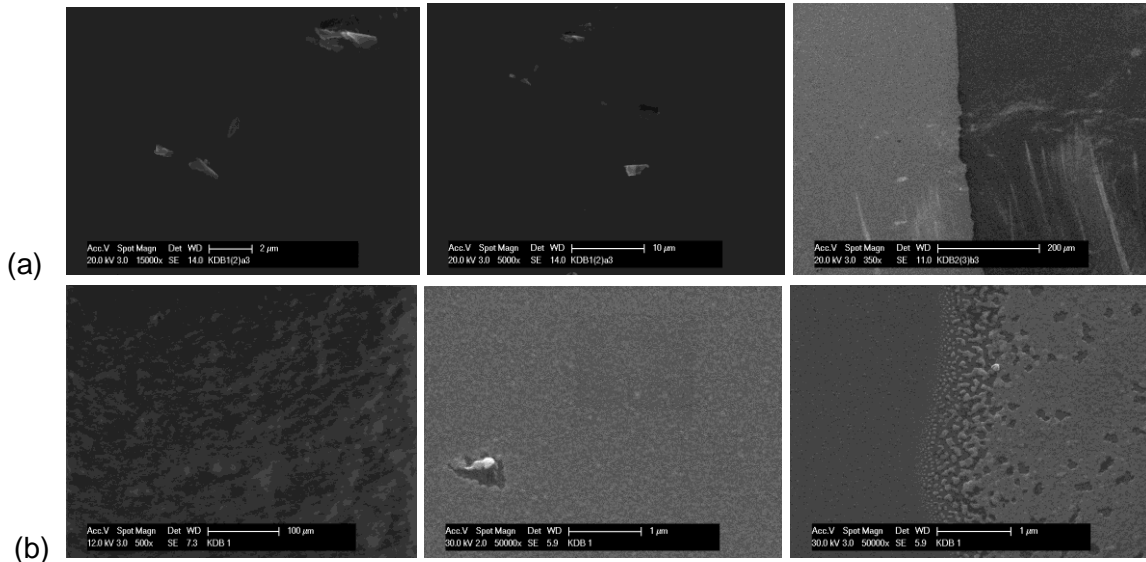


Figure 4.3. HR-SEM images for sample surfaces with titanium in the top layer and that partially covered by Pd revealing the titanium and palladium border before (a) and after (b) hydrogen charging.

4.1.2 Resistivity of hydrogenated Ti thin films

Hydrogen in transition metals, like Ti, tends to occupy tetrahedral interstitial sites [2]. As it is well known, one can reach the best solubility of H in the case of the β -phase (12 tetrahedral and 6 octahedral interstitial positions). The solubility of hydrogen in α -titanium is quite negligible. For small amounts of hydrogen in titanium (α -Ti), hydrogen forms a disordered interstitial solution in the *hcp* Ti lattice (only 4 tetrahedral interstitial sites) and hydrogen atoms act as extra scattering centres for the conduction electrons. Therefore, the resistivity of the layer will be increased. Hydrogen atoms in titanium represent a model system for concentrated lattice gas [62]. This system is an ideal physical realization of this model because of the wide ranges of hydrogen solubility and the high mobility of hydrogen in Ti. Therefore, it can be described using the lattice gas automata (LGA) or lattice gas cellular automata (LGCA) methods.

With increasing amount of hydrogen in the sample, titanium hydride with H-vacancies (under-stoichiometric composition) will be created (*fcc* lattice) and hydrogen atoms will occupy tetrahedral voids, so the contribution of conducting electrons becomes larger than the contribution of scattering centres in the lattice. Consequently, the resistivity will be decreased [85]. Resistivity of the top titanium layer was measured for each sample using the 4-points method and was calculated using the Equation 4.1:

$$\rho = \frac{\pi}{\ln 2} \cdot d \cdot \frac{U}{I}, \quad (4.1)$$

where d is the thickness of the titanium layer, U is the measured voltage and I is the applied current. Before hydrogen charging, the measured average resistivity for each sample was in good agreement with the literature.

The resistivity measured on the titanium layer of the sample Pd/Ti/TiO₂/Ti/Si (on the area that was not covered with Pd) before hydrogen charging was found to be $1.76 \cdot 10^{-7} \Omega\text{m}$, as shown in Fig. 4.4. After the first charging step, resistivity decreased to $1.21 \cdot 10^{-7} \Omega\text{m}$ and after the second charging step, the resistivity decreased again down to $0.98 \cdot 10^{-7} \Omega\text{m}$. Because of the conditions of hydrogen charging (at 300 °C the concentration of hydrogen in α , β and δ (hydride) phases are 6.72, 39 and 51.9 at.%, respectively [82]), we can state, that already after the first step of hydrogenation, the pure β -phase or at least a mixed ($\alpha+\beta$)-phase has been reached. The sharp decrease in the resistivity seems to confirm this statement. After the last charging step N-15 measurements have been performed. The results show a hydrogen concentration of over 50% in the titanium layer, meaning that probably the δ phase with *fcc* lattice has been achieved. Up to this region, Debye's temperature, as well as electronic specific heat coefficient, decrease linearly with increasing amount of hydrogen [141]. Obtaining higher H concentration values (over 60 at.%) an “electronically driven” *fcc*↔*fct* transformation will be induced [142,143].

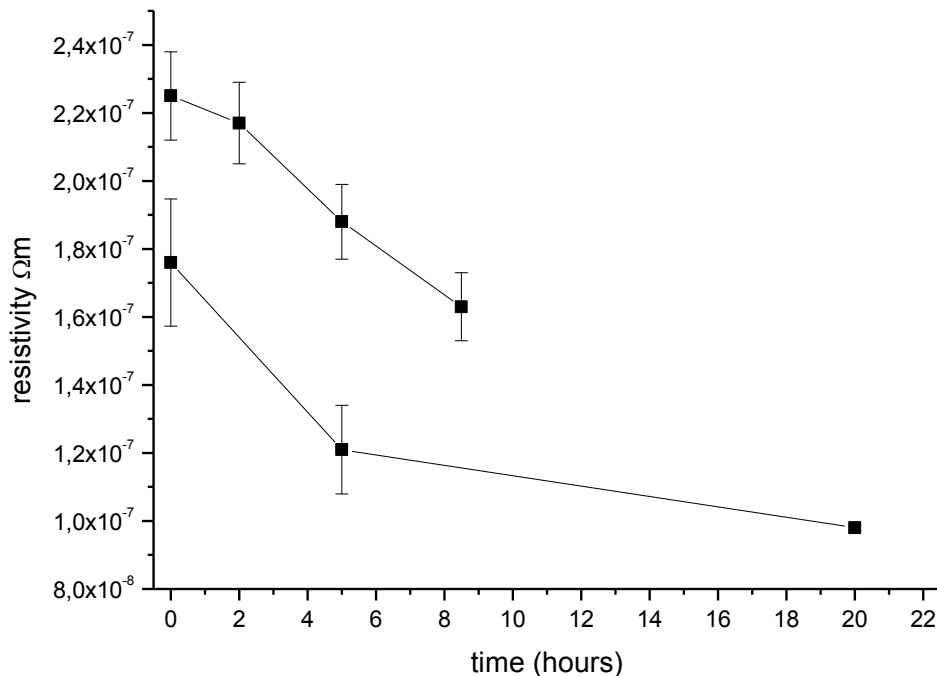


Figure 4.4. Charging time dependence of resistivity in titanium layer for samples Ti/TiO₂/Ti/Si(111) with and without Pd cover (samples T2 and T3 in Table 3.1) .

In the Ti/TiO₂/Ti/Si sample the resistivity measured prior to hydrogen charging was found to be $2.25 \cdot 10^{-7} \Omega\text{m}$. In both cases (samples with and without palladium) the value of resistivity is slightly under the literature value, probably because samples contained small amount of hydrogen already before hydrogen charging (the presence of H was confirmed by SIMS measurements). It is also visible from Fig. 4.4, that the resistivity is lower for samples covered by palladium (because of the supporting role of Pd for hydrogen dissociation and diffusion into the metal). However, later both curves are decreasing almost parallel. After the first charging step, resistivity decreased to $2.17 \cdot 10^{-7} \Omega\text{m}$, after the second charging step it decreased to $1.88 \cdot 10^{-7} \Omega\text{m}$, and after the last charging it decreased to $1.63 \cdot 10^{-7} \Omega\text{m}$. These change in the resistivity suggests, that after the first process of charging the ($\alpha+\beta$)- or β -phase was achieved, and after the second process the pure β -phase was obtained. Further N-15 measurements showed about 40 at.% of hydrogen in the sample, meaning that in this case the δ phase has not been reached.

As already mentioned, metal-insulator-metal (MIM) structures such as Ti/TiO₂/Ti have been proposed for resistive random-access memories (ReRAM) because their resistance can be switched reversibly by an applied electric field [54]. However, methods for improving the uniformity of resistive switching parameters are still investigated. Li et al. [144] reported nitrogen annealing as a method improving the broad variations of the resistive switching parameters in the as-deposited TiO_x films. Changing the resistivity of titanium by hydrogen charging could also be a way to modify properties of such systems.

4.1.3 Hydrogen profiling in Ti-TiO₂ films

To obtain the hydrogen profiles in samples Pd/Ti/TiO₂/Ti/Si (111) and Ti/TiO₂/Ti/Si (111) with the same titanium layer thicknesses and the same hydrogen charging times and temperature, SIMS and N-15 measurements have been performed. For these samples, partially covered by palladium, it is clearly visible that hydrogen charging enhances the hydrogen concentration (storage) in both (top and bottom) titanium layers, but no changes were observed in the oxide layer.

Titanium is a metal that was widely investigated as a potential material for hydrogen storage, because of its high hydrogen storage capacity (67 at.%) and its very low out-gassing property [145]. In the titanium-hydrogen system, the heat of solution and the formation energy of the hydride, TiH₂, are both negative. At elevated temperatures, hydrogen atoms in the titanium formed hydrides immediately. The hydride formation is therefore controlled by the diffusion process of the hydrogen atoms, and numerical calculations concerning this topic have also been performed, and some theoretical models have been developed [146]. One of these models is based on the idea, that complex defects will contribute to the surface diffusion flux at temperatures approaching the melting point and allows to determine diffusion coefficient even in the case of very complex and defected systems.

SIMS results show that after charging the concentration of hydrogen was increased in titanium layers. However, in the titanium dioxide layer its concentration remains the same as before (Fig. 4.5). Results of N-15 measurements show an accumulation of hydrogen in both titanium layers (up to 50 at.%) but only a small amount (less than 5 at.%) in the oxide layer. These results are in a good agreement with results of SIMS measurements. The comparison of SIMS and N-15 is presented in Fig 4.6. It seems to be clear that hydrogen diffuses through the oxide layer without any accumulation there. This fact can be explained by the mechanism, proposed by Bates et al. [147], who described the diffusion of hydrogen and its isotopes through a TiO₂ sample in direction parallel and perpendicular to the *c* axis. They showed, that because of its large open channels parallel to the *c* axis, diffusion of hydrogen is very rapid in this direction and proceeds by a proton jump from one O²⁻ ion to another along this channel (so diffusion parallel to the *c* axis is much faster than in the perpendicular direction).

For a sample without palladium layer, the situation is quite similar, and differs only in the contents of hydrogen. Prior to charging some amount of hydrogen was observed by SIMS measurements because of the H absorption of the surface. Charging with hydrogen increased this amount in the top titanium layer significantly, but in the second titanium layer the concentration of hydrogen remains lower than in the case of the sample with palladium top layer (Fig. 4.7). This result indicates that palladium acts as a catalyst for gathering hydrogen in Ti and its diffusion through the TiO₂ layer. Results of N-15 measurements, shown in Fig. 4.8, indicate a high accumulation of hydrogen in the first titanium layer (~40 at.%) and a smaller amount in the second titanium layer (~15 at.%). Only a very small amount of hydrogen was observed in the oxide layer. This indicates that the lack of palladium on the top hinders hydrogen to penetrate into titanium, as well as into the second Ti layer through the titanium dioxide layer [64]. Pd supports the dissociation of H₂ molecules on the surface. Palladium atoms on the surface promote the dissociation of hydrogen molecules and so the H atoms can be easily absorbed by the bulk of the metal and diffuse through other layers. These results are in good agreement with concentration depth profiles from SIMS measurements.

In summary, the main characteristics of hydrogen absorption by titanium and titanium dioxide thin films were investigated with specific emphasis on the hydrogen diffusion and its storage in each layer. It is clearly visible from the results that palladium acts as a catalyst for hydrogen diffusion through TiO₂ layer and increases the maximum H concentration up to a value of over 50 at.% (under the palladium-covered part) instead of about 40 at.% and 15 at.% in first and second titanium layer, respectively if it is not covered by palladium. Hydrogen profiles obtained both by SIMS and N-15 measurements proved this higher hydrogen concentration in good agreement in samples with partially covered top layers. Concerning the surface, hydrogen charging caused a granulation of titanium layer. Also the palladium layer was changed (cracks on the surface) because of the elevated temperatures during the hydrogen charging process. The resistivity of the samples has decreased with increasing hydrogen charging according to the predictions as it was pointed out in the discussion.

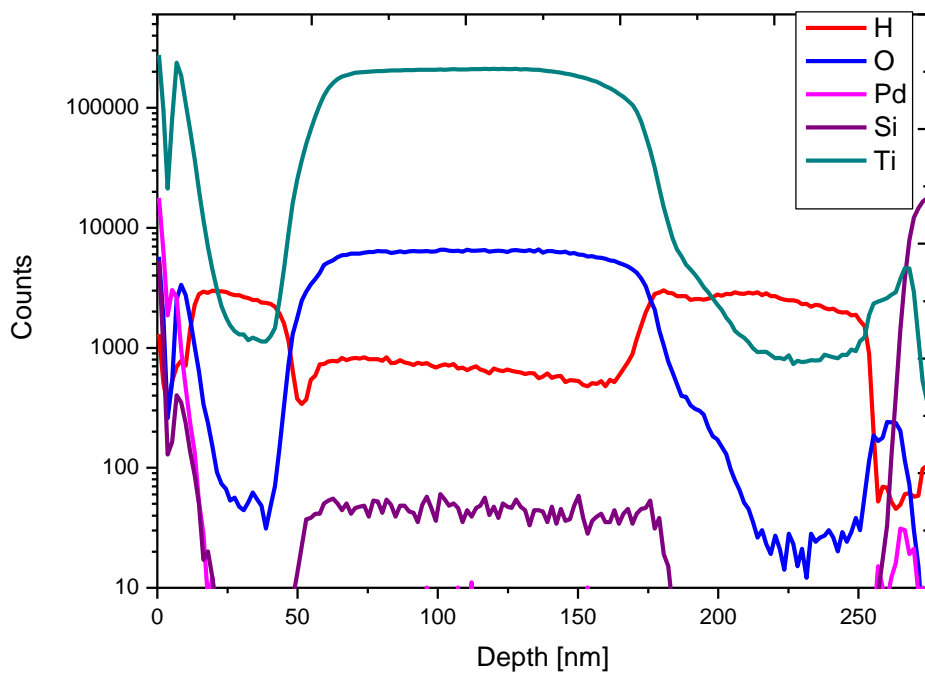
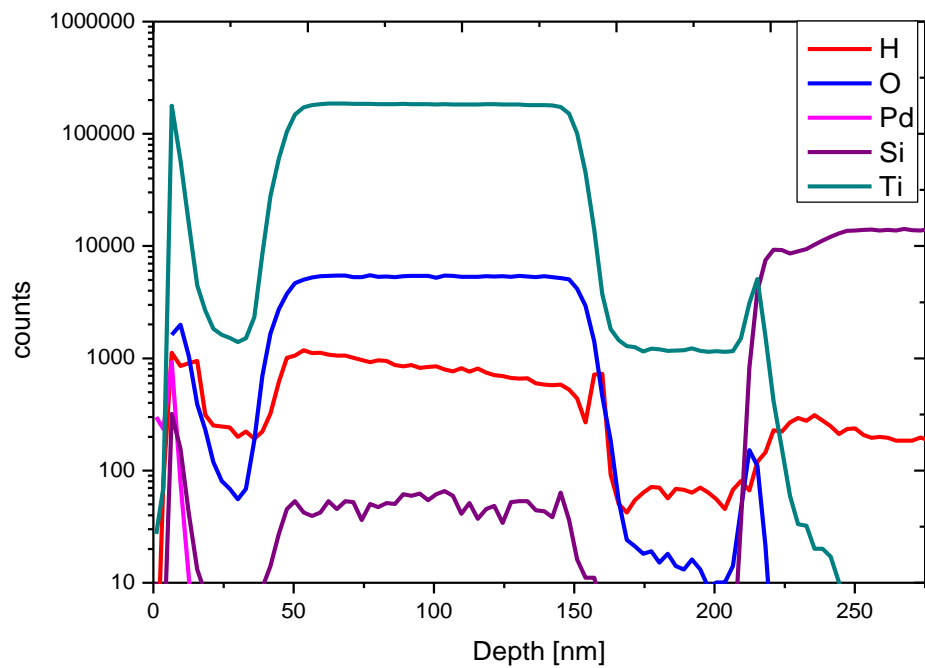


Figure 4.5. SIMS profiles for the sample covered with Pd, Pd/Ti/TiO₂/Ti/Si, before (top) and after (bottom) hydrogen charging.

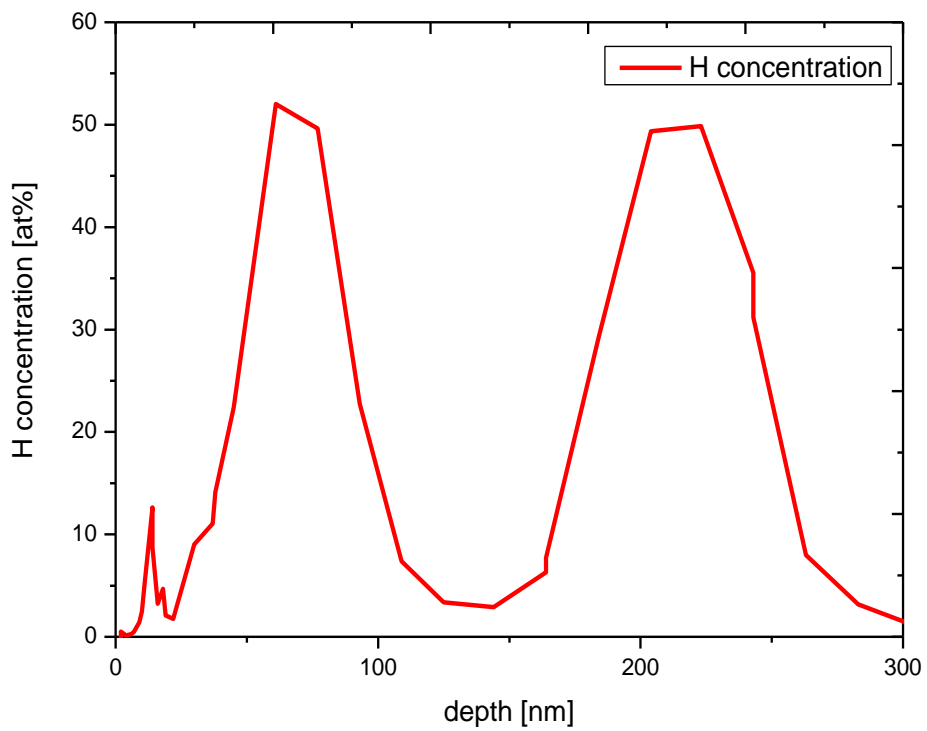
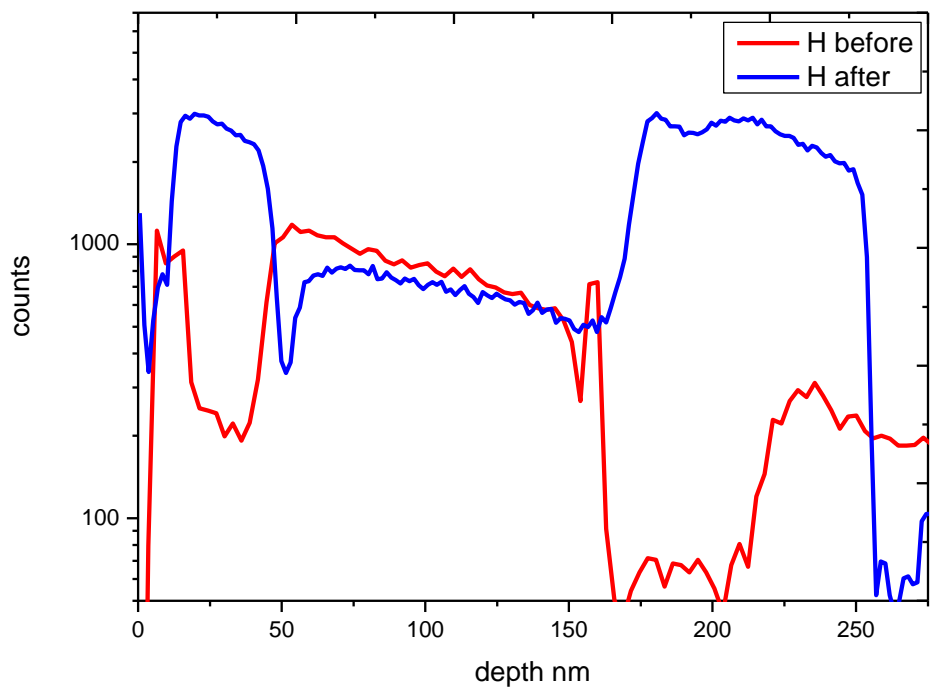


Figure 4.6. Comparison of H profiles for the sample covered with Pd, Pd/Ti/TiO₂/Ti/Si, measured by SIMS (top) and N-15 (bottom).

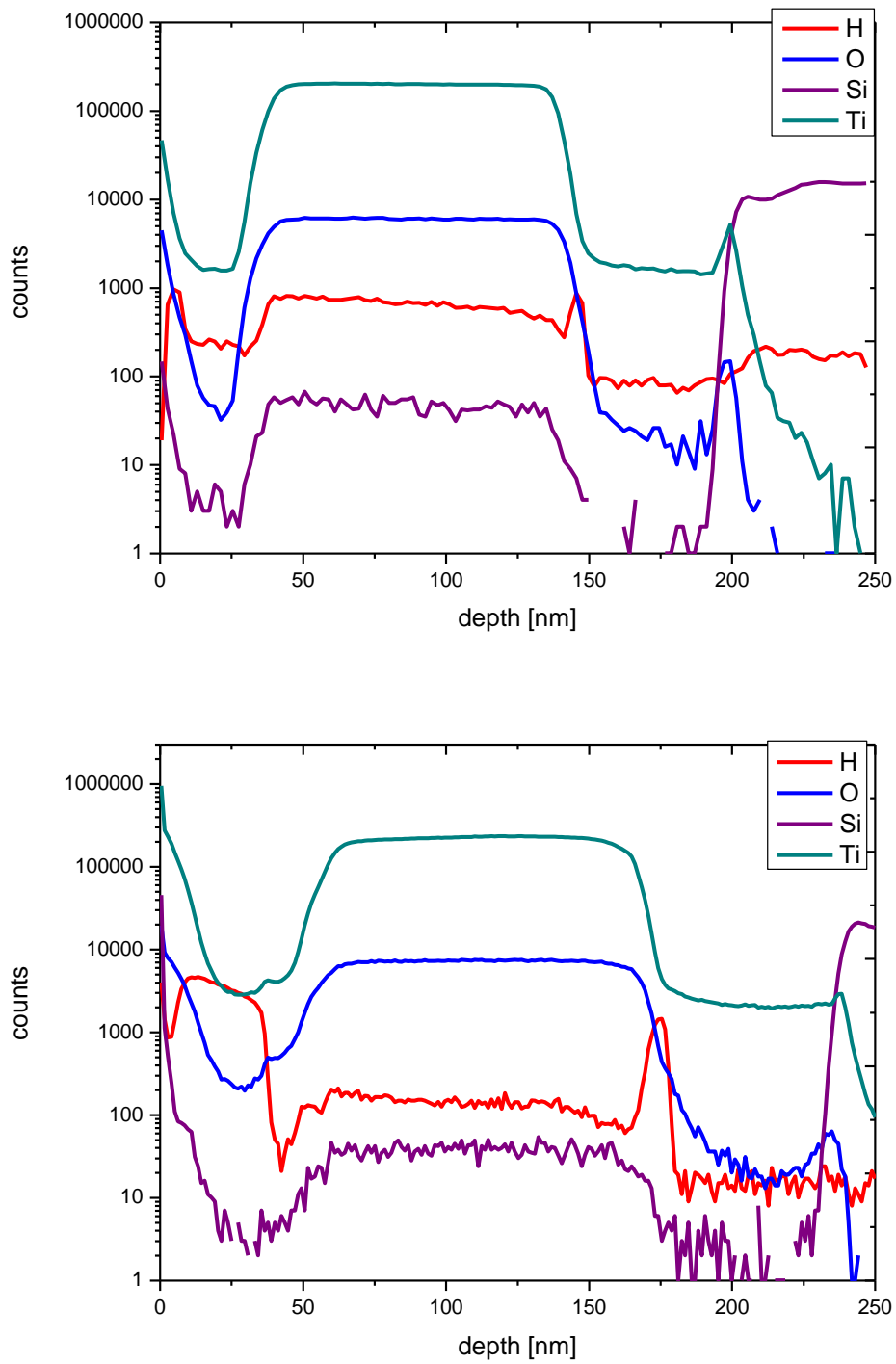


Figure 4.7. SIMS profiles for the sample without covering by Pd, Ti/TiO₂/Ti/Si, before (top) and after (bottom) hydrogen charging.

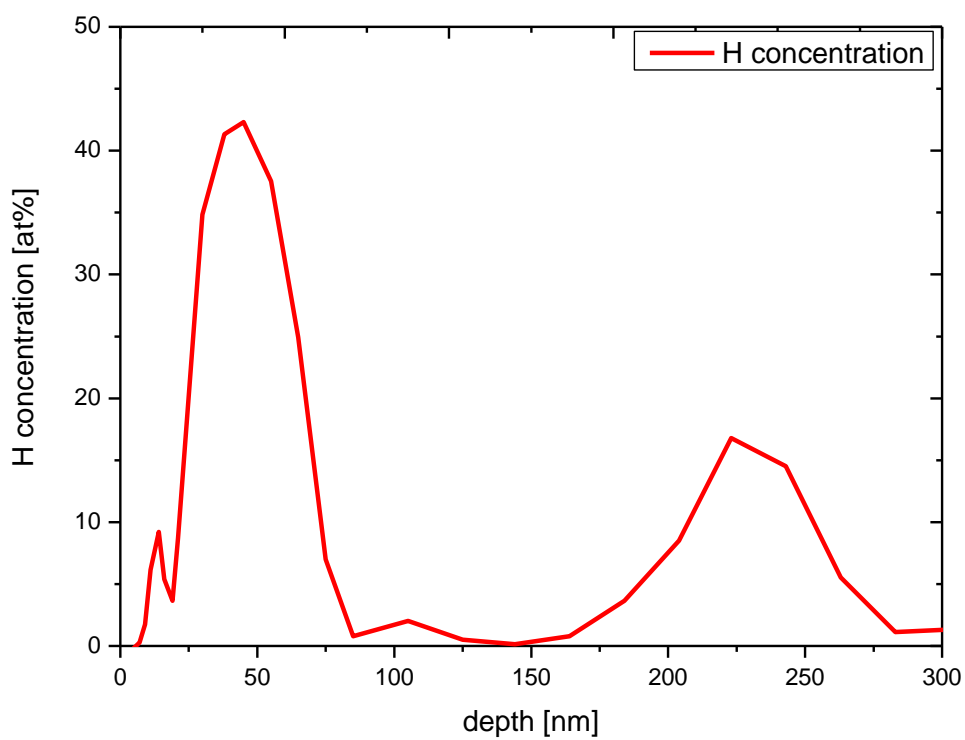
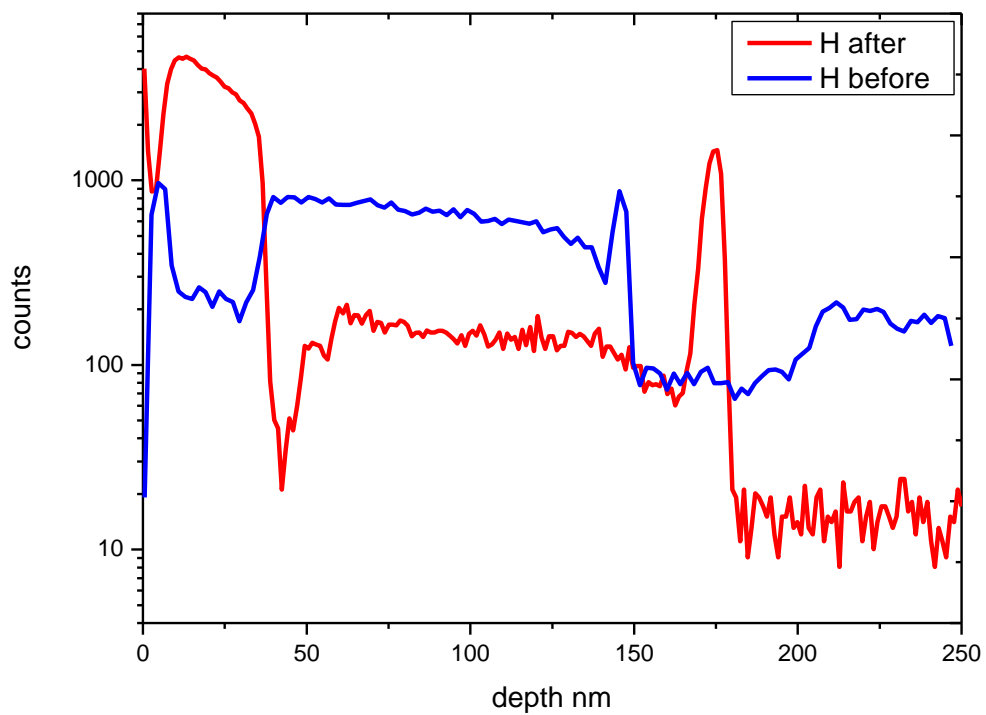


Figure 4.8. Hydrogen profiles for the sample without covering by Pd, Ti/TiO₂/Ti/Si, measured by SIMS (top) and by N-15 (bottom).

4.2 Hydrogenation of Ti-TiO₂ films at high pressure

4.2.1 Result and discussion

The hydrogenation at high pressures was performed on the single and tri-layer films; the S2, S3, D5 and T5 samples in Table 3.1. Fig. 4.9 (top) shows the XRR curves of the single layer S2 upon hydrogenation at two different hydrogen pressures. A quite reasonable fit to the experimental data was obtained. (The model of a single layer requires 5 fitting parameters among which the most important are its thickness and density as well as the interface roughness). The estimated value for the thickness was 67 nm in this case, a bit higher than the nominal thickness. The XRR results revealed that the layer-structure of the film is still very good upon hydrogenation at the pressure of H₂ gas of $p_{\text{H}_2} = 10$ bar. The periodicity of the XRR curve was similar to that of the as-deposited film. Increasing hydrogenation pressure to 100 bar leads to a disappearance of the periodicity of the XRR curve. A similar thickness was found for the hydrogenated film (S2) at 102 bar, indicating no visible swelling effect. However, hydrogenation causes an increase of the layer roughness. Namely, the roughness value (r) of 1.8 nm and 3.6 nm was estimated for the film after hydrogenation at respectively $p_{\text{H}_2} = 10$ bar and 102 bar. In other words, the sample after hydrogenation at 102 bar has got much rougher and thus it can explain why the Kiessig fringes in XRR have disappeared. We notice here that the film roughness of the as-deposited films was in the range of 1.0-1.3 nm [148] and no visible difference in the film roughness was found for the film upon hydrogen charging at 1 bar and at temperature $T = 300$ °C ($r = 1.1$ nm). Fig. 4.9 (bottom) shows XRD pattern of 67 nm Ti/Si(111) film (S2) after hydrogenation. For a comparison of the relative change in the peak intensity of different reflections, each XRD pattern was normalized so that the most intense diffraction line was set to 1 (the Ti(103) reflection for different films at 0 bar and at 10 bar and the Ti(002) reflection for these at 102 bar). Individual diffraction patterns were then shifted vertically with respect to each other. Similar to other studied single films, the intensity of all diffraction lines of the as-deposited film is very small except for the peak corresponding to (10.3) crystallographic plane. It confirmed a strong preferred orientation (with (00.1) plane parallel to the substrate) in the Ti layer. Hydrogenation at 10 bar, a large enhancement of the Ti(203) and Ti(110) peaks was observed with the intensity reaching respectively 60% and 40% with respect to that of the Ti(103) reflection. The diffraction peaks are rather broad ($>1^\circ$), in particular the Ti(203) one. A very similar XRD pattern was also observed for the thicker film (sample S3) of 240 nm Ti/Si(111) upon hydrogenation at the same condition. As pointed out earlier [148], the preferential orientation of Ti crystallites is not forced by the substrates and thus it would not be influenced by the film thickness. Increasing hydrogen pressure to 102 bar, many more Ti peaks appeared. Moreover, the Ti(002) peak becomes most intense; its intensity is two times larger than that of Ti(103). The results indicated that hydrogenation at high pressures ($p_{\text{H}_2} = 102$ bar) has destroyed the preferential orientation of the Ti film and thus the situation comes back to normal exhibiting standard XRD pattern. We notice here also that no peak-shift and no peak-widening were observed for any peak. It indicated that a large absorption of hydrogen in this thin Ti film ($d = 67$ nm) does not lead to any (visible) lattice expansion.

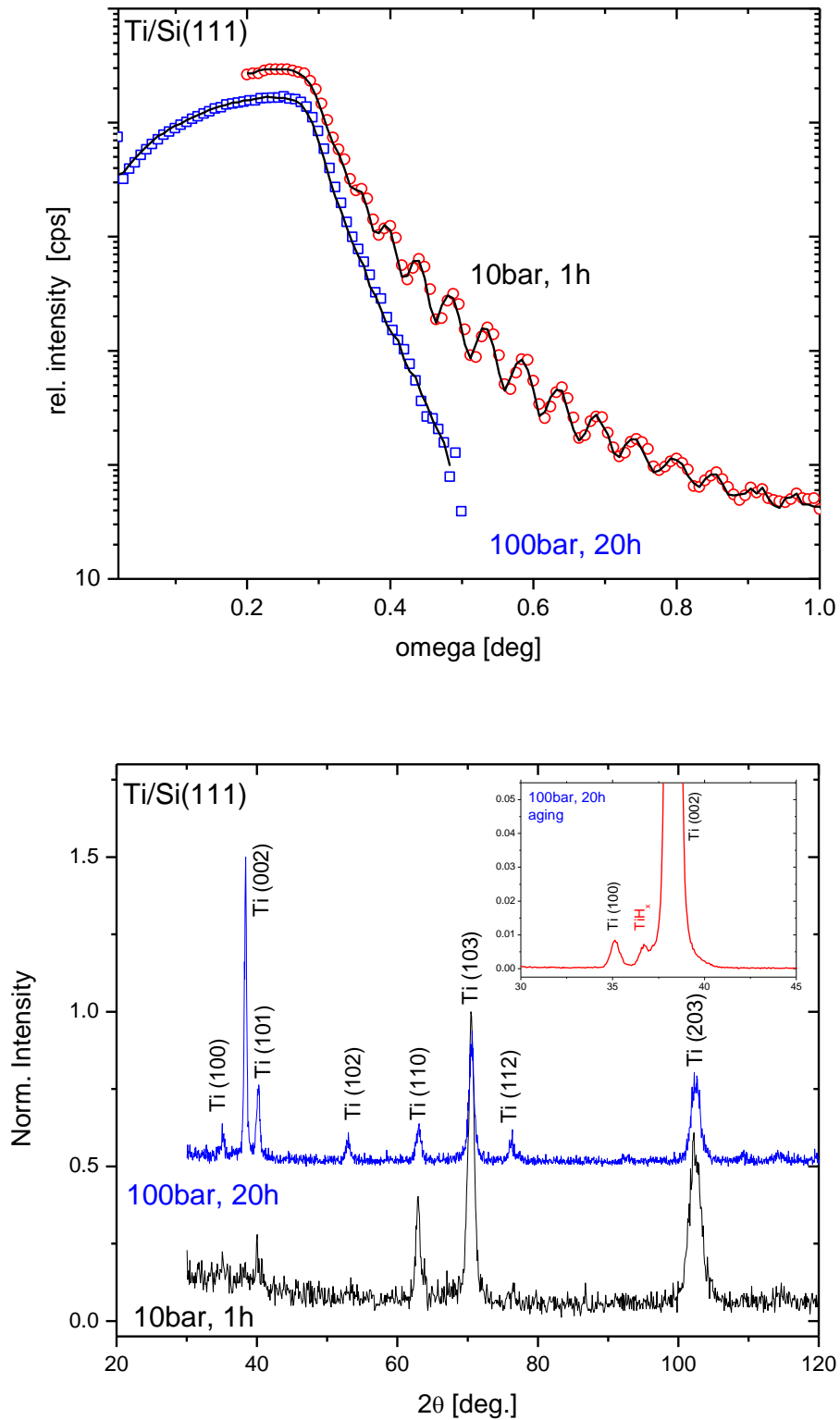


Figure 4.9. XRD pattern (top) and XRR curves (bottom) for 67 nm Ti/Si(111) film (sample S2) upon hydrogenation at 10 bar for 1 h and at 102 bar for 20 h and at room temperature. The curves were shifted to guide the eyes. Insert: the XRD pattern of the film after hydrogenation at 100 bar for 20 h performed on the film after 10 months revealing the TiH_x phase.

In other words, no visible swelling effect was observed. It is in a good agreement with XRR data (revealing a similar film thickness before and after hydrogenation). We remind here the disappearance of XRR periodicity of this thin film upon hydrogenation at 102 bar. It would be also consistent with XRD data revealing that the film becomes better crystallized and the crystallites become bigger and protrude from the surface causing the roughness increased. The titanium hydride phases TiH_x , e.g. titanium dihydride ($x = 2.0$), could be formed under such a high hydrogen pressure. However, the reflections of such hydride phases are very close to those of Ti. Therefore, we cannot rule out the existence of the TiH_x phases in the film. We have performed glancing incidence X-ray diffraction (GIXD) on this film. Very low intensity was seen in GIXD revealing a high texture of Ti in the film. The film after hydrogenation at 102 bar was re-measured after 10 months. It is very essential that we observed in this case the additional reflection located at $2\theta = 36.7^\circ$ contributed to TiH_x phase (with $x < 0.66$).

The RBS measurements were performed on these hydrogenated films, results are shown in Fig. 4.10. The RBS analysis for single thin Ti film (S2) confirmed that no swelling effect was observed, i.e. no visible change in the film thickness. However, for the hydrogenated film at 10 bar, we could easily fit the measured RBS spectra with one Ti layer and without any diffusion and without using the ‘roughness’ option from SIMNRA simulation. For the data at 102 bar, although from the width of the Ti peak, we could get a similar film-thickness, it was difficult to get a good overall fit even if with using (partially) the roughness option. We presented the data at 100 bar in the same Figure, just for pointing out that a similar peak width was observed for the Ti peak at both 10 bar and 102 bar. However, the small difference between two these films cannot be easily seen, except that the simulated spectrum is very well fitted to the data for the film at 10 bar for the whole energy range even if at low energy region, while the good fit was obtained for those at 102 bar only down to around 750 keV. We suggest that the reason is that the roughness is increased, as seen in XRR, and the thus film is far from ideal for RBS analysis. In other words, the RBS data also supported the XRR finding. No visible swelling effect from hydrogenation at 102 bar was observed for sample D5, since the film is still thin (with a total thickness of 75 nm). A large swelling effect was observed for the thick Ti film ($d = 240$ nm, sample S3). Surprisingly in this case, we could get easily a good simulated RBS fit even if after hydrogenation at 102 bar using just a single layer. The thickness value after hydrogenation at 10 bar is almost the same ($d = 240$ nm), but it amounts to 370 nm after hydrogenation at 102 bar, i.e. the thickness did increase by more than 150%. Increase of the layer thickness is related to increasing atomic volume due to crystal lattice expansion. Such behaviour for hydrogen charged metals have been already observed, e.g. for Nb [7].

The effect of hydrogenation on crystal structure of three-layer film (sample T5) was shown in Fig. 4.11. In the as-deposited state, unlike the single layer film, except of the intense Ti(103) reflection, the Ti(002) and Ti(101) were also observed. The appearance of Ti(002) reflection in the three-layer film was reported earlier [149]. Hydrogenation at $p_{\text{H}_2} = 102$ bar generally did not lead to a visible change of the XRD pattern except of the fact that all

reflections become more visible. Besides, the additional peak was observed at 54° contributed to the rutile phase, i.e. $\text{TiO}_2(211)$ reflection.

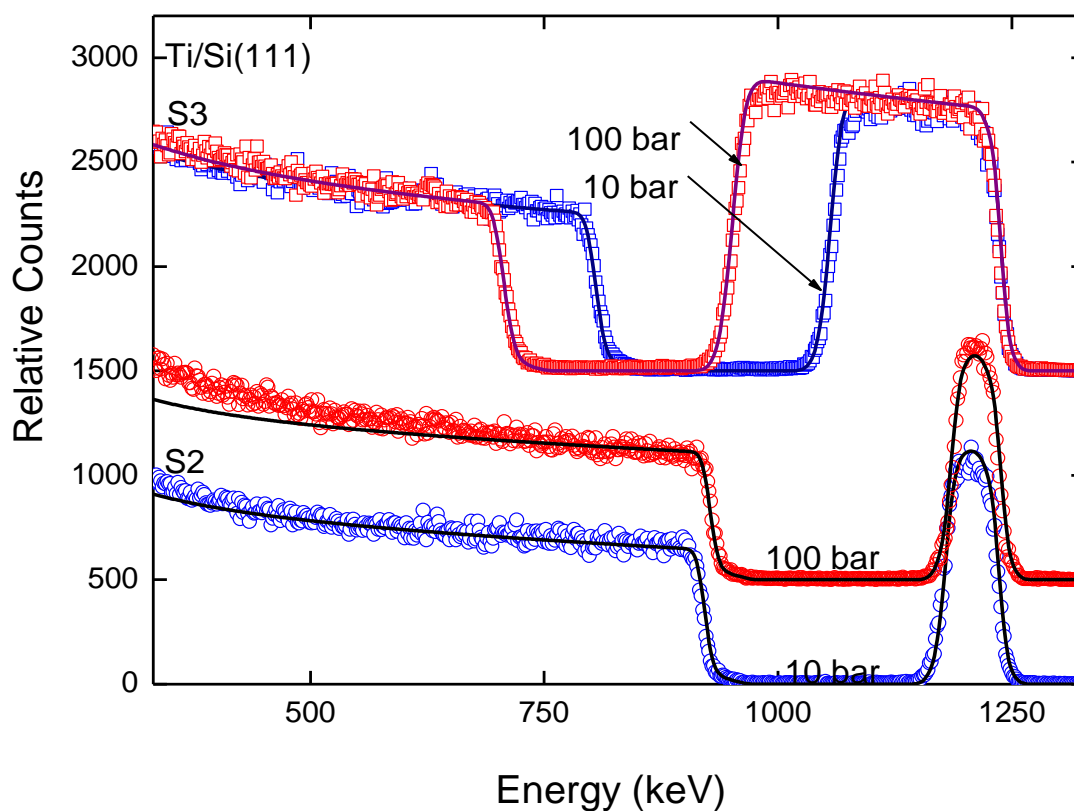


Figure 4.10. Random RBS (markers) and SIMNRA (lines) simulated spectra for hydrogenated single layer Ti/Si(111) films (S2, S3 in Table 3.1) at 10 bar and 102 bar. RBS experiments were performed with 1.7 MeV He^+ ion beam and the backscattering angle of 171° .

Since the total film thickness is only 95 nm in which the total thickness of Ti layers is only 35 nm, we did not expect to observe any swelling effect in this case. (The hydrogen can be stored in Ti layers but hardly stays in the TiO_2 layer). The RBS measurements indeed confirmed it. Namely, no change in the film thickness upon hydrogenation was revealed for such the tri-layer film.

4.2.2 Influence from hydrogenation to the film crystallinity

The main outcome of our investigations of numerous thin films of Ti-TiO₂ system with different film-geometry and layer thickness is summarized as follow:

The preferential orientation in the Ti films (with the *c*-axis of the hexagonal cell of Ti crystallites perpendicular to the substrate) was removed upon hydrogenation at high pressures ($p_{H_2}=102$ bar).

For the thin Ti films ($d < 100$ nm) or for the thick film ($d = 240$ nm) upon hydrogenation at 10 bar, the film thickness did not change much. A large swelling effect was observed for the thick Ti layer upon hydrogenation at 102 bar. The large hydrogen storage can make the film thickness increased by 150%.

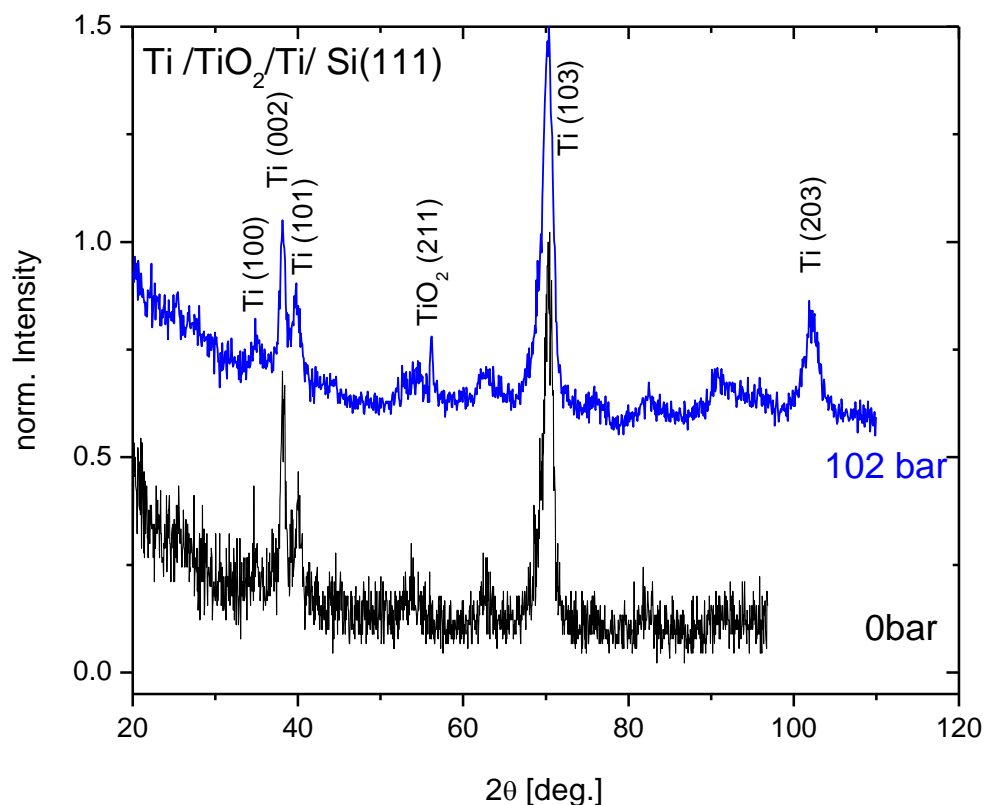


Figure 4.11. Comparison of X-ray diffraction pattern for tri-layer film Ti/TiO₂/Ti/ Si(111) (sample T5) after hydrogenation at 102 bar for 20 h with that before hydrogenation (as-deposited film). The curves were shifted to guide the eyes.

Chapter 5

Effect of hydrogen charging on the structure and physical properties of VO_x-TiO₂ thin films

As already mentioned in Chapter 1, due to oxygen reduction, the vanadium pentoxide V₂O₅ can be converted to vanadium dioxide VO₂. In this chapter we present the detail investigations of the influence of hydrogen on 5 different thin films consisted of TiO₂ and V₂O₅ layers deposited on silica SiO₂ substrates. For convenience, the films are denoted by their nominal chemical composition: V₂O₅/SiO₂ (denoted also as sample v1) and V₂O₅/TiO₂/SiO₂ (vt1), TiO₂/V₂O₅/SiO₂ (vt2 and vt3, with the same layer geometry but different thickness) and TiO₂+V/SiO₂ (v13).

The samples have been charged with hydrogen. Some samples was charged only once (denoted as H(1)), while some was charged twice (H(2)). Each hydrogen charging was carried out at pressure of 1 bar, at temperature of 300 °C and for 3 hours. RBS measurements were performed (with the incident He⁺ ion energy of 1.7 MeV and the backscattering angle of 171°) for every sample after each hydrogen charging.

5.1 The as-deposited VO_x-TiO₂ films

The measured and simulated RBS spectra for the 5 films deposited on silica SiO₂ substrates after deposition are shown in Fig. 5.1. Details of layer composition and thickness estimated from SIMNRA for each film are given in Table 5.1.

The RBS spectrum of V₂O₅/SiO₂ film (v1) was characterized by a large V-peak at energy around 1250 keV from the film, a steep Si- and O edge from the substrate respectively at 960 keV and 616 keV. Oxygen are consisted both in the film and in the substrate, thus there is no separated oxygen signal from the film, its contribution leads to some increase of the total oxygen signal on the left-hand, which side of the O-edge (i.e. below 616 keV) in the RBS spectra. A high non-zero background between the V-peak and Si-edge attributes to a diffusion of vanadium deeply into the SiO₂ substrate. The film geometry is described as following: 1/ the upmost surface layer of the film indeed consists of the most stable and common vanadium oxide V₂O₅ with a thickness of 13 nm (denoted as layer 1 of sample (v1) in Table 5.1), 2) beneath the V₂O₅ layer is the thick layer with a composition of V₂O_{5-x} (layer 2) with x increasing from 0 to 3.0 and thickness of 51 nm, 3) beneath the V₂O_{5-x} layer is the stoichiometric VO₂ layer with a thickness of 15 nm (layer 3) and then 4) a thick interface layer consisted of mixture of VO₂+SiO₂ was formed as a consequence of V diffusion into the SiO₂ substrate). A more detail analysis of the mixture layer V₂O_{5-x} (layer 2, thickness 51 nm)

indicates that it consists of two layers, the first one with a thickness of 24 nm (beneath the surface V_2O_5 layer (1)) is as a mixture of V_2O_5 , V_2O_7 (i.e. $x = 1.5$) and V_5O_9 ($x = 1.4$), while the second one (above the VO_2 layer (3)) with a thickness of 27 nm is a mixture of V_2O_3 layer ($x = 2.0$) and VO ($x = 3.0$). Our results indicates that during film deposition, first the VO_2 layer was formed (with an oxygen content of 33.3 at.%). With increasing deposition time, the oxygen content increases to a higher value to form the mixed V_2O_3+VO layer (with the oxygen content of 40-50 at.%). Increasing further the deposition time, the oxygen reduction leads to a layer with a complex mixture of V_2O_5 , V_2O_7 and V_5O_9 until the stable V_2O_5 (with the oxygen content of 28.6 at.%) is reached and formed on the film surface.

We notice here that in all cases, from the estimated value of metal (M) and oxygen (O) content by SIMNRA, the type of oxides consisted in the layer can be easily defined. For instance, the M and O content in M_2O_5 is respectively 28.6 at.% and 71.4 at.% , while it amounts respectively 33.3 at.% and 66.7 at.% for MO_2 . The SIMNRA fit for RBS spectrum is simulated for Nt product, i.e. the areal density (the number of target atoms per unit area). It is more convenient to have the estimated layer thickness in nm. The values of layer-thickness in [nm] are converted from the simulated RBS areal density values Y (in 10^{15} atoms/cm²) using the bulk density of different oxides (e.g. $\rho(TiO_2) = 4.23$ g/cm³, $\rho(VO_2) = 4.57$ g/cm³, $\rho(V_2O_5) = 3.36$ g/cm³) and estimated percentage (%) of each oxide presented in the layers. For instance, for the stoichiometric V_2O_5 layer (1) in sample vt1: $d(\text{nm}) = 0.1284 \cdot Y(10^{15} \text{ at./cm}^2)$, while for the mixed-oxide layer (2) in sample vt1 consisted of 85% TiO_2 , 9% VO_2 and 6% SiO_2 :

$$d(\text{nm})=[85\%(TiO_2) \cdot 0.1045 + 9\%(VO_2) \cdot 0.1004 + 6\%(SiO_2) \cdot 0.1505] \cdot Y(10^{15} \text{ at./cm}^2)$$

In most cases, the thickness could be estimated with a good accuracy, since the layer either consists of only stoichiometric oxide (such as TiO_2 , V_2O_5 , VO_2) or the mixture of oxides of the same type (such as (TiO_2+VO_2) or (VO_2+SiO_2) mixture). Even if for such a mixture, since the oxygen content is the same (66.7%), the percentage of different oxides can be easily estimated based on the ratio between different M components, e.g. $(\%) TiO_2 = (\%)Ti/33.3\%$ where $(\%)Ti$ is the estimated percentage of Ti in the layer and 33.3% amounts to the summation of percentage of all metal contents in the layer ($(\%)(Ti+V+Si)=33.3\%$). Some difficulty arises for the conversion of the simulated RBS areal density into the thickness in [nm] of the layer consisted of a mixture of different oxides, such as the layer (2) of sample v1 (V_2O_{5-x}). In this case, it is more difficult to estimate the exact ratio of different oxides based on only the ratio of M contents, since the O content is different for each oxide. We notice here that the real layer thickness of different layers would be somewhat different since the sputter deposited films may have some porosity or defects and thus the mass density of the film is certainly different than that of the bulk.

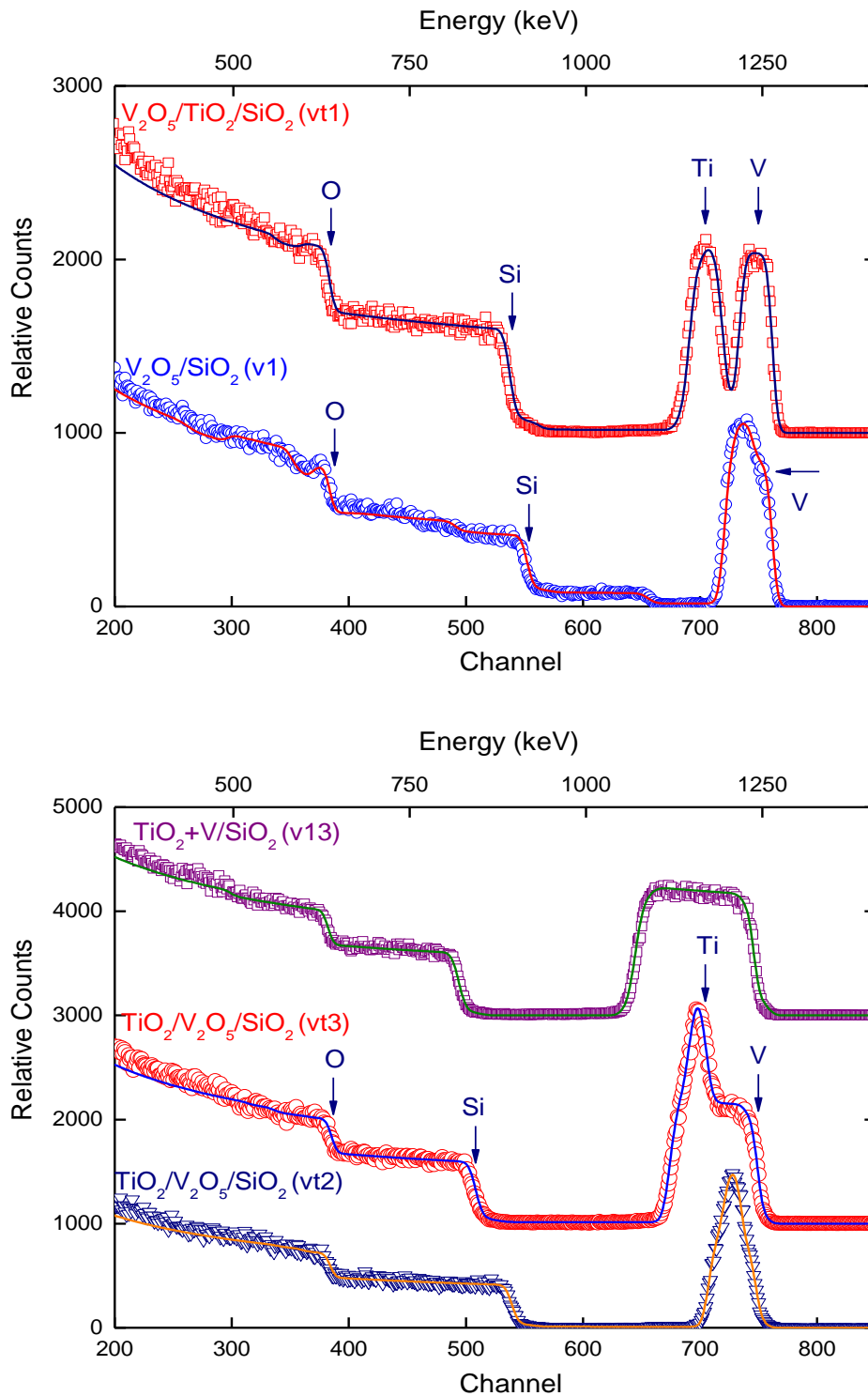


Figure 5.1. Random RBS (markers) and SIMNRA (lines) simulated spectra for (top) 79 nm V_2O_5/SiO_2 (sample v1) and 122 nm $V_2O_5/TiO_2/SiO_2$ (vt1) and (bottom) 117 nm $TiO_2/V_2O_5/SiO_2$ (vt2), 184 nm $TiO_2/V_2O_5/SiO_2$ (vt3) and 193 nm TiO_2+V/SiO_2 (v13) after deposition. RBS experiments were performed with the incident He^+ ion energy of 1.7 MeV and the backscattering angle of 171° . The film are denoted by its nominal chemical composition and the estimated total thickness. The curves were normalized and shifted for a better guide for the eyes.

	layer	V ₂ O ₅ (%)	TiO ₂ (%)	VO ₂ (%)	SiO ₂ (%)	<i>d</i> (nm)	<i>D</i> (nm)
V ₂ O ₅ /SiO ₂ (v1)	1	100				13	79
	2	100 (V ₂ O _{5-x})				51	
	3			100		15	

V ₂ O ₅ /TiO ₂ /SiO ₂ (vt1)	1	100				68	122
	2		85	9	6	54	

TiO ₂ /V ₂ O ₅ /SiO ₂ (vt2)	1		100			53	117
	2	100				64	

TiO ₂ /V ₂ O ₅ /SiO ₂ (vt3)	1		100			113	184
	2	100				71	

TiO ₂ +V/SiO ₂ (v13)	1		97	3		193	193
---	---	--	----	---	--	-----	-----

Table 5.1. Chemical composition of 5 films deposited on silica SiO₂ substrates after deposition (as-deposited films): V₂O₅/SiO₂ (denoted as sample v1), V₂O₅/TiO₂/SiO₂ (sample vt1), TiO₂/V₂O₅/SiO₂ (sample vt2 and vt3 with the same layer geometry but different thickness) and TiO₂+V/SiO₂ (sample v13). The layer-thickness of each layer (*d* (nm)), the percentage (%) of each type of oxides (TiO₂, V₂O₅, VO₂) presented in the film are estimated using SIMNRA and the mass density of the bulk (see text). Layer (1) denotes the surface layer. As a consequence of Ti, V and Si diffusion in the film-substrate interface the mixed MO₂ (M=Ti, V, Si) layer can appear.

The RBS spectrum of V₂O₅/TiO₂/SiO₂ film (vt1) was characterized by a large V-peak at an energy around 1250 keV and a large Ti-peak at an energy around 1200 keV from the film, a steep Si- and O edge from the substrate (at a lower energy than that for the v1 films since the film thickness is larger). The thickness of the V₂O₅ and TiO₂ layer are quite similar and so the V- and Ti-content in the film, thus a clear minimum between the V- and T-peak was observed. The TiO₂ was first deposited on the SiO₂ substrate and then the V₂O₅ layer was followed in this case. No stoichiometric TiO₂ was found. Instead, a mixed layer (TiO₂+VO₂+SiO₂) with a thickness of 54 was formed (layer 2, sample vt1) as a consequence from some Si diffusion (6% SiO₂) and V-diffusion (9% VO₂) into the TiO₂ film. However, the surface layer with a thickness of 68 nm consists of only stoichiometric V₂O₅.

In the case of two $\text{TiO}_2/\text{V}_2\text{O}_5/\text{SiO}_2$ films (vt2 and vt3), i.e. deposition sequence is first the vanadium and then the titanium oxide, our analysis reveals that each film consists of only stoichiometric V_2O_5 and TiO_2 layer. For the vt2 film, the thickness of TiO_2 (64 nm) and V_2O_5 layer (53 nm) is quite similar. Besides, the film is quite thin. Thus the V- and Ti- signal was combined into one large peak at around 1200 keV in the RBS spectrum. For the vt3 film, the thickness of TiO_2 layer is estimated to be 113 nm, while it equals to 71 nm for V_2O_5 layer (see Table 6.1). Both layers are thicker than those of vt2. Besides, the thickness of TiO_2 film is about 1.5 times larger than that of V_2O_5 one, i.e. the Ti content in the film is much larger. It leads to the wide shoulder (V-signal) and the large peak (Ti-signal) in the RBS spectra.

In the case of $\text{TiO}_2+\text{V}/\text{SiO}_2$ film (v13), the V content is estimated to be 1% for the entire film, i.e. the film composition is 97% $\text{TiO}_2+3\% \text{VO}_2$. Since the film is thick (193 nm), and since the V-content is very small, only a broad peak was observed in the RBS spectrum.

We notice here also, that during deposition, some V- or/and Ti was diffused deeply into the SiO_2 substrates implying a small non-zero background between the backscattered signals from the films and the Si-edge in the RBS spectra. Our analysis pointed out that the V- or/and Ti content is less than 0.2% for the last 4 films (vt1, vt2, vt3 and v13). The very high non-zero background observed for the first film (v1) is resulted from a much larger and deeper V-diffusion into the SiO_2 substrates forming a much larger interface region (mixture of VO_2+SiO_2). The reason is unknown for us, since we use almost the same deposition conditions for all those 5 films.

5.2 Effect of hydrogen charging on the $\text{VO}_x\text{-TiO}_2$ films

Comparison of the measured and simulated RBS spectra for the films before and after hydrogen charging are shown in Figs. 5.2 - 5.4. Details of layer composition and thickness estimated from SIMNRA for each film after each hydrogen charging are given in Table 5.2, i.e. the layer-thickness of each layer (d (nm)) converted from the SIMNRA areal density using the mass density of the bulk (mentioned above), the percentage (%) of each type of oxides (TiO_2 , V_2O_5 , VO_2) in each layer. The increased thickness of the film (%) due to hydrogenation was estimated for the total film thickness (D [nm]) with respect to that of as-deposited film ($= (D(\text{after}) - D(\text{before})) / D(\text{before charging})$).

For the $\text{V}_2\text{O}_5/\text{TiO}_2/\text{SiO}_2$ film (vt1), the Ti-peak and V-peak with almost equal intensity before hydrogen charging was observed (Fig. 5.2). The effect of hydrogen charging on this film is revealed by a lowering of the Ti-peak and a widening of this peak at the left-hand side. It is caused by a decrease of the percentage of TiO_2 in the layer 2, as well as an appearance of an extra mixed layer in the interface (see Table 5.2). The total film thickness is increased respectively by 7% and 15% after the first and second hydrogen charging. The thickness change is large enough in this case which can be revealed in the RBS spectrum.

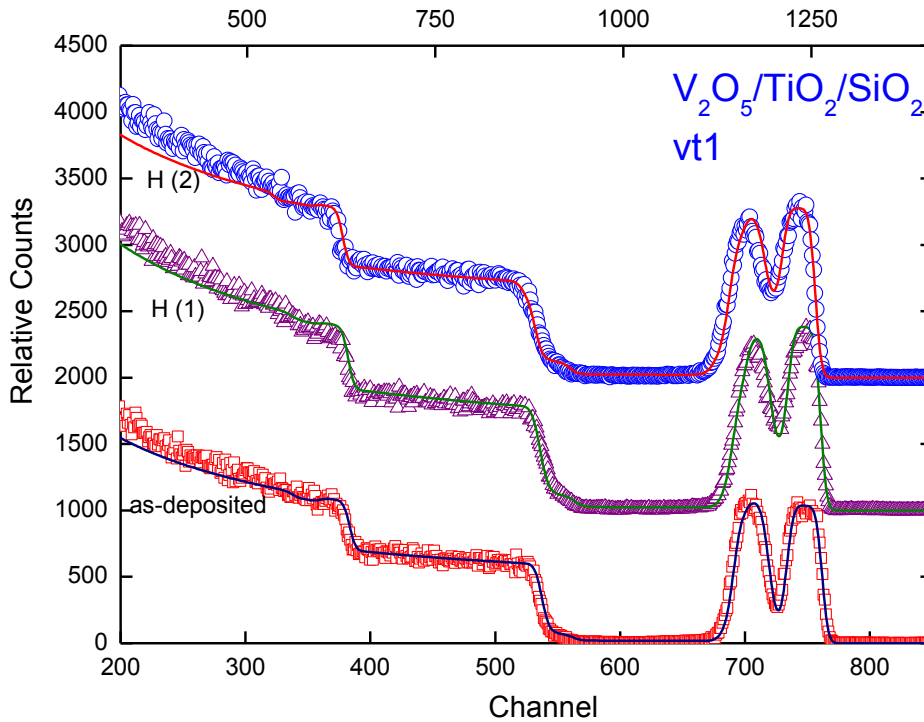


Figure 5.2. Random RBS (markers) and SIMNRA (lines) simulated spectra for $V_2O_5/TiO_2/SiO_2$ (vt1) before (as-deposited) and after two times of hydrogen charging (denoted respectively as H(1) and H(2)).

No clear effect can be seen in RBS spectra from hydrogen charging for the two $TiO_2/V_2O_5/SiO_2$ films (vt2 and vt3) and TiO_2+V/SiO_2 film (v13). Namely the RBS spectra before and after hydrogen charging are similar, as shown in Figs 5.3 and 5.4. The effect from hydrogen charging is mostly revealed by the change of the layer content and layer thickness, but the change in the total thickness is in the range of 2-3% for the vt2 and vt3 films. There is no change observed for the v13 film. Thus there is no visible change observed either for the peak-width or its shape in the RBS spectra.

We concentrate on analysing the most visible effect from hydrogen charging, i.e. on the $V_2O_5/TiO_2/SiO_2$ film (vt1). The hydrogen charging leads to a decrease of the layer thickness of the stoichiometric V_2O_5 layer-(layer 1) from 68 nm to 62 nm, while that of the mixed $TiO_2+VO_2+SiO_2$ layer - layer 2 increases from 54 nm to 56 nm after the first charging. The TiO_2 percentage in the layer 2 is only 62.5%, much lower than that before charging (85%). The VO_2 percentage increases from 9% to 26.5%. Besides, an extra layer with the same mixture as that layer 2 but with a lower percentage of TiO_2 (19%) and VO_2 (19%) and a higher percentage of SiO_2 (62%) does appear (with a thickness of 13 nm).

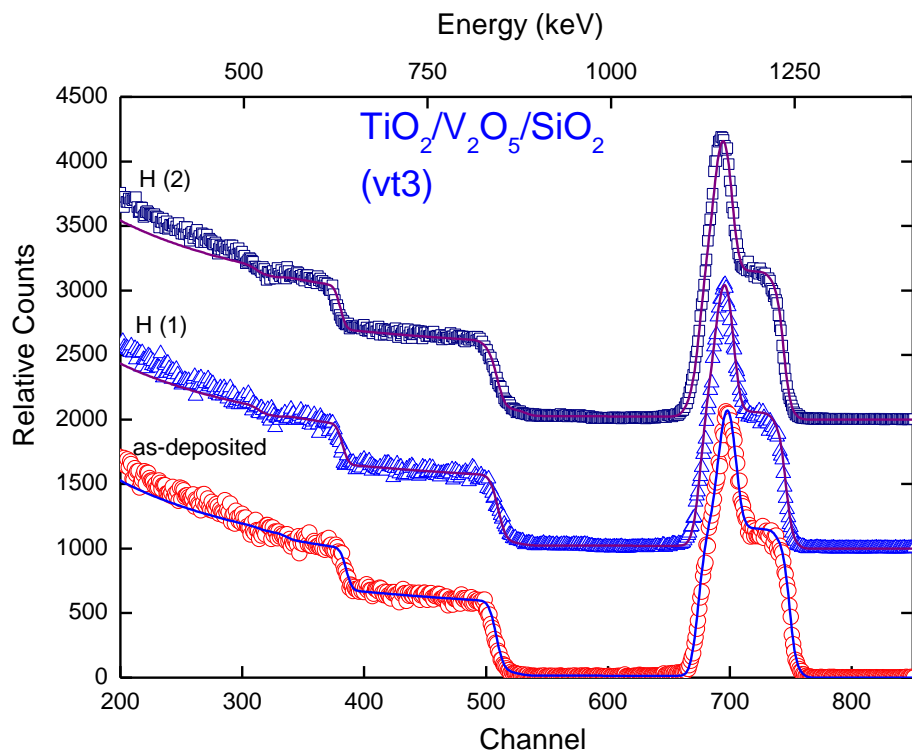
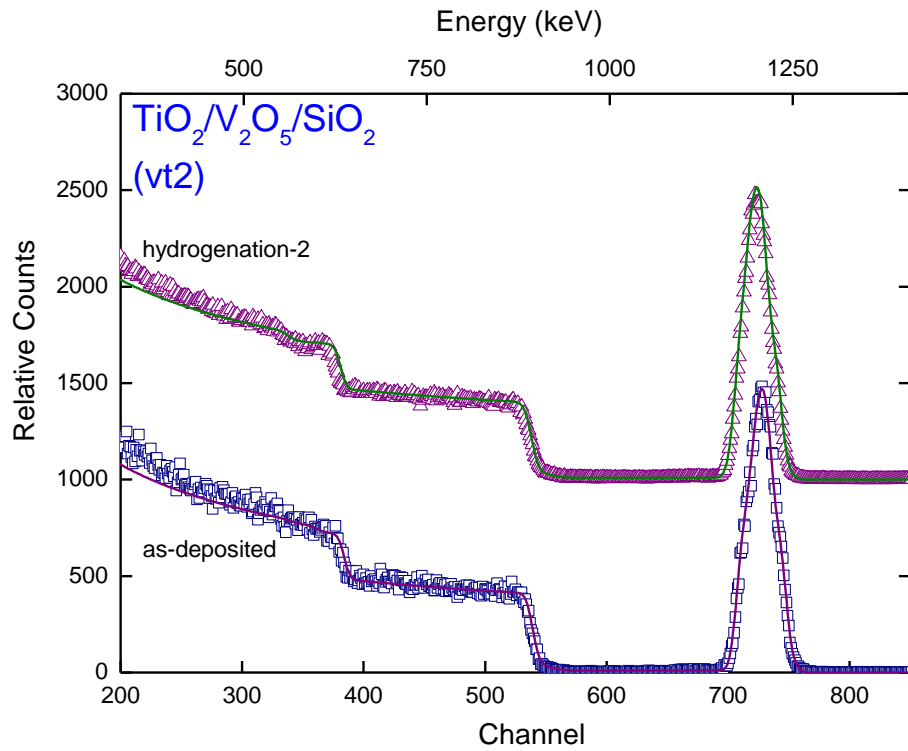


Figure 5.3. Random RBS (markers) and SIMNRA (lines) simulated spectra for (top) $\text{TiO}_2/\text{V}_2\text{O}_5/\text{SiO}_2$ (vt2) and (bottom) vt3 before (as-deposited) and after two times of hydrogen charging (denoted respectively as H(1) and H(2)).

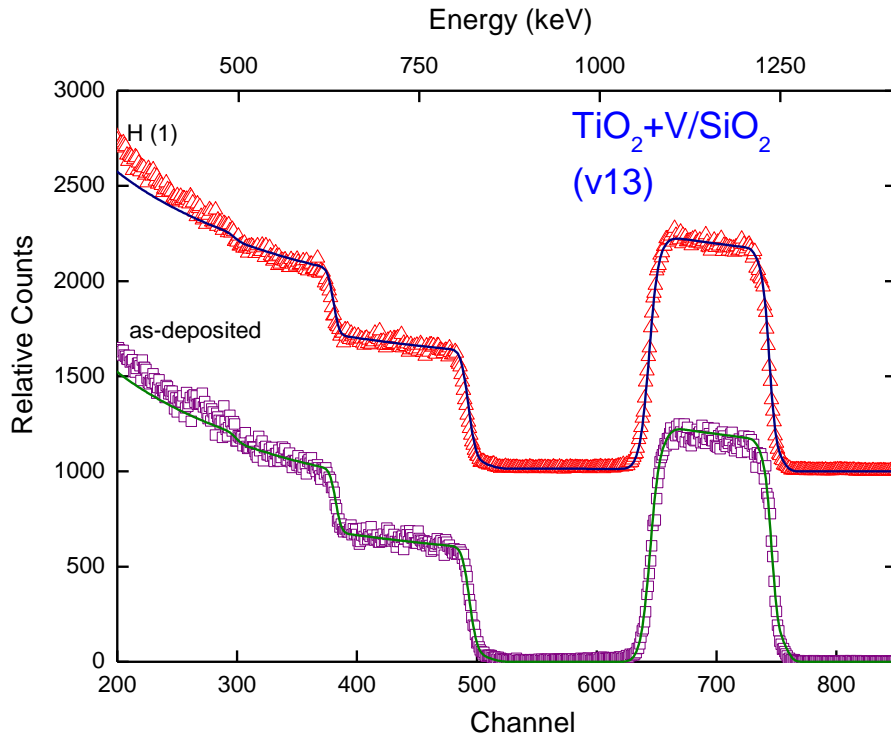


Figure 5.4. Random RBS (markers) and SIMNRA (lines) simulated spectra for $\text{TiO}_2+\text{V}/\text{SiO}_2$ (v13) before (as-deposited) and after hydrogen charging.

It can be explained as an enhancement of both Ti diffusion into the SiO_2 substrate and Si diffusion out from substrate into the film. We notice here that the film is heated up to 300°C for 3 hours during the first hydrogen charging. It certainly promotes such a diffusion and as a consequence increases the thickness of the interface layers. Indeed, the second hydrogen charging induces a larger enhancement; the percentage of SiO_2 in the interface layers is largely enhanced and reached even 75%. The total film thickness is found to be increased by 7% and 15% after the first and the second hydrogen charging. Our results clearly show the transition from V_2O_5 to VO_2 , or in other words, a reduction of V_2O_5 and increase of VO_2 concentration due to hydrogen charging.

We did not construct the depth profile from the RBS data, i.e. the concentration of each element as a function of the film thickness, just because the relative change between different layers is quite small. For a better presentation of the hydrogen effect, we construct the film diagram, where the layer thicknesses of different layers are drawn proportionally with respect to the values given in Table 5.2.

V ₂ O ₅ /TiO ₂ /SiO ₂ (vt1)	layer	V ₂ O ₅ (%)	TiO ₂ (%)	VO ₂ (%)	SiO ₂ (%)	<i>d</i> (nm)	<i>D</i> (nm)	Increased thickness
as-deposited	1	100				68	122	
	2		85	9	6	54		
hydrogenation-1 H (1)	1	100				62	131	7%
	2		62.5	26.5	11	56		
	3		19	19	62	13		
hydrogenation-2 H (2)	1	100				62	140	15%
	2		48	36	16	37		
	3		7	18	75	41		

TiO ₂ /V ₂ O ₅ /SiO ₂ (vt2)	layer	V ₂ O ₅ (%)	TiO ₂ (%)	VO ₂ (%)	SiO ₂ (%)	<i>d</i> (nm)	<i>D</i> (nm)	Increased thickness
as-deposited	1		100			53	117	
	2	100				64		
hydrogenation-2 H (2)	1		100			53	121	3%
	2			100		54		
	3			18	82	14		

TiO ₂ /V ₂ O ₅ /SiO ₂ (vt3)	layer	V ₂ O ₅ (%)	TiO ₂ (%)	VO ₂ (%)	SiO ₂ (%)	<i>d</i> (nm)	<i>D</i> (nm)	Increased thickness
as-deposited	1		100			113	184	
	2	100				71		
hydrogenation-1 H (1)	1		100			112	184	0%
	2	100				58		
	3			15	85	14		
hydrogenation-2 H (2)	1		100			111	187	2%
	2			94	6	47		
	3			15	85	29		

Table 5.2. Effect of hydrogenation on 3 films deposited on silica SiO₂ substrates: V₂O₅/TiO₂/SiO₂ (sample vt1), TiO₂/V₂O₅/SiO₂ (sample vt2 and vt3 with the same layer geometry but different thickness). No effect was observed for TiO₂+V/SiO₂ film (vt13). The layer-thickness of each layer (*d* (nm)), the percentage (%) of each type of oxides (TiO₂, V₂O₅, VO₂) presented in the film were estimated using SIMNRA and the mass density of the bulk (see text). Layer (1) denotes the surface layer. As a consequence of Si diffusion from the SiO₂ substrate into the film, in the film-substrate interface the mixed TiO₂-VO₂-SiO₂ layer did appear. The increased thickness of the film (%) due to hydrogenation was estimated for the total film thickness (*D* (nm)) with respect to that of as-deposited film.

Different compositions of different oxides in the layers are presented by using different colours. The film diagram was shown for vt1, vt2 and vt3 films in Figs 5.5 and 5.6 respectively, since the hydrogen charging leads to the change of layer thickness and composition in these cases. Neither any change of the film thickness nor the film composition was revealed for the v13 film upon hydrogen charging. The film composition is estimated to be consisted of 97% of TiO_2 and 3% of VO_2 with a total thickness of 193 nm, both before and after hydrogen charging. Thus no diagram was shown for this film.

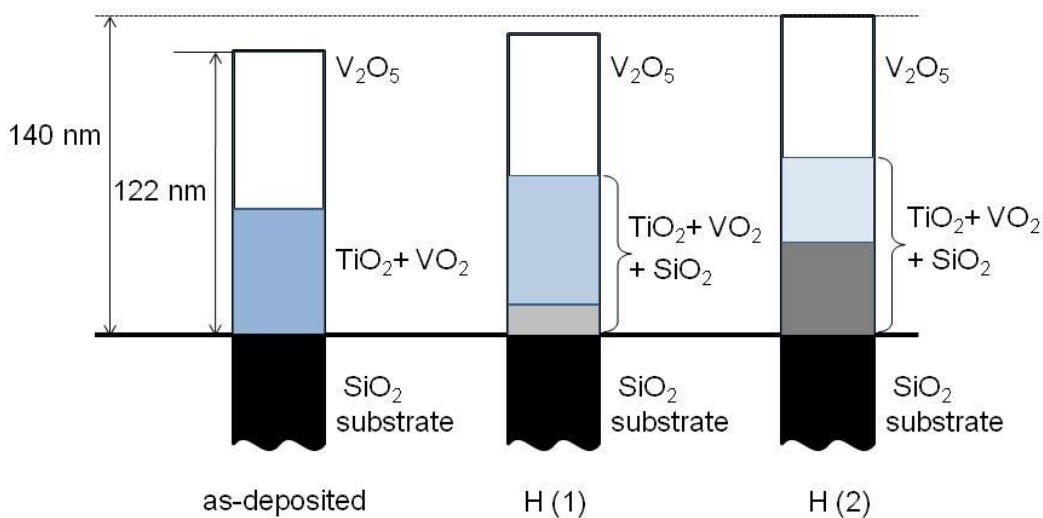


Figure 5.5. Illustration of the influence of hydrogenation on the structure and composition of $\text{V}_2\text{O}_5/\text{TiO}_2/\text{SiO}_2$ (vt1). The layer thicknesses are drawn proportionally with respect to the values given in Table 6.2. The solid line indicates the original separation between the film and the SiO_2 substrate. Different colours indicate different compositions of different oxides (TiO_2 , VO_2 , SiO_2) in the layers. The dashed line reveals the film thickness after two times of hydrogenation with respect to that of the as-deposited film (thin solid line). The estimated total film thickness before and after hydrogenation was also given.

The effect from hydrogen charging on $\text{VO}_x\text{-TiO}_2$ films is summarized as following:

- 1/ The V_2O_5 reduction is always observed for 3 films with bi-layer geometry, i.e. $\text{V}_2\text{O}_5/\text{TiO}_2/\text{SiO}_2$ and $\text{TiO}_2/\text{V}_2\text{O}_5/\text{SiO}_2$ films. In all cases the thickness of the V_2O_5 layer decreases upon hydrogen charging,
- 2/ In the case if the surface layer is the V_2O_5 layer, the hydrogen charging effect is much enhanced shown by a large increase of the total film thickness (up to 15% upon hydrogen charging of 6 hours) mostly related to a large increase of the thickness of the mixed ($\text{TiO}_2+\text{VO}_2+\text{SiO}_2$) layer.

3/ In the case if the surface layer is the TiO_2 layer, the film thickness does not change much (up to 2-3% only) upon hydrogen charging.

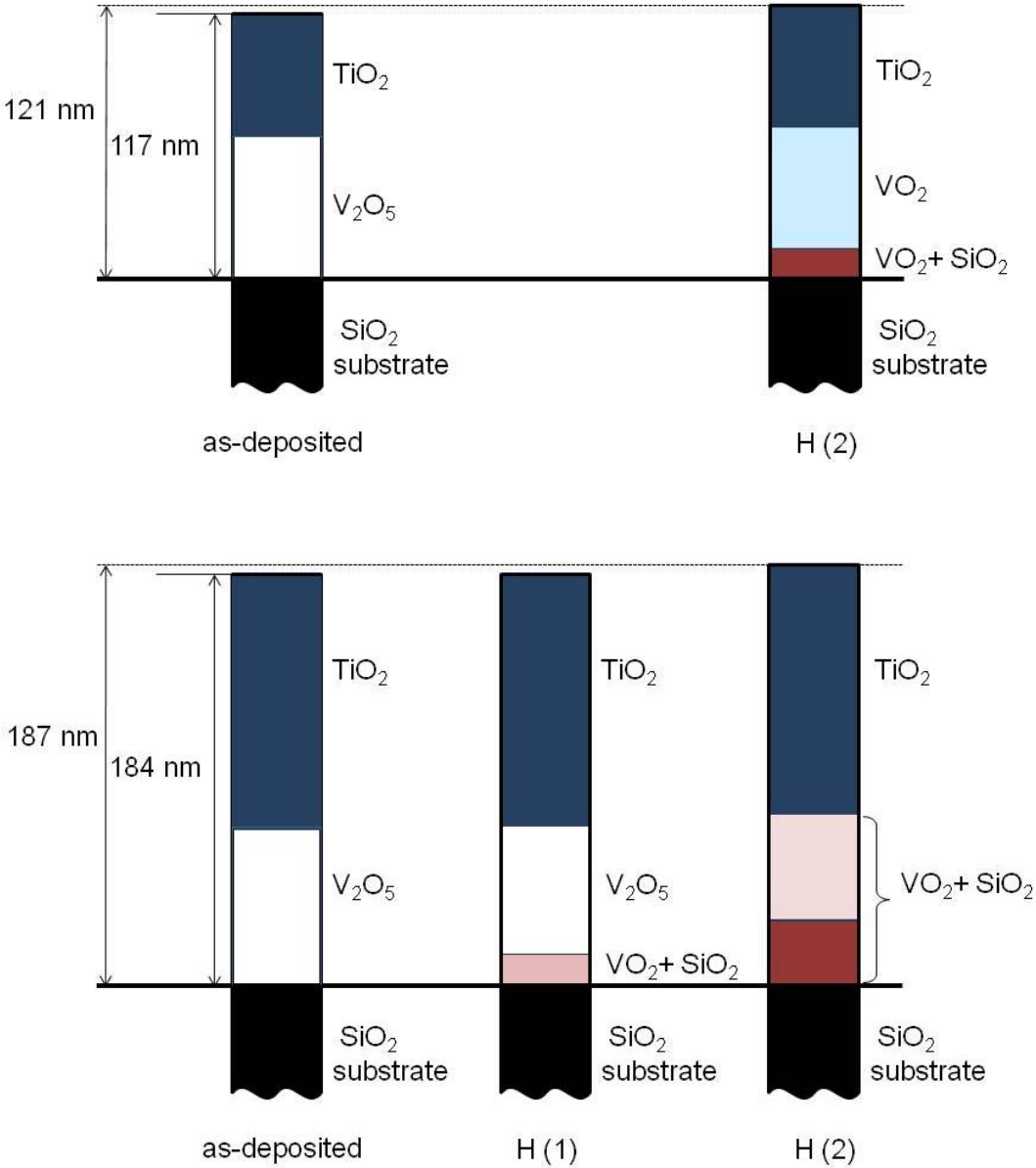


Figure 5.6. Illustration of the influence of hydrogenation effect on the structure and composition of 2 films with similar layer geometry $\text{TiO}_2/\text{V}_2\text{O}_5/\text{SiO}_2$ but with different thickness (vt2 (top), vt3 (bottom)). The layer thicknesses are drawn proportionally with respect to the values given in Table 5.2. The solid line indicates the original separation between the film and the SiO_2 substrate. Different colours indicate different compositions of different oxides (VO_2 , SiO_2) in the layers. The dashed line reveals the film thickness after two times of hydrogenation with respect to that of the as-deposited film (thin solid line). The estimated total film thickness before and after hydrogenation is also given.

However, a larger reduction of V_2O_5 is observed. Namely, after 6 hours charging, a complete transition of V_2O_5 into VO_2 was obtained. It indicates that the TiO_2 layer acts as 'hydrogen catalyst' for such the V_2O_5 - VO_2 transition.

Our study of Ti - TiO_2 multilayers (Chapter 3) have revealed that hydrogen can diffuse through open channels along the TiO_2 *c*-axis in TiO_2 layer without any accumulation there. On one hand, the hydrogen can be transferred to the V_2O_5 layer though the TiO_2 layer, on the other hand such the V_2O_5 layer is deposited directly on SiO_2 substrates (possessing a lot of oxygen) for the case of $TiO_2/V_2O_5/SiO_2$ films. Both help the V_2O_5 - VO_2 transition completed. But it seems the hydrogen is not stored in the film, when there is no expansion of the lattice observed (when a very small increase of the film thickness is observed).

The V_2O_5 can be well preserved upon hydrogen charging if it locates on the film surface, as in the case of $V_2O_5/TiO_2/SiO_2$ film. Besides, the visible increase of the film thickness (up to 15%) can attribute to a large expansion of the lattice and may indicate a large hydrogen storage in the film.

Our conclusion is supported by the results obtained for $TiO_2 +V/SiO_2$ film (v13). No change was observed indicating that no hydrogen is accumulated in TiO_2 even if it is doped with vanadium. However, in this case, since the V-doping is very small (1%) and the film is thick, VO_2 (3%) exists in the film. Thus there is no possibility to observe the V_2O_5 - VO_2 transition.

5.3 Hydrogen profile of $TiO_2/V_2O_5/SiO_2$ film

N-15 experiments have been performed on $TiO_2/V_2O_5/SiO_2$ film to determine the hydrogen content in different layers upon hydrogen charging, as shown in Fig. 5.7. The N-15 results are in a good agreement with the RBS analysis. Namely, the hydrogen diffuse through the TiO_2 and does not accumulate there indicated by a very low hydrogen content in the hydrogen profile in the thickness range down to about 100 nm with respect to the film surface, i.e. the thickness of TiO_2 layer. The hydrogen reaches an average value of about 15% in the thickness range of 100-200 nm. In other words hydrogen is accumulated in the V_2O_5 or mixed VO_2+SiO_2 layer.

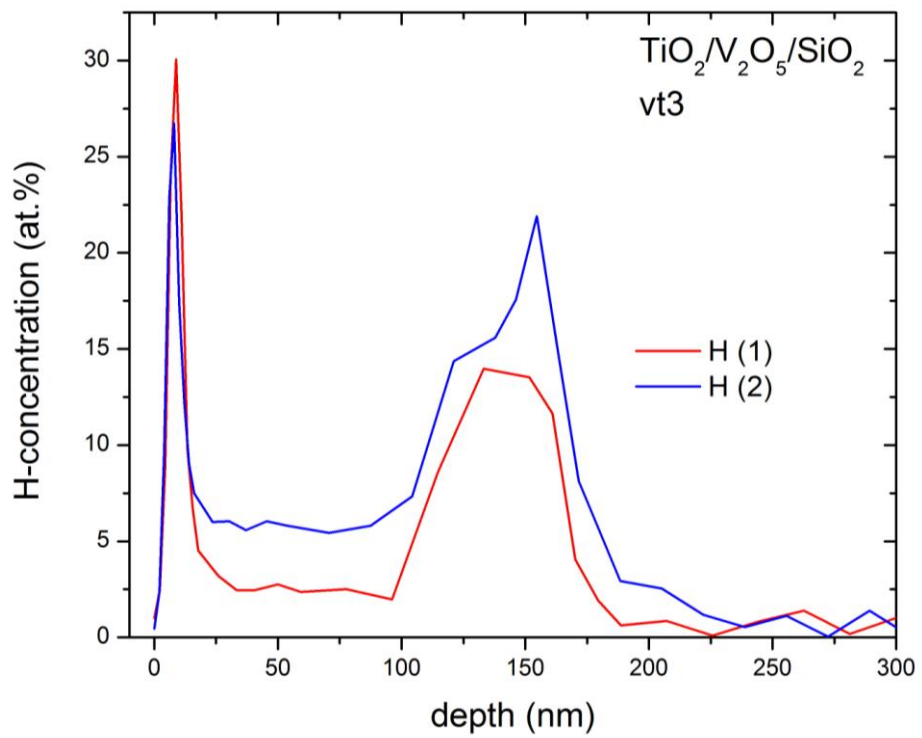


Figure 5.7. The hydrogen profile determined from N-15 experiments for $\text{TiO}_2/\text{V}_2\text{O}_5/\text{SiO}_2$ film upon hydrogen charging.

Chapter 6

Hydrogen storage in Ti-V-Ni films

As shown in Chapter 3, 4 and 5, Ti-TiO₂ and TiO₂-VO_x systems can absorb and store a large amount of hydrogen. In order to get a deeper understanding of the hydrogen absorption capacity, we extend our investigations to other thin film system consisted of Ti, V as well as of Ni.

We have prepared the Ti-V-Ni thin films deposited on Si and SiO₂ substrates by sputtering, i.e. Ti-V-Ni/Si(111) (denoted also as kdv5 sample) and Ti-V-Si/SiO₂ (kdv2). Vanadium and Nickel plates were placed on Titanium target to obtain Ti:V:Ni ratio of 1:1:1 and 0.6: 0.1: 0.3 respectively for kdv5 and kdv2 sample. Sputtering time of 180 s was acquired to obtain the film with a thickness of 150 nm. The exact composition and thickness were determined by means of RBS. Both two samples were charged with hydrogen at 1 bar and at 300 °C for 3 hours. The hydrogen profiles have been obtained by N-15 method.

6.1. Layer composition and the thickness of the Ti-V-Ni films

Figs 6.1 and 6.2 show the measured and simulated RBS spectra for the Ti-V-Ni films before and after hydrogen charging. Details of layer composition and thickness estimated from SIMNRA for each layer of each film are given in Table 6.1. The RBS spectrum of as-deposited Ti-V-Si/Si(111) film (Fig. 6.1) is characterized by a large and wide peak at energy range of 1050 and 1300 keV corresponded to Ti-, V- and Ni signals from the film. The energy of He⁺ ions backscattered from a binary collision with the Ti-, V- and Ni atoms in the films are denoted as Ni(f), V(f) and Ti(f) in the figure. The composition of each element is quite similar in the film: 36 wt% Ti, 34 wt% V and 30 wt% Ni, or Ti₃₆V₃₄Ni₃₀/Si(111). Besides, the molar mass of such 3 elements are very close to each other ($m(\text{Ni}) = 58.7$ g, $m(\text{V}) = 50.9$ g, $m(\text{Ti}) = 47.8$ g). Thus the ‘combined’ signals from those 3 elements formed the wide peak with some fine structures (e.g. 2 small peaks at the two sides of a wide peak located around 1200 keV). For such a sample, the Si-edge from the Si substrate locates at energy around 850 keV (Si(sub.)).

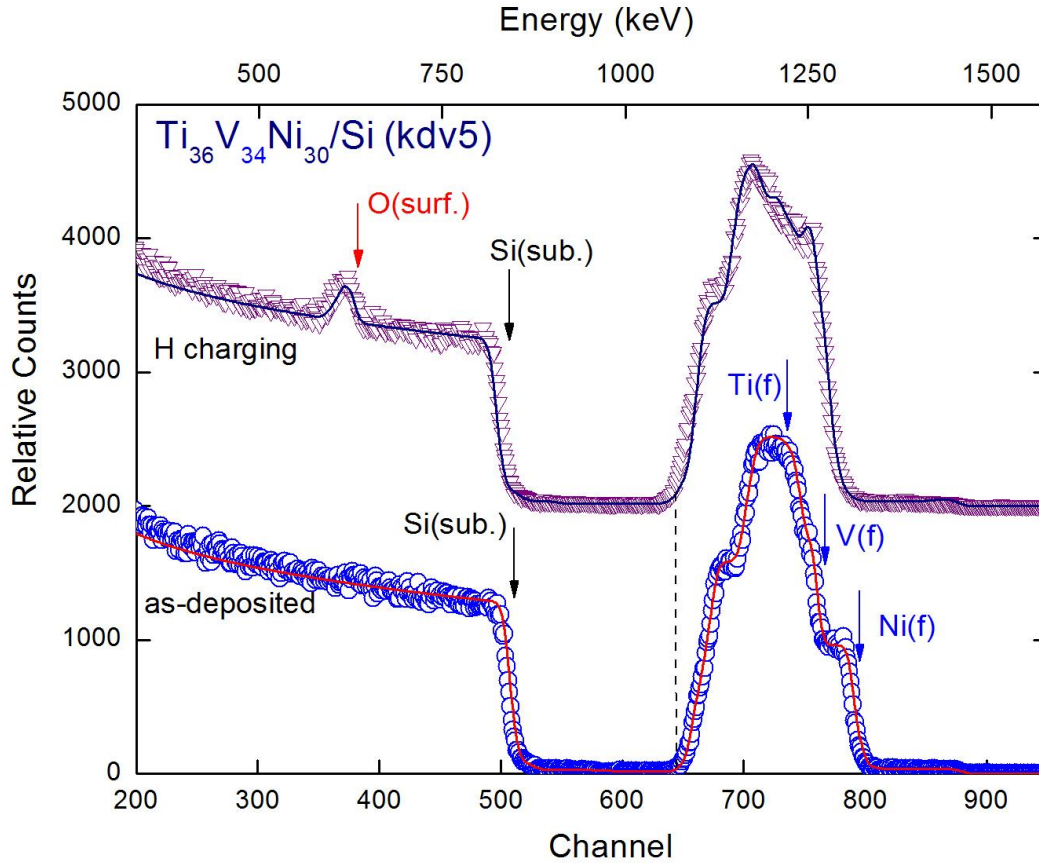


Figure 6.1. Random RBS (markers) and SIMNRA (lines) simulated spectra for 151 nm $\text{Ti}_{36}\text{V}_{34}\text{Ni}_{30}/\text{Si}(111)$ (sample kdv5) before and after hydrogen charging. RBS experiments were performed with the incident He^+ ion energy of 1.7 MeV and the backscattering angle of 171° . The film is denoted by its nominal chemical composition in the as-deposited state. The curves were normalized and shifted for a clarity. Ni(f), V(f) and Ti(f) denoted respectively the Ni-, V- and Ti signal in the film. The Si signal from the Si substrate is labeled as Si(sub.). The surface oxidation is revealed by an appearance of oxygen signal (O(surf.)). The vertical dotted line indicates that the film thickness (or the peak width) does not change upon hydrogenation.

Hydrogen charging leads to surface oxidation of the film revealed by an appearance of a quite sharp O-peak at energy of 620 keV. The film structure can be considered to consist of 2 different regions: 1) the surface oxidized layer with a total thickness of 48 nm, 2) the main part of the film is the pure metal layers of a total thickness of 103 nm. Our detailed analysis indicates that on the surface there is the fully oxidized layer with a thickness of 29 nm (layer 1) consisted of 88% TiO_2 + 9% VO_2 + 4% NiO_2 (see Table 6.1). Beneath it is the mixed layer (layer 2) of oxides and pure metals of approx. 14% $(\text{Ti,V,Ni})\text{O}_2$ + 86% (Ti,V,Ni) with a thickness of 19 nm. In the pure metal layer (103 nm), the element content was changed in different sub-layers (layer 3-5). Namely the Ti and Ni content decreases respectively from 21

to 10 at.% and from 64 to 35 at.%, while the V-content increases from 15 to 50 at.%. A surprising fact is that the total thickness of the Ti-V-Ni/Si(111) film does not change by hydrogen charging. Despite of the change of the peak-shape related to some re-arrangement of the metal atoms in the films (revealed by the composition change in different sub-layers), the peak-width in the RBS spectra is similar for both as-deposited film and that after hydrogen charging. It was illustrated by the vertical dotted-line in the figure: the Ti-V-Ni peak ends at the same energy value.

We notice here that the hydrogen charging has been carried out at 300 °C for a quite long time (of 3 hours). The significant change of the element-ratio upon hydrogen charging, in our opinion, is rather related to the diffusion process at elevate temperatures. Different elements would have different diffusion efficiency. A highest Ni concentration was found on the top sub-layer of the pure metal layer (64 at.%). In the deeper parts of the film, nickel concentration did not change (35 at.%). The interdiffusion is found between Ti and V, in which the top sub-layer (layer 3) consists of more Ti (21 at.%) and less V(15 at.%) while for the bottom sublayer (layer 5, located directly on the Si substrate) it is opposite, i.e. it consists of less Ti (10 at.%) and more V (50 at.%).

The RBS spectrum of as-deposited Ti-V-Si/SiO₂ film (Fig. 6.2) is quite similar to that of Ti-V-Si/Si(111) film, i.e. with a wide peak at energy range of 1050 and 1300 keV corresponded to the Ti-, V- and Ni signal from the film (Ni(f), V(f) and Ti(f)) and the Si-edge from the Si substrate locates at energy around 850 keV (Si(sub.)). However, in this case, the oxygen signal from the substrate implies the oxygen edge (O(sub.)) at energy of 500 keV located on the Si-plateau (from Si substrate).

After hydrogen charging, the film surface was found to be oxidized. Our analysis indicates that there is no longer any pure metal in this case. The oxygen signal from the entire oxidized film and from the SiO₂ substrate leads to some fine structure in the RBS spectrum between 400 keV and 700 keV: the broader O-peak from the film (O(f)) and the smoother O-edge from the substrate. The film structure after hydrogen charging can be divided into 3 main regions, on the surface is the entire oxidized layer (with a thickness of 47 nm), the mixed oxide and metal layer (81 nm) and the interface layer as a mixed layer consisted of pure metals and SiO₂ (82 nm). The topmost surface layer (layer 1) consists of 88% TiO₂ + 12% NiO₂, i.e. vanadium diffuses deeply into the film and is not present on the surface layer (see Table 6.1). The second layer beneath the surface (layer 2) consists of approximately 38% TiO₂ + 45% VO₂ + 17% NiO₂. Beneath the oxide layer, there is the mixed layer of oxide and pure metals (Ti,V,Ni)O₂ + (Ti,V,Ni) with the percentage of the oxides decreases from 75% (layer 3) to 30% (layer 4). Although the percentage of metals further increases in deeper layer (85%, layer 5), due to Si and O diffusion out of the substrate into the film, the metal percentage again decreases in the deeper layer (78%, layer 6). As a result of both surface oxidization and oxygen diffusion out from the substrate into the film, the oxygen is present throughout the entire film.

We notice here that upon hydrogen charging, due to the presence of several elements, and due to the formation of mixed metal and oxide-metal layer, it is difficult to obtain the precise estimation of the content of each element in the film. However, the total content of the metal can be easily estimated, especially based on the assumption of a formation of only di-oxide metal (MO_2).

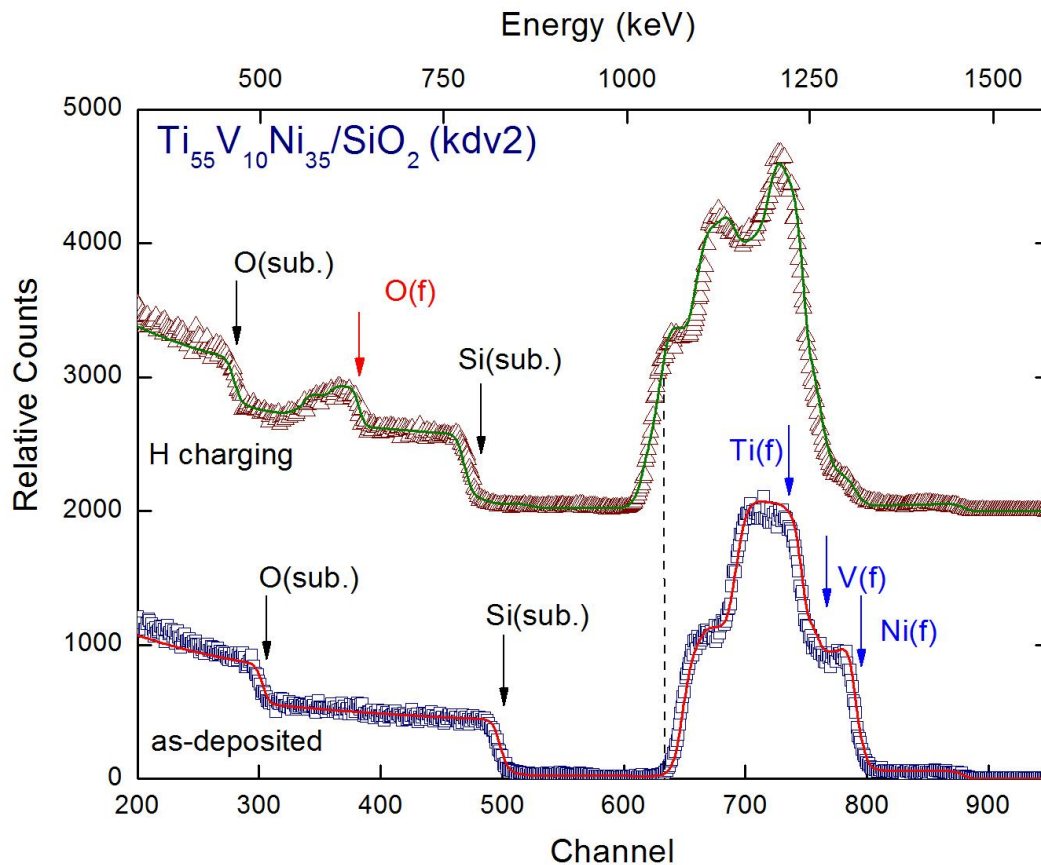


Figure 6.2. Random RBS (markers) and SIMNRA (lines) simulated spectra for 178 nm $\text{Ti}_{55}\text{V}_{10}\text{Ni}_{35}/\text{SiO}_2$ film (kdv2) before and after hydrogen charging. RBS experiments were performed with the incident He^+ ion energy of 1.7 MeV and the backscattering angle of 171° . The film are denoted by its nominal chemical composition and the estimated total thickness in the as-deposited state. The curves were normalized and shifted for a clarity. Ni(f), V(f) and Ti(f) denoted respectively the Ni-, V- and Ti signal in the film. The Si- and O-signal from the SiO_2 substrate is labeled as Si(sub.) and O(sub.). The presence of the oxygen in the entire film as a result of surface oxidation as well as oxygen diffusion out from the substrate is indicated by O(f). The vertical dotted line indicates that the film thickness (or the peak-width) increases upon hydrogenation.

Ti-V-Ni/Si (kdv5)	layer		d (nm)	film thickness (nm)	increased thickness
as-deposited	1	Ti ₃₆ V ₃₄ Ni ₃₀ /Si	151	151	
Hydrogen charging	1	88% TiO ₂ +9% VO ₂ +4% NiO ₂	29	151	0%
	2	14% (Ti,V,Ni)O ₂ +86%(TiVNi)	19		
	3	Ti ₂₁ V ₁₅ Ni ₆₄	26		
	4	Ti ₁₉ V ₄₄ Ni ₃₅	48		
	5	Ti ₁₀ V ₅₀ Ni ₃₅	29		

Ti-V- Ni/SiO ₂ (kdv2)	layer		d (nm)	film thickness (nm)	increased thickness
as-deposited	1	Ti ₅₅ V ₁₀ Ni ₃₅ /SiO ₂	178	178	
Hydrogen charging	1	88% TiO ₂ +12% NiO ₂	17	210	17%
	2	38% TiO ₂ +45% VO ₂ +17% NiO ₂	30		
	3	25% (TiVNi)+75%(Ti,V,Ni)O ₂	58		
	4	70% (TiVNi)+30%(Ti,V,Ni)O ₂	23		
	5	85% (TiVNi)+15% SiO ₂	54		
	6	78% (TiVNi)+22% SiO ₂	28		

Table 6.1. Effect of hydrogen charging on the V-Ti-Ni films deposited on Si and silica SiO₂ substrates (denoted respectively kdv5 and kdv2). The layer-thickness (d (nm)), the element composition of each layer, the percentage (%) of each type of oxides (TiO₂, V₂O₅, VO₂) presented in the film were estimated using SIMNRA and the mass density of the bulk. Layer (1) denotes the surface layer. As a consequence of Si diffusion from the SiO₂ substrate into the film, in the film-substrate interface the mixed (Ti, V, Ni)+SiO₂ layer did appear. The increased thickness of the film (%) due to hydrogenation was estimated for the total film thickness (D (nm)) with respect to that of as-deposited film.

Similar to the sample kdv5, we assume that the significant change of the element-ratio and interdiffusion upon hydrogen charging for sample kdv2 is related to the diffusion process of metals at elevated temperatures during the hydrogen charging process.

The total thickness of the Ti-V-Ni/SiO₂ film increases by 17% by hydrogen charging (i.e. from 178 nm to 210 nm). It is illustrated by the vertical dotted-line in the figure: the Ti-V-Ni peak after hydrogenation ends at a lower energy value, i.e. the peak-width is much larger in this case.

The Ni content is similar in both 2 films. The V content in the second film is much smaller while the Ti content is much larger in the second film (kdv2). Thus we suggest that the increase of the film thickness upon hydrogen charging rather related to the titanium in the film.

6.2. Hydrogen profile in Ti-V-Ni films

Hydrogen profile determined from N-15 experiments for Ti-V-Ni layer deposited on Si (111) is presented in Fig. 6.3. Before hydrogen charging, Ti-V-Ni layer reveals small amount of hydrogen (~4 at.%) distributed quite homogeneously within the whole film up to 100 nm deep from the film surface. On the surface (up to the thickness of 10-15 nm) a quite high concentration of 15 at.% of hydrogen is found. Hydrogen charging causes an enormous increase of hydrogen amount up to 35 at.% in the sample. However, the hydrogen profile reveals that the hydrogen gather mostly in the deepness of the range of 50-100 nm, i.e. in the layer consisted of pure Ti-V-Ni metal (layer 3-5, Table 6.1). Only a small amount of hydrogen (less than 2 at.%) was found at the distance >150 nm from the film surface, i.e. in the substrate. layer consisted of pure Ti-V-Ni metal (layer 3-5, Table 6.1). Only a small amount of hydrogen (less than 2 at.%) was found at the distance >150 nm from the film surface, i.e. in the substrate.

The hydrogen profile has also been obtained by N-15 technique for the Ti-V-Ni film deposited on SiO₂, shown in Fig. 6.4. Similarly, before hydrogen charging an amount of hydrogen up to ~4 at.% is homogeneously distributed in the film. Besides, a higher hydrogen concentration of 15 at.% was also found in the film surface. After hydrogen charging process, a significant increase of hydrogen concentration is revealed. Hydrogen is accumulated deeply in the film, at the deepness (from the film surface) of 100-200 nm, corresponded to the region consisted of layers with a high Ti-V-Ni content (>70%, layer 4-6, Table 6.1). The hydrogen amount reaches 28 at.%, i.e. lower than that in the film deposited on Si(111) substrate.

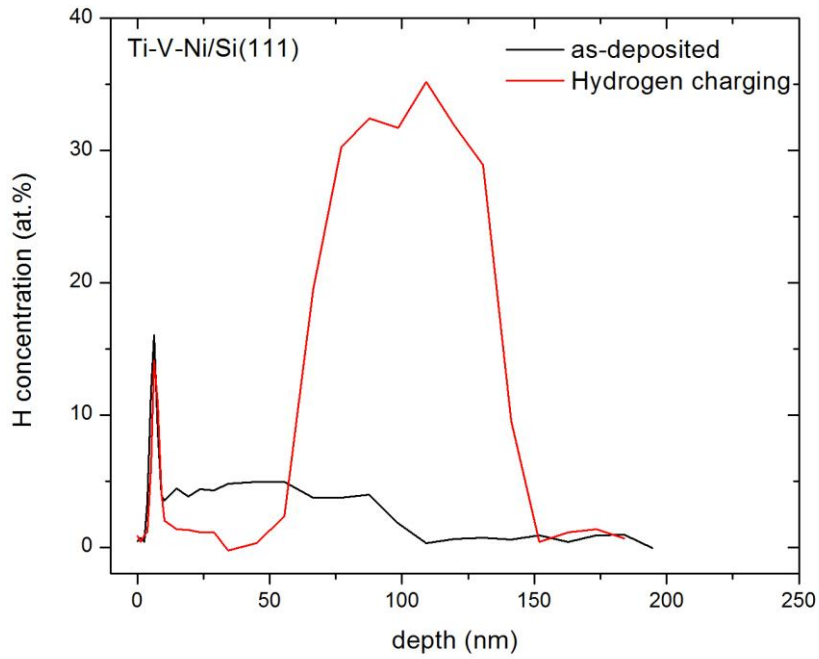


Figure 6.5. Hydrogen profiles of Ti-V-Ni layer on Si(111) before (as-deposited) and after hydrogen charging.

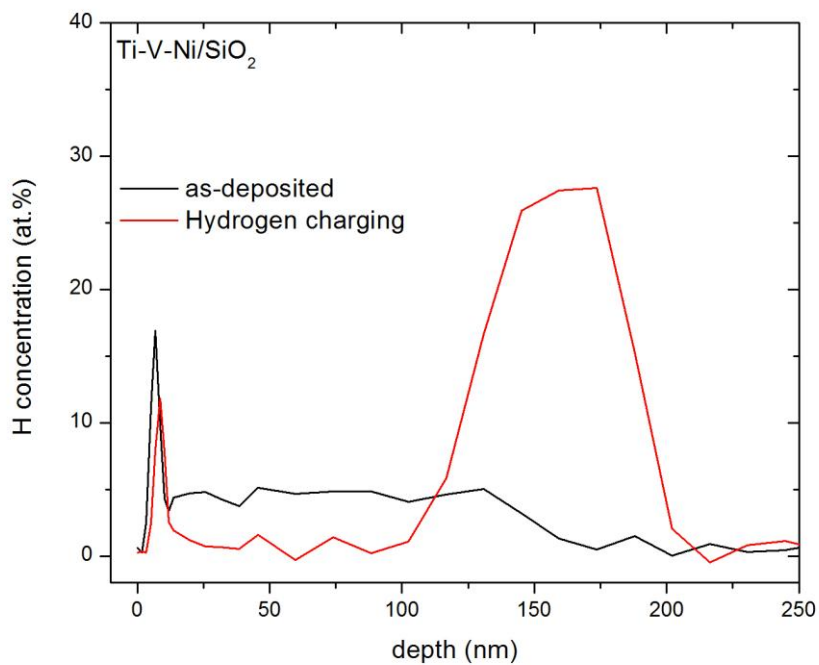


Figure 6.6. Hydrogen profiles of Ti-V-Ni layer deposited on SiO₂ before (as deposited) and after hydrogen charging.

In summary, our results for the Ti-V-Ni films indicate that:

- The film surface was oxidized upon hydrogen charging. It consists mostly TiO_2 .
- Hydrogen diffuses through the oxide layer consisted mostly TiO_2 without gathering there. Instead, hydrogen accumulates in the deeper part of the film where it consists the pure metal layers (for Ti-V-Ni/Si(111) film) or in the mixed metal and metal oxides layers but with a high content of metals (>70%) in the Ti-V-Ni film deposited on SiO_2 .
- N-15 measurements proved that Ti-V-Ni layer deposited on Si(111) has a higher hydrogen storage (35 at.%) than the Ti-V-Ni layer deposited on SiO_2 (28 at.%). On the other hand, the hydrogen storage in the pure metal layer does not lead to any enlargement of the film, while a large increase of the film thickness up to 17% was found for the mixed metal and oxide - metal layer. It indicates that the pure Ti-V-Ni metal layers can have more interstitial sites for hydrogen and that hydrogen storage does not need any lattice expansion.
- The obtained results on Ti-V-Ni films confirmed our earlier observation on Ti- TiO_2 . Namely, a large hydrogen storage in the Ti films and no hydrogen accumulation in TiO_2 layers.
- The Ni content in the two film is similar (30-35 at.%). However, the Ti content is higher in the film deposited on SiO_2 . In other words, the V content is lower. The higher hydrogen storage is found in the film with a higher Ti content (i.e. with a lower V content). Thus it seems that the hydrogen storage is mostly related to titanium indicating that titanium seems to have a higher hydrogen absorption capacity. More experiments are needed to verify the titanium and vanadium hydrogen absorption ability.

Conclusions and final remarks

The aim and scope of this work was to produce and investigate the physical properties of Ti-V-Ni thin films systems and their oxides. The next step assumed the hydrogen charging of such systems and observe the influence of hydrogen charging on their properties.

The surface, chemical composition, structure and electrical resistivity of the thin films of Ti-TiO₂ systems deposited by magnetron sputtering have been investigated by RBS, XRR, optical spectrophotometry and SEM. The results revealed smooth surface of top titanium layer and columnar growth of TiO₂. No significant interdiffusion between the layers have been observed.

Hydrogen charging caused granulation of titanium layer and decrease of electrical resistivity. Covering the samples with palladium layer allowed to improve the hydrogen absorption. For samples without Pd layer, the hydrogen concentration in top titanium layer was up to 40 at.%, whereas palladium, which acts as a catalyst, allowed to obtain concentration of ~50 at.% of hydrogen in both titanium layers. It was observed, that hydrogen can diffuse through the TiO₂ layer without any accumulation there. Such a phenomenon is probably related to the columnar-structure of TiO₂. Columnar growth of TiO₂ was observed by HRSEM.

The preferential orientation in the Ti films (with the *c*-axis of the hexagonal cell of Ti crystallites perpendicular to the substrate) was removed upon hydrogenation at high pressures (p_{H_2} =100 bar). Hydrogen charging under such high pressures caused a large swelling effect for the thicker Ti layer. The large hydrogen storage increased the film thickness.

Hydrogen charging of TiO₂-VO_x systems led to reduction of oxygen state in vanadium oxide layer after each hydrogen charging process. Hydrogen gathers better in V₂O₅ due to its crystal structure. This was confirmed by N-15 measurements. In case of Ti-V-Ni layer, hydrogen charging caused oxidation of the surface and thus accumulation of hydrogen in deeper parts of a film. The obtained results confirmed our earlier observation on Ti-TiO₂. Namely, a large hydrogen storage in the Ti films and no hydrogen accumulation in TiO₂ layers.

References

- [1] see e.g. *Hydrogen in Metals III: Properties and Applications*, in *Topics in Applied Physics*, vol. 73, edited by H. Wipf, Springer-Verlag, Berlin, 1997.
- [2] Y. Fukai, *The Metal-Hydrogen System*, Springer-Verlag, Berlin, 1993.
- [3] A. Zuttel, *Hydrogen storage materials*, University of Birmingham, 2004.
- [4] M. Wanner, *Untersuchung des Langzeitverhaltens der thermodynamischen Stabilität von Metallhydriden*, Ph.D. Thesis, Stuttgart, 2001.
- [5] E. Fromm, *Kinetics of Metal-Gas Interactions at Low Temperatures*, Springer Series in Surface Sciences, Vol.36, Springer-Verlag, Berlin - Heidelberg, 1998.
- [6] H.-P. Klein, *Betriebsverhalten einer zweistufigen Metallhydrid-Sorptionsanlage zur Kälteerzeugung*, Ph.D. Thesis, Stuttgart, 2007.
- [7] T. Schober, H. Wentzl, *Ionics* 1 (1995) 311.
- [8] S. P. Karna, R. D. Pugh, W. M. Shedd, B. B. K. Singaraju, *J. Non-Cryst. Solids* 254 (1999) 66.
- [9] T. K. Mandal, L. Sebastian, J. Gopalakrishnan, L. Abrams, J. B. Goodenough, *Mater. Res. Bull.* 39 (2004) 2257.
- [10] S. Aggarwal, S.R. Perusse, C.W. Tipton, R. Ramesh, H.D. Drew, T. Venkatesan, D.B. Romero, V.B. Podobedov, A. Weber, *Appl. Phys. Lett.* 73 (1998) 1973.
- [11] B. Malaman, J. F. J. Brice, *Solid State Chem.* 53 (1984) 44.
- [12] W. R. Grove, *Phil. Mag.* 14 (1839) 127.
- [13] M. Ismail, *Modification of light-metal hydride properties for hydrogen-energy applications*, Ph.D. Thesis, Wollongong, 2011.
- [14] K. Yoshimura, Y. Yamada, M. Okada, *Surf. Sci.* 566-568 (2004) 751.
- [15] Z. Dehouche, R. Djaozandry, J. Huot, S. Boily, J. Goyette, T. K. Bose, R. Schulz, *J. Alloys Comp.* 305 (2000) 264.
- [16] A. Lèon, E. J. Knystautas, J. Huot, S. Lo Russo, C. H. Koch, R. Schulz, *J. Alloys Comp.* 356–357 (2003) 530.
- [17] R. Schulz, G. Liang, J. Huot, *Proc. 22nd Risø Int. Symp. on Material Science: Science of Metastable and Nanocrystalline Alloys: Structure, Properties and Modeling*, edited by A. R. Dinesen (Roskilde: Risø National Laboratory (2001) 141.
- [18] M. Pozzo, D. Alfe, *Int. J. Hydrog. Energy* 34 (2009) 1922.
- [19] M. Khrussanova, M. Terzieva, P. Peshev, I. Konstanchuk, E. Ivanov, *Mater. Res. Bull.* 26 (1991) 561.

- [20] K. S. Jung, E. Y. Lee, K. S. Lee, *J. Alloys Comp.* 421 (2005) 179.
- [21] J. J.G. Willems, J. Philips, *J. Res. Suppl.* 39 (1984) 1-94.
- [22] T. Kabutomori, T. Takahashi, H. Takeda, Y. Wakisaka, *JSW Technical Report* 53 (1997) 21.
- [23] J. N. Huiberts, R. Griessen, J.H. Rector, R. J. Wijngaarden, J. P. Dekker, D.G. de Groot, N.J. Koeman, *Nature* 380 (1996) 231.
- [24] T. J. Richardson, J. L. Slack, R. D. Armitage, R. Kostecki, B. Farangis, M.D. Rubin, *Appl. Phys. Lett.* 78 (2001) 3047.
- [25] R. A. H. Niessen and P. H. L. Notten, *Electrochem. Solid-State Lett.* 8 (2005) A534.
- [26] A. Budziak, P. Zachariasz, R. Pelka, H. Figiel, J. Zukrowski, M.W. Woch, *J. Alloys and Comp.* 525 (2012) 175 and references therein.
- [27] Z. Tarnawski, L. Kolwicz-Chodak, H. Figiel, N.-T. H.Kim-Ngan, L. Havela, K. Miliyanchuk, V. Sechovsky, E. Santava, J. Sebek, *J. Alloys Comp.* 442 (2007) 372 and references therein
- [28] G. Lütjering, J. J. C. Williams, *Titanium*, Springer, 2007.
- [29] P. Waldner, G. Eriksson, *Calphad*, 23 (1999) 189.
- [30] N. N. Greenwood, A. Earnshaw, *Chemistry of the Elements*, Oxford: Pergamon Press (1984) 1117.
- [31] O. Carp, C. L. Huisman, A. Reller, *Progress in solid state chemistry* 32 (2004) 33.
- [32] A. Fujishima, K. Honda, *Nature*, 238 (1972) 37.
- [33] A. L. Linsebigler, G. Lu, J. T. Yates Jr, *Chem. Rev.* 95 (1995) 735.
- [34] M. Grätzel, B. O'Regan, *Nature* 353 (1991) 737.
- [35] O. K. Varghese, C. A. Grimes, *Nanosci. Nanotech.* 3 (2003) 277.
- [36] A. Fujishima, K. Kohayakawa, K. Honda *J. Electrochem. Soc.* 122 (1975) 1487.
- [37] A. B. Murphy, P. R. F. Barnes, L. K. Randeniya, I. C. Plumb, I. E. Grey, M. D. Horne, J. A. Glasscock, *Int. Journ. of Hydrogen Energy* 31 (2006) 1999.
- [38] J. Nowotny, T. Bąk, M. K. Nowotny, L. R. Sheppard, *Int. Journ. of Hydrogen Energy* 32 (2007) 2609.
- [39] S.-H. Lim, J. Luo, Z. Zhong Z, W. Ji, J. Lin, *Inorg. Chem.* 44 (2005) 4124.
- [40] P. Pillai, K. S. M. Raja, Misra, *J. Power Sources* 161 (2006) 524.
- [41] M. Ni, M. K. H. Leung, D. Y. C. Leung, K. Sumathy, *Renewable and Sustainable Energy Reviews* 11 (2007) 401.
- [42] K. Hashimoto, H. Irie, A. Fujishima, *Japanese J. Appl. Phys.* 44 (2005) 8269.
- [43] A. Fujishima, X. Zhang, D. A. Tryk, *Surf. Sci. Reports* 63 (2008) 515.

- [44] M. A. Henderson, Surf. Sci. Reports 66 (2001) 185.
- [45] M.-I. Baraton, The Open Nanoscience Journal 5 (2011) 64.
- [46] G. R. Dey, A. D. Belapurkar, K. Kishore, J. Photochem. Photobiol. A, 163 (2004) 503.
- [47] M. R. Hoffmann, S. T. Martin, W. Choi, D. W. Bahnemann, Chem. Rev, 95 (1995) 69.
- [48] D. Chatterjee, A. Mahata, Appl. Catal., B-Environ, 33 (2001) 119.
- [49] P. Jacobson, S.-C. Li, C. Wang, U. Diebold, J. Vac. Sci. Technol. B 26 (2008) 2236.
- [50] W.-G. Kim, S-W. Rhee, Microelectron. Eng. 87 (2) (2010) 98.
- [51] Y. Shin-ichi Ohkoshi, T. Tsunobuchi, K. Matsuda, K. Hashimoto, A. Namai, F. Hakoe, H. Tokoro, Nat. Chem. 2 (2010) 539.
- [52] A. Fujishima, X. Zhang X., C.R. Chimie 9 (2006) 750.
- [53] M. Maaza, Z. Jiang, F. Samuel, B. Farnoux, B. Vidal, J. Appl. Crystallography 25 (1992) 789.
- [54] B. J. Choi, J. Appl. Phys. 98 (2005) 1.
- [55] B. G. Pound, Corrosion 47 (1991) 99.
- [56] S. I. Pyun, J. W. Park, Y. G. Yoon, J. Alloys and Comp 231 (1995) 315.
- [57] H. Numakura, M. Coiwa, Acta Metall. 32 (1984) 1799.
- [58] G. C. Woo, C. E. Weatherly, C. E. Coleman, R. W. Gillbert, Acta Metall. 33 (1985) 1897.
- [59] E. Tal-Gutelmacher, D. Eliezer, Materials Transactions 45 (2004) 1594.
- [60] J. J. Xu, H. Y. Cheung, S. Q. Shi, J. Alloys and Comp 436 (2007) 82.
- [61] H.G. Nelson, in: *Hydrogen Effects in Metals*, edited by: A.W. Thompson and N.R. Moody, TMS, Warrendale, PA, (1996) 699.
- [62] H. Wipf, B. Kappesser, R. Werner: J. Alloys and Comp. Vol. 310 (2000) 190.
- [63] A. F. Wells, *Structural Inorganic Chemistry* (5th ed.), Oxford: Clarendon Press, 1984.
- [64] Z. Qin, Y.Zeng, P. R. Norton, D.W. Shoesmith, "Modeling hydrogen permeation through a thin TiO₂ film deposited on Pd using COMSOL multiphysics," in *Proceedings of the 5th COMSOL Conference*, Boston, Mass, USA, 2009.
- [65] G. S. Nadkarni, V. S. Shirodkar, Thin Solid Films 105 (1983) 115.
- [66] H. A. Wriedt, *The O-V (Oxygen-Vanadium) system*, in: *Bulletin of Alloy Phase Diagrams* Vol. 8 No. 2, 1987.
- [67] H. G. Bachmann, F. R. Ahmed, W. H. Barnes, Z Kristallogr., 115 (1961) 110.
- [68] R. Darling, S. Iwanaga, Sadhana- Academy Proceedings in Engineering Sciences 34 (2009) 531.

- [69] A. Talledo, C. G. Granqvist, J. Appl. Phys. 77 (1995) 4655.
- [70] K. Hermann, A. Chakrabarti, R. Druzinic, M. Witko, Phys. Stat. Sol. A173 (1999) 195.
- [71] S. Iwanaga, M. Marciniak, R. B. Darling, F. S. Ohuchi, J. Appl. Phys. 101 (2007) 123709.
- [72] G. W. Coulston, E. A. Thompson, N. Herron, Journal of Catalysis 163 (1996) 122.
- [73] V. Eyert, In Annalen der Physik 11 (2002) 650.
- [74] A. Zylbersztejn, N. F. Mott, Phys. Rev. B 11 (1976) 4383.
- [75] J. B. Goodenough, J. Solid State Chem. 3 (1971) 490.
- [76] A. Cavalleri, T. Dekorsy, H. H. W. Chong, J. C. Kieffer, R. W. Schoenlein, Phys. Rev. B 70 (2004) 161102.
- [77] H. Kuwamoto, J. M. Honig, J. Appel, Phys. Rev. B 22 (1980) 2626.
- [78] M. N. Field, I.P. Parkin. J. Mater. Chem. 10 (2000) 1863.
- [79] V. N. Andreev, V. M. Kapralova, V. A. Klimov, Physics of the Solid State 49 (2007) 2318.
- [80] B. Vaidhyanathan, K. Balaji, K. J. Rao, Chem. Mater. 10 (1998) 3400.
- [81] X. Liu, C. Täschner, A. Leonhardt, M. H. Rummeli, T. Pichler, T. Gemming, B. Büchner, M. Knupfer, Phys. Rev. B 72 (2005) 115407.
- [82] D. Johansson, *VO₂ films as active infrared shutters*, Master Thesis, Linköping, 2006.
- [83] K. Bohmhammel, G. Wolf, G. Gross, H. Madge, J. Low Temp. Phys. 43 (1981) 521.
- [84] E. Tal-Gutelmacher, R. Gemma, A. Pundt, R. Kirchheim, Defect and Diffusion Forum 283-286 (2009) 662.
- [85] K. Kandasamy, N. A. Surplice, J. Phys. D 17 (1984) 387.
- [86] Ch. Walczyk et al., J. Vac. Sci. Technol. B 29 (2011) 1.
- [87] J. M. Herrmann, Top. Catal. 34 (2005) 49.
- [88] H. Kawasaki, T. Ohshima, Y. Yagy, Y. Sud, S. I. Khartsev, A. M. Grishin, J. Phys.: Conference Series 100 (2008) 012038.
- [89] Y.-H. Han et al., J. Korean Phys. Soc. 45 (2004) 1655.
- [90] H. Cele, *Synthesis of VO₂ Nanostructures for Infrared Modulation Applications*, Ph.D. Thesis, Zululand, 2007.
- [91] R. Angelucci, A. Poggi, L. Dori, G.C. Cardinali, A. Parisini, G. Pizzochero, F. Trinro, F. Cavani, C. Critelli, L. Boarino, Thin Solid Films 297 (1997) 43.
- [92] A. Lavacchi, B. Cortigiani, G. Roviola, U. Bardi, A. Atrei, R. Angelucci, L. Dori, S. Nicoletti, A. Poggi, Sensor Actuator B 71 (2000) 123.
- [93] S. Chen, H. Ma, J. Dai, X. Yi, Appl. Phys. Lett. 90 (2007) 101117 .

- [94] V. Msomi, O. Nemraoui, S. Afr J. Sci, 106 (11/12) (2010) 1.
- [95] M. Gasior, B. Grzybowska, *Vanadia catalysts for processes of oxidation of aromatic hydrocarbons* (B.Grzybowska-Swierkosz, J.Haber eds.), Warszawa (1984) 133.
- [96] D. Honicke, J. Xu, J. Phys. Chem. 92 (1988) 4699.
- [97] F. Roozeboom, C. Mittelmejer-Hazeleger, A. Moulijn, J. Medema, V. H. J. de Beer, P. J. Gellings, J. Phys. Chem. 84 (1980) 2783.
- [98] A. Vejux, P. Courtine, J. Solid State Chem. 23 (1978) 93.
- [99] R. Kozlowski, R. F. Pettifer, J. M. Thomas, J. Phys. Chem. 87 (1963) 5176.
- [100] J. Haber, A. Kozłowska, R. Kozłowski, J. Catal. 102 (1986) 52.
- [101] B. Grzybowska-Swierkosz, Appl. Catal. A: General 157 (1997) 263.
- [102] G. Centi, Appl. Catal. A: General 147 (1996) 267.
- [103] L. Silva, *Structural changes and dynamic behaviour of vanadium oxide-based catalysts for gas-phase selective oxidations*, Ph.D. Thesis, Bologna, 2009.
- [104] N. R. Mlyuka, G. A. Niklasson, C. G. Granqvist, Phys. Status Solidi A206 (2009) 2155.
- [105] M. Radecka, M. Rekas, E. Kusior, K. Zakrzewska, A. Heel, K. A. Michalow, T. Graule, Journal of Nanoscience and Nanotechnology 10 (2010) 1032.
- [106] K. Zakrzewska, Vacuum 74 (2004) 335.
- [107] K. Zakrzewska, *Titanium Dioxide Thin Films for Gas Sensors and Photonic Applications*, Habilitation Thesis, AGH, Kraków, 2003.
- [108] B. Łysoń-Sypień, *Nano-oxide materials for gas sensing*, Ph.D. Thesis, Krakow, 2013.
- [109] J. F. R. De Castro, S. F. Santos, A. L. M. Costa, A. R. Yavari, W. J. Botta, T. T. Ishikawa, J. Alloys Comp 376 (2004) 251.
- [110] N. Hanada, T. Ichikawa, H. Fujii, J. Phys. Chem. B 109 (2005) 7188 .
- [111] L. Z. Ouyang, H. Wang, C. Y. Chung, J. H. Ahn, M. Zhu, J. Alloys Comp. 422 (2006) 58.
- [112] X. Yao, C. Wu, A. Du, G. Q. Lu, H. Cheng, S. C. Smith, J. Zou, Y. He, J. Phys. Chem. B 110 (2006) 11697.
- [113] X. B. Yu, J. Z. Chen, Z. Wu, B. J. Xia, N. X. Xu, Int. J. Hydrogen Energy 29 (2004) 1377.
- [114] R. Schmidt, M. Schlereth, H. Wipf, W. Assmus, M. Müller, J. Phys.: Condens. Matter 1 (1989) 2473.
- [115] H. Wipf, Phys. Scripta T94 (2001) 43.

- [116] D. Cauceglia, M. D. Hampton, J. K. Lomness, D. K. Slattery, M. Resan, J. Alloys Comp 417 (2006) 159.
- [117] A. Brudnik, M. Bucko, M. Radecka, A. Trenczek-Zajac, K. Zakrzewska, Vacuum 32 (2008) 936.
- [118] A. Brudnik, H. Czternastek, K. Zakrzewska, M. Jachimowski, Thin Solid Films 199/1 (1991) 45.
- [119] W. M. Posadowski, A. Wiatrowski, J. Dora, Z. J. Radzimski, Thin Solid Films 516 (2008) 4478.
- [120] A. Trenczek-Zajac, M. Radecka, K. Zakrzewska, A. Brudnik, E. Kusior, S. Bourgeois, M.C. Marco de Lucas, L. Imhoff, Journal of Power Sources 194 (2009) 93.
- [121] A. M. Adamska, *Variations of actinide magnetism in uranium-based hydrides and other selected systems*, Doctoral Thesis, Prague-Krakow, 2011.
- [122] web site, <http://www.purdue.edu/>, downloaded on 15th April 2013.
- [123] web site, <http://www.sckcen.be/>, downloaded on 15th April 2013.
- [124] B. D. Cullity, *Elements of X-ray diffraction*, 2nd Edition, Addison-Wesley publishing company, 1978.
- [125] *Introduction to Powder X-Ray Diffraction*, Bruker AXS, 2001.
- [126] M. Yasaka, Rigaku Journal 26 (2010) 1.
- [127] A. K. Wróblewski, *Historia Fizyki*, PWN, Warszawa 2007.
- [128] W.-K. Chu, J. W. Mayer, M. A. Nicolet, *Backscattering Spectrometry*, Academic Press, New York, 1978.
- [129] www.nasa.gov – article on Apollo Expeditions to the Moon, <http://history.nasa.gov/SP-350/toc.html>
- [130] A. Oleś, *Metody doświadczalne fizyki ciała stałego*, Wydawnictwa Naukowo-Techniczne, Warszawam 1998.
- [131] R.G. Newton, *Scattering theory of waves and particles*, McGraw Hill, 1966.
- [132] M. Mayer, SIMNRA home page <http://home.rzg.mpg.de/~mam/>
- [133] The RUMP home page <http://www.genplot.com/doc/RUMP/intro.htm>
- [134] Introduction to SIMS techniques <http://www.cameca.com/instruments-for-research/sims.aspx>
- [135] NRA techniques, http://physik2.unigoettingen.de/research/2_hofs/methods/nra
- [136] J. F. Zielgler, J. P. Biersack, SRIM home page : <http://www.srim.org/>
- [137] M.- L. Kääriäinen, T. O. Kääriäinen, D. C. Cameron, Thin Solid Films 517 (2009) 6666.
- [138] Ti 44-1294 JCPDS –International Center for Diffraction Data, 1999.

- [139] B.L. Henke, E.M. Gullikson, J.C. Davis, *Atom. Data Nucl. Data* 54 (2) (1993) 181.
- [140] S. Nakao et.al., *Thin Solid Films* 343-344 (1999) 195.
- [141] K. Bohmhammel, G. Wolf, G. Gross, H. Madge, *J. Low Temp. Phys.* 43 (1981) 521
- [143] A.C. Switendick, *J. Less-Common Met.* 49 (1976) 283.
- [144] L. Yingtao et al, *Journal of the Korean Physical Society*, 58 (2011) 407.
- [145] M. Takeda et al., *Vacuum* 84 (2010) 352.
- [146] K. Mizuno et al., *Phys. Stat. Sol. (a)* 204 (2007) 2734.
- [147] J. B. Bates, J. C. Wang, R. A. Perkins, *Phys. Rev. B*, 19 (1979) 4130.
- [148] K. Drogowska, Z. Tarnawski, A. Brudnik, E. Kusior, M. Sokołowski, K. Zakrzewska K, A. Reszka, N.-T. H. Kim-Ngan, A. G. Balogh, *Mater. Res. Bulletin* 47 (2012) 296.
- [149] K. Drogowska, S. Flege, C. Schmitt, D. Rogalla, H.-W. Becker, Nhu-T. H. Kim-Ngan, A. Brudnik, Z. Tarnawski, K. Zakrzewska, A. G. Balogh, *Adv. Materials Sci. and Eng.* 2012 (2012) art. 269603.

List of publications

1. K. Drogowska, N.-T.H. Kim-Ngan, A.G. Balogh, M. Radecka, A. Brudnik, K. Zakrzewska, Z. Tarnawski, *Diffusion and chemical composition of TiN_xO_y thin films studied by Rutherford Backscattering Spectroscopy*, Surface Science. 604 (2010) 1010.
2. K. Drogowska, S. Flege, C. Schmitt, D. Rogalla, H.-W. Becker, Nhu-T. H. Kim-Ngan, A. Brudnik, Z. Tarnawski, K. Zakrzewska, M. Marszałek, A. G. Balogh, *Hydrogen Charging Effects in Pd/Ti/TiO₂/Ti Thin Films Deposited on Si(111) Studied by Ion Beam Analysis Methods*, Advances in Materials Science and Engineering (2012), 269603.
3. K. Drogowska, Z. Tarnawski, A. Brudnik, E. Kusior, M. Sokołowski, K. Zakrzewska, A. Reszka, N.- T.H. Kim-Ngan, A.G. Balogh, *RBS, XRR and optical reflectivity measurements of Ti-TiO₂ thin films deposited by magnetron sputtering*, Materials Research Bulletin, 47 (2012) 296.
4. K. Drogowska, S. Flege, D. Rogalla, H.-W. Becker, E. Ionescu, N.-T.H. Kim-Ngan, A.G. Balogh, *Hydrogen content analysis in hydrogen-charged PZT ferroelectric ceramics*, Solid State Ionics 235 (2013) 32.
5. Z. Tarnawski, Nhu-T. H. Kim-Ngan, K. Zakrzewska, K. Drogowska, A Brudnik, A. G. Balogh, R. Kuzel, L. Havela, V. Sechovsky, *Hydrogen storage in Ti-TiO₂ multilayers*, Adv. Nat. Sci.: Nanosci. Nanotechnol. 4 (2013) 025004.